POLISH ACADEMY OF SCIENCES
INSTITUTE OF PHYSICAL CHEMISTRY


ul. M. Kasprzaka 44/52, 01-224 Warsaw, Poland

# Selected Properties of Novel Hydrides Synthesized from $R_7Rh_3$ (R=Ho, Y, Dy, Tb and Er) and Several Transition Metal based Intermetallic Compounds

**Department I: Physical Chemistry of Solid State**

**Ryutaro Sato**

**Supervisor: Stanisław M. Filipek**

Warsaw, 2010

# Index

# Symbols

| | |
|---|---|
| $p$ | pressure |
| $T$ | temperature |
| $R$ | gas constant |
| $V$ | volume |
| $C$ | composition |
| $H$ | enthalpy |
| $S$ | entropy |
| $G$ | Gibbs free energy |
| $E$ | activation energy |

| | |
|---|---|
| $N$ | the total number of molecules |
| $k_B$ | Boltzmann constant |
| $m$ | mass of molecule |
| $N_A$ | Avogadro's constant |
| $\Delta H_{ph}$ | enthalpy of physisorption of $H_2$ |
| $\Delta H_c$ | enthalpy of chemisorption |
| $E_c$' | activation energy of transition from physisorption of $H_2$ into chemisorption of H atoms |
| $E_d$ | activation energy from chemisorption state to physisorption state |
| $E_m$ | activation energy of diffusion of H atoms in metals |
| $\Delta_{trans}H$ | enthalpy change of phase transition |
| $\Delta_{trans}S$ | entropy change of phase transition |
| $\Delta_f H^\circ$ | standard enthalpy of metal hydride formation |

| | |
|---|---|
| **L** | total orbital angular momentum |
| **S** | total spin angular momentum |
| $M$ | magnetization |
| **H** | magnetic field |

| | |
|---|---|
| $\chi$ | magnetic susceptibility |
| $C_C$ | Curie constant |
| $\theta$ | Weiss constant |
| $T_C$ | Curie temperature |
| $T_N$ | Neel temperature |
| $T_t$ | Another antiferromagnetic transition temperature in a reentrant magnetic property |
| $q$ | heat |
| $C_h$ | heat capacity (specific heat) |

# 1. Introduction

Many metals and alloys can absorb hydrogen. Since they can form hydrides with high density of hydrogen atoms they can find application in various technologies including nuclear reactors, preparation of pure metal powders and strong magnets. Hydrogen storage alloys were also proposed as energy storage materials after the oil crisis at the Middle East and Iran-Iraq war in 1970's.

From long time it had been known well that a certain metals can absorb hydrogen and form hydrides. The discovery reported at the end of 1960's by Vucht and coworkers in Philips laboratory in Holland revealed that $SmCo_5$ intermetallic compound absorbed huge amount of hydrogen, and the developments of hydrogen storage alloys were started at that moment [1]. In their systematic researches of hydrogen reactions with $RT_5$ alloys (R: Rare earths, T: Transition Metals), they found $LaNi_5$, which is a typical hydrogen storage alloy. At the same time, $Mg_2Ni$ was discovered by Reilly and coworkers in Brookhaven National Laboratory in U.S.A [1]. Moreover, they discovered TiFe alloy for hydrogen storage as one of the cheapest alloy. At the end of 1970's, $TiMn_{1.5}$, $TiCr_2$ alloys and Zr-series alloys with Laves phase structure were also discovered [1].

From early 1970's it became clear that development of high hydrogen pressure technique is a very effective tool for synthesis of many new hydrides.

$ZrCo_2$ and/or $ZrFe_2$ – C15 Laves phase with $Fd\bar{3}m$ space group shows the simplest hydride formation. More complicated case is transformation of $RFe_2$ into $RFe_2H_5$ accompanied with symmetry changes. For instance, cubic C15 structures of $YFe_2$ and $ErFe_2$ transform into orthorhombic structure when the $YFe_2H_5$ and the $ErFe_2H_5$ are formed [2]. Furthermore, the most complicated changes occur during formation of $RMn_2D_6$ (where R = Y, Dy, Er, Gd and Ho) from $RMn_2$ (space group $Fd\bar{3}m$ or $P6_3/mmc$) under high-pressure and high-temperature conditions. The space group of $RMn_2D_6$ is $Fm\ m$ (constituted of four formula units) in spite of different structures of the parent sample [3,4,5]. The 8*c* site is randomly occupied by four R and four Mn atoms. This random occupation suggests that it is possible that 8*c* site in one

cell is occupied only by rare earths (R atoms) and in another one only by Mn atoms. Therefore, one can expect that formation of the $RMn_2H_6$ type hydrides from other R-Mn alloys (not belonging to C14 or C15) would also be possible.

Hydrogen may also modify magnetic properties. For instance, many rare earth based alloys change markedly their magnetic properties during hydride formation. It seems that interaction of hydrogen with valence shell electrons of transition metals in the alloys has influence on their magnetic properties [6,7]. On the other hand the expansion of interatomic distance should also influence magnetic interactions.

In this work, the high hydrogen pressure technique has been used to synthesize novel hydrides from four groups of materials:

1) Pseudo-binary Zr based alloys in search of composition most suitable for hydrogen storage.
2) $GdFe_2$, $TbFe_2$, $DyFe_2$ and $HoFe_2$ aiming at possible formation of $RFe_2H_5$ deuterides of orthorhombic structure like $ErFe_2D_5$ and $YFe_2D_5$.
3) $Y_6Mn_{23}$ and $YMn_{12}$ to prove hypothesis that they can form $YMn_2H_6$-type hydrides.
4) $R_7Rh_3$ (R=Ho, Y, Dy, Tb and Er) with focus on the influence of hydrogen on their magnetic properties.

# 2. Theory

## *2.1. The Interaction of Hydrogen with Metals and Alloys*

The process of hydrogen reaction with metals and alloys including formation of hydrides can be classified as following elementary processes [8,9].

I. The transport of $H_2$ molecules from gas phase to the metal surface.
II. The physisorption of $H_2$ molecules on the metal surface.
III. The $H_2$ dissociation into H atoms and the subsequent chemisorption of hydrogen atoms on the surface.
IV. The diffusion of H atoms into the metal.
V. The formation of the hydrogen solid solution.
VI. The formation of the metal hydride.

In these elementary processes of hydrogen interaction, I ~ III are called "Surface processes" (Fig. 2.1). To describe the processes precisely and strictly, it is required to consider influences of residual gas molecules on the metal surface in vacuum [10,11]. In order to analyze surface conditions of a sample, equipments as AES (Auger Electron Spectroscopy) or XPS (X-ray Photoelectron Spectroscopy) would be useful. This is especially important when syntheses occur at pressures lower than 0.1 MPa ($H_2$). However, since the very high-pressure synthesis of hydrides is the main subject of this study, only the behavior of $H_2$ molecules and H atoms will be discussed in next chapter.

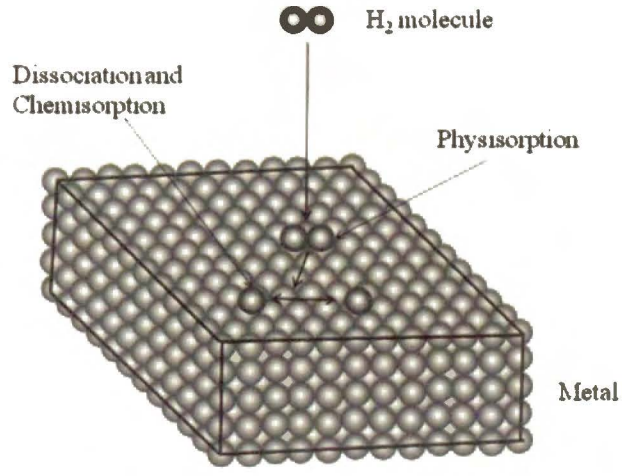


**Fig. 2.1. Hydrogen interaction on a metal surface**

### 2.1.1. *The Physisorption of $H_2$ Molecules on Metal Surface*

$H_2$ molecules with a certain striking rate come closer to the metal surface and interact with the surface by physisorption. Physisorption is one of attractions, which occurs by non-uniform distribution of electrons (van der Waals force), and its binding energy is very small (Fig. 2.2.). Fig.2.3. shows a schematic potential energy diagram of surface reaction between hydrogen and metals. In this figure, activation energies and reaction enthalpies of each elementary process are estimated per 1 mol of $H_2$ molecules. The enthalpy of physisorption of $H_2$ molecules is $\Delta H_{ph}$, and it is obvious that the binding energy is small and can be absorbed as vibrations of a lattice and dissipated as thermal motion [12].

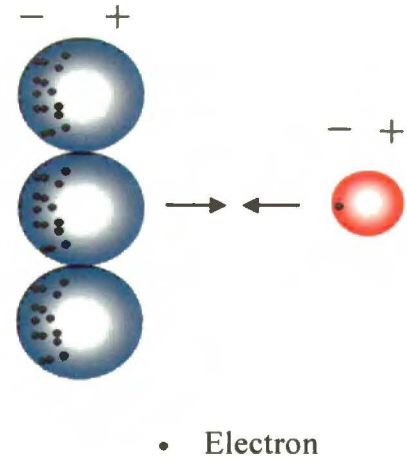


**Fig. 2.2. Scheme of a physisorption mechanism for gas molecules**

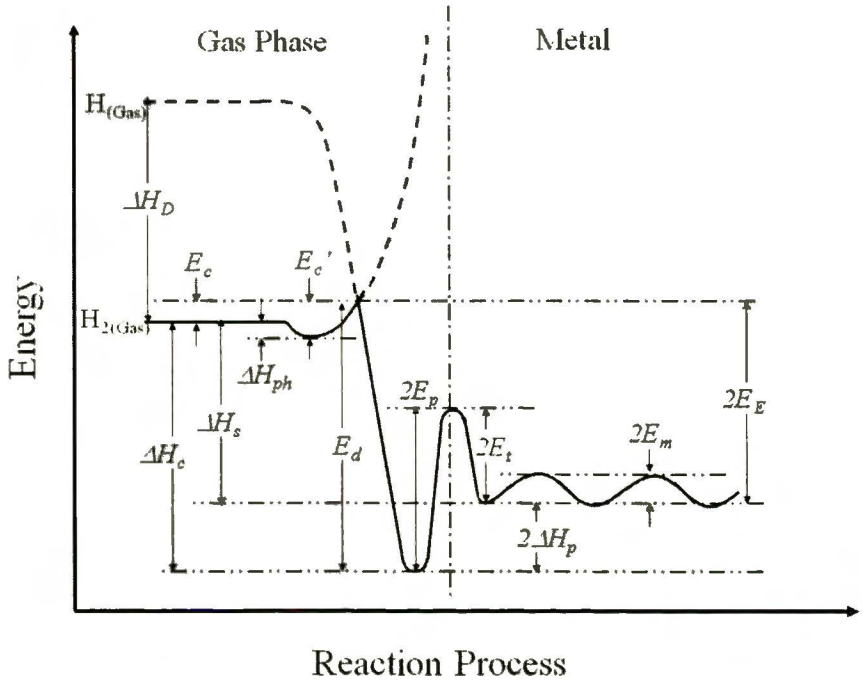


**Fig. 2.3. One dimensional schematic potential energy diagram illustrating the interactions of $H_2$ with a metal surface**

## 2.1.2. *The Dissociation of $H_2$ Molecules into H Atoms and Chemisorption of H Atoms on the Surface*

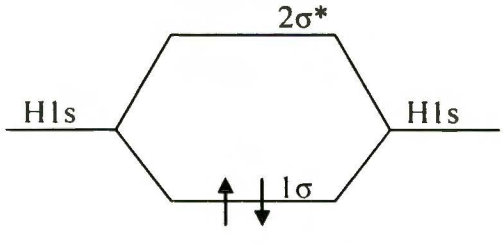


**Fig. 2.4. A $H_2$ molecular orbital energy level diagram for orbitals constructed from the overlap of H1s orbitals.**

The $H_2$ molecules physisorbed on metal surface get over activation energy $E_c$' (in Fig.2.3), and are dissociated and chemisorbed on the surface with the binding energy $1/2(\Delta H_c + \Delta H_D)$ [13]. According to Nørskov and Besenbacher who have studied theory of interactions between hydrogen and metals from the point of view of electronic states, $H_2$ molecules can dissociate into H atoms around the top of the potential barrier $E_c$' by electrons

occupying an antibonding state $2\sigma^*$ [14] (Fig.2.4). When the molecule is far from the surface it has an occupied bonding state $1\sigma$ and unoccupied antibonding state $2\sigma^*$. Unlike monoatomic molecules like helium, $H_2$ molecules can chemisorb on the metal surface. At that moment, the antibonding $2\sigma^*$ orbital starts becoming occupied and subsequently the molecule is dissociated.

### 2.1.3. *The Diffusion of H Atoms into the Metals*

In general, chemisorbed gas atoms on a metal surface diffuse into the metal immediately if there is no thick surface coverage on the metal. H atoms in particular can diffuse into metals with higher diffusion rate than the other elements as shown in Fig. 2.5 [15]. In Fig. 2.3, the activation energy for diffusion of H atoms is shown as "$2E_m$" (because the activation energy is per 1 mol of "$H_2$ molecules", and if the molecules are dissociated it becomes 2 mol of "H atoms") and it is smaller than the others. In general, the height of the barrier and the diffusion mechanism varies drastically with temperature.

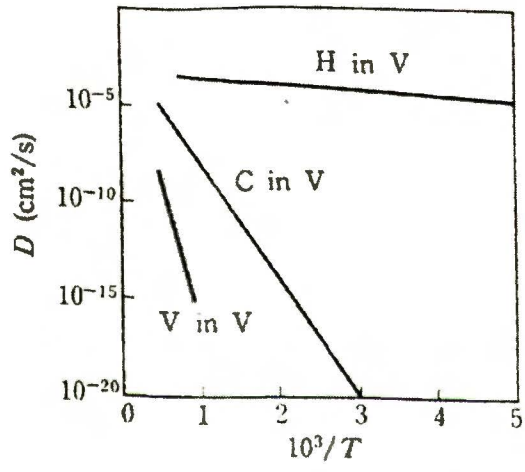


**Fig. 2.5. Diffusion coefficients of H and C in V, and self-diffusion of V [15]**

Diffusion of gas atoms into metals occur through the crystal lattice not along grain boundaries, what was reported by S. Dushman [11] and C.A. Edward [16]. Nowadays, muon or muonium (Mu, $\mu^+$, $e^-$) are regarded as H atoms probe diffusing in the metal and their movement can be observed accurately by using Muon spin rotation/ relaxation/ resonance ($\mu$SR) [15,17]. H atoms can get over the activation energies by their thermal motion and an excitation, but the mechanism changes from the thermal motion of the atoms to their tunneling at sufficiently low temperature. For instance, it has been reported that the hopping rate of muon increases markedly below 20 K [18].

### 2.1.4. *Formation of the Hydrogen Solid Solution*

In general, H atoms diffusing and dissolving in a metal form hydrogen solid solution. The solid solution exists in a region called "α-phase" on *p-C* isotherms (Fig.2.6). Precipitation of the hydride phase (β-phase) starts at beginning of plateau which corresponds to coexistence of α- and β-phases. Finally, steep part of isotherm beyond plateau corresponds to pure β-phase.

Dissolved hydrogen atoms can move freely in the α-phase. Especially at low hydrogen concentration, interaction among the dissolved atoms is not strong and the relation between concentration and pressure follows the Sieverts' law.

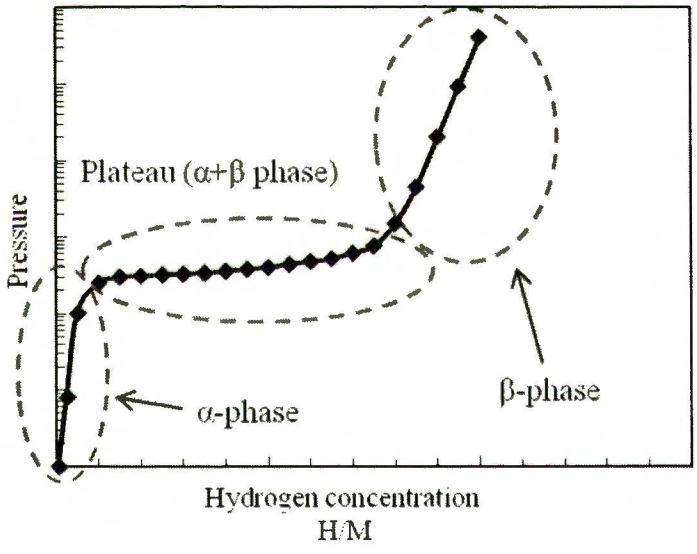


**Fig. 2.6. Typical *p-C* isotherm for hydrogen absorption.**

### 2.1.5. *Formation of the Metal Hydride*

The formation of the metal hydride begins at pressure corresponding to plateau region where α- and β-phases coexist on *p-C* isotherm (Fig. 2.6). At the initial stage of this process appear areas oversaturated with hydrogen (excess chemical potential of hydrogen in solid solution) from which the hydride is precipitated gradually [19]. When a metal forms hydride, unit cells of the metal are expanded and this expansion can be accompanied with change of the crystal structure. In many cases, the hydrogenation causes also pulverization of metals (Fig. 2.7) [20].

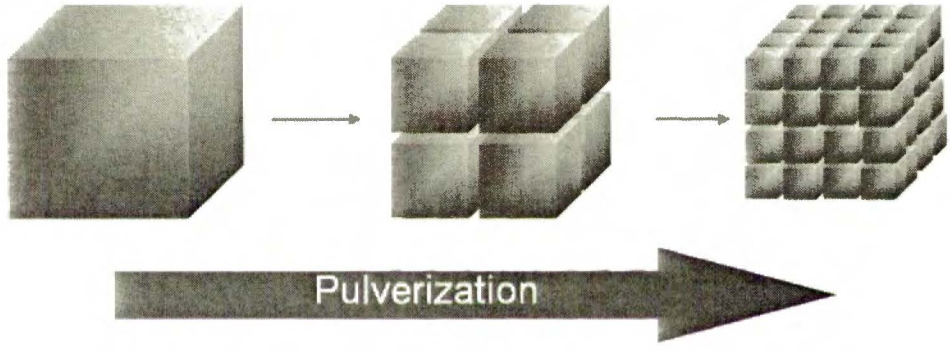


**Fig. 2.7. Pulverization of a sample**

At the right end of plateau the transformation into β-phase is completed and consequently *p-C* isotherm rises steeply as shown in Fig. 2.6. Let us remark that for many alloys two or more plateaux are observed when hydrogen pressure is gradually increased. These plateaux correspond to hydrides with different stoichiometry.

## 2.2. *The Influence of Hydrogenation on Rare Earth – Transition Metal Compounds*

When a transformation from rare earth dihydride $RH_2$ into trihydride $RH_3$ occurs, metallic electrical conduction is lost and magnetic ordering is eliminated or greatly suppressed because conduction electrons are attracted to absorbed hydrogen atoms [21]. Since electrical conduction and exchange interaction which leads to magnetic ordering both require the presence of conduction electrons, it appears that hydrogenation results in a complete depopulation of the host metal conduction band. Thus, hydrogen in these materials is essentially anionic and hence the bonding in rare earth tri-hydrides is essentially ionic.

Intermetallic compounds involving Fe, Co or Mn combined with the rare earths can easily absorb hydrogen to form hydrides. They have proton densities exceeding that of liquid hydrogen. Hydrogenation to this extent usually modifies the electronic density of states and expands interatomic distances of the host metal (Fig. 2.8) [21]. Among the effects observed are; (1) Strengthening the exchange interaction to convert a paramagnetic system into a ferromagnet ($Th_6Mn_{23}$) [22]; (2) Suppression of ferromagnetism ($Y_6Mn_{23}$) [23]. Fig. 2.9 shows the dependence of the magnetization on the hydrogen content for $GdFe_3H_x$ and $Dy_6Fe_{23}H_x$. Thus, magnetic moment tends to be weakened with increasing hydrogen content in these alloys.

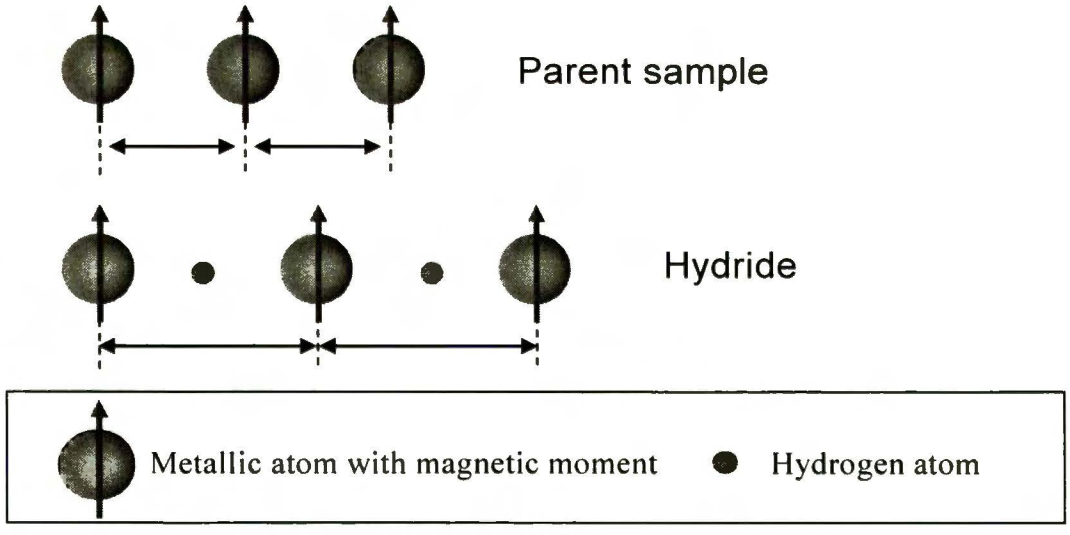


**Fig. 2.8. Spin-spin interactions of metallic atoms with/without hydrogen atoms**

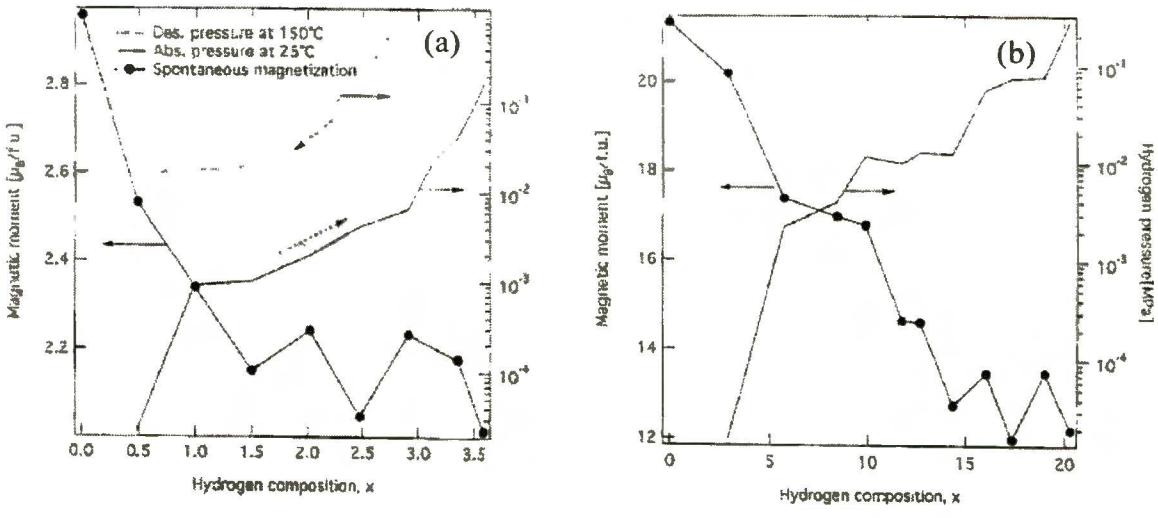


**Fig. 2.9. Dependence of spontaneous magnetizaton on hydrogen content for (a) $GdFe_3H_x$ and (b) $Dy_6Fe_{23}H_x$. Both *p-C* isotherms were measured at 298 K [24].**

In general, the magnetization often varies linearly with hydrogen content in the two phases (α and β) region because the magnetization is weighted average of the magnetic moment between the two phases [24]. For example, the magnetization $M$ of $LaCo_5H_x$ decreases linearly with hydrogen content $x$ in the α–β and β–γ regions but the gradient $dM/dx$ differs between the two phases. The R-T intermetallic compounds and their hydrides often have a large magnetocrystalline anisotropy with anisotropy fields higher than several tesla. In such case, neither the saturation magnetization nor the spontaneous magnetization can be determined exactly from magnetization measured in the low field [24].

# 3. Literature Review

## *3.1. $AB_2$ Laves Phase Compounds*

Laves phases intermetallics are composed of two different metallic atoms A and B with the different atomic radii; usually $r_A:r_B \approx 1.2:1$. The Laves phases have C14, C15 and C36-type structures (Fig. 3.1). Most of hydrogen storage alloys with Laves phase belong to C14 or C15-type structures, and only a few C36-type compounds can absorb hydrogen.

The properties of the $AB_2$ Laves phase including their pseudo-binary alloys are of basic and practical interest. One of the reasons is that more than 300 of them form hydrides with capacities equal or higher than 1 H/Metal ratio. Hydrogen atoms in Laves phase compounds usually occupy interstitial sites and induce an increase in the lattice parameters often accompanied with change of their structure. The interstitials available for hydrogen in the $AB_2$ compounds are tetrahedral sites that are formed by two B and two A atoms or by three B atoms and one A atom or by four B atoms. Table 3.1 gives a list of the various sites and the number of the sites per unit cells for the cubic $MgCu_2$-type and hexagonal $MgZn_2$-type structures [25].

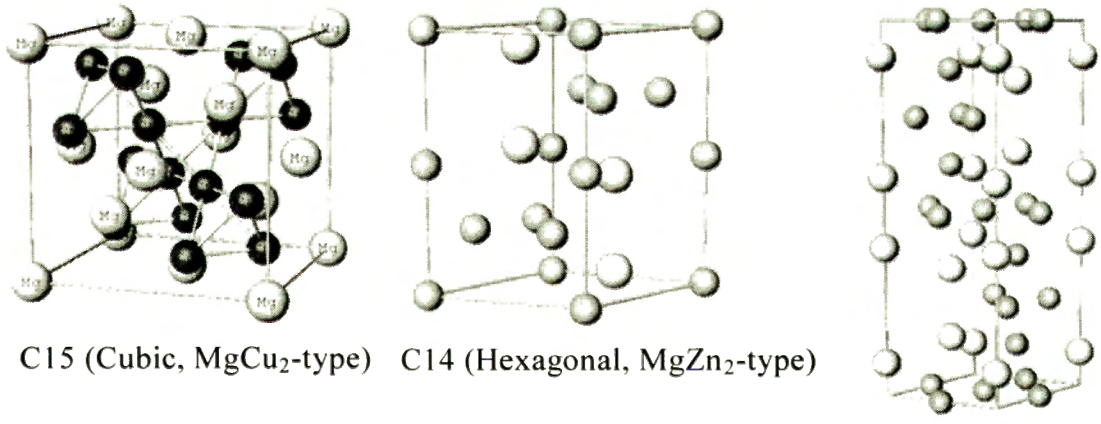

C15 (Cubic, $MgCu_2$-type) C14 (Hexagonal, $MgZn_2$-type) C36 (Hexagonal, $MgNi_2$-type)

**Fig. 3.1. Three types of Laves phases**

**Table 3.1. Tetrahedral interstitial sites in cubic (hexagonal) $MgCu_2$ ($MgZn_2$)-type compounds [25]**

| Interstitial site | Composition | Number of sites per unit cell | Number of sites per formula unit |
|---|---|---|---|
| b (e) | 4B | 8 (4) | 1 |
| e (k, f) | 1A+3B | 32 (12k+4f) | 4 |
| g (l) | 2A+2B | 96 (24l+24l) | 12 |

### 3.1.1. *$ZrCo_2 - H_2$ and $ZrFe_2 - H_2$ Systems*

At normal conditions $ZrCo_2$ and $ZrFe_2$ dissolve only small amount of hydrogen. Even after hydrogenation at 7 MPa [26] both alloys did not transform into hydrides as proved by XRD analysis. However, their hydrides (deuterides) can be formed at 0.7 GPa ($H_2$) and 373 K as confirmed by XRD and Neutron Diffraction (ND) (Fig. 3.2) [27,28]. According to ND analysis, both $ZrFe_2$ and $ZrFe_2D_x$ phases crystallized in the cubic C15 structure with *Fd m* space group. However, the lattice volume of the deuteride was by 22.9 % larger than that of parent $ZrFe_2$. Deuterium atoms in $ZrFe_2D_x$ are located in 96g A2B2 site as shown in Table 3.2. $ZrCo_2$ transformed into $ZrCo_2D_x$ and coexistence of both $ZrCo_2$ and $ZrCo_2D_x$ was observed in the XRD and ND patterns. The ND pattern was refined assuming that $ZrCo_2Dx$ crystallizes in the C15 type structure with D atoms in A2B2 sites. The refinement of the deuteride showed that the increase in cell volume is 11.6% and the total amount of D atom in the 96g A2B2 site was 1.65 D/f.u. (Table 3.2).

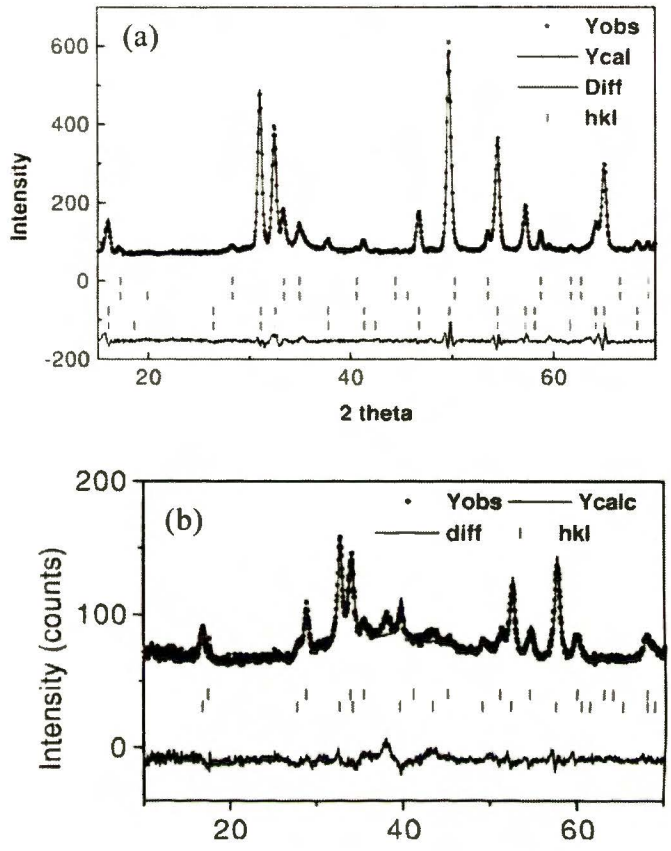


**Fig. 3.2. Neutron diffraction patterns of (a) $ZrFe_2D_x$ refined with a mixture of $ZrFe_2D_{2.7}$+$ZrFe_2$ and (b) $ZrCo_2D_x$ refined with a mixture of $ZrCo_2$ and $ZrCo_2D_2$ [28].**

**Table 3.2. Comparison of structural data of parent compounds ($ZrFe_2$ and $ZrCo_2$) and their deuterides [28].**

| Phase | Space group | $a$ (nm) | $\Delta a/a$ (%) | $V$ (nm$^3$) | $\Delta V/V$ (%) |
|---|---|---|---|---|---|
| $ZrFe_2$ | *Fd m* | 0.706 | - | 0.352 | - |
| $ZrFe_2D_n$ | *Fd m* | 0.756 | 7.1 | 0.433 | 22.9 |
| $ZrCo_2$ | *Fd m* | 0.693 | - | 0.333 | - |
| $ZrCo_2D_n$ | *Fd m* | 0.719 | 3.7 | 0.372 | 11.6 |

### 3.1.2. *$YFe_2 - H_2$ ($D_2$) and $ErFe_2 - H_2$ ($D_2$) System*

Both $YFe_2$ and $ErFe_2$ with cubic C15 Laves phase can absorb hydrogen up to x = 5 per formula unit ($RFe_2H_x$) under high pressure condition [2,29]. Their parent structures transform into several different structures depending on hydrogen content accompanied by multiplateaux character of their *p-C* isotherms. $YFe_2D_x$ shows cubic, tetragonal and rhombohedral structures at $0 \leq x \leq 4.2$ depending sensitively on deuterium content as shown in Table 3.3 [30,31]. After hydrogen treatment of $YFe_2$ at 1 GPa ($H_2$) and 373 K thermal decomposition analysis proved that hydrogen content was 5 H/f.u [2]. The XRD patterns of $YFe_2H_5$ were indexed in a centered orthorhombic cell with $a$ = 0.544 nm, $b$ = 0.585 nm and $c$ = 0.808 nm, and could be described in the space group *Imm*2 as given in Table 3.4 [2].

**Table 3.3. Structural data of $YFe_2D_x$ deuterides [30].**

| Compound | Structures | Cell parameters |
|---|---|---|
| $YFe_2$ | cubic | $a$ = 0.736 nm |
| $YFe_2D_{1.2}$ | tetragonal | $a$ = 1.198 nm, $c$ = 0.761 nm |
| $YFe_2D_{1.75}$ | cubic | $a$ = 1.534 nm |
| $YFe_2D_{1.9}$ | tetragonal | $a$ = 1.215 nm, $c$ = 2.307 nm |
| $YFe_2D_{2.6}$ | cubic | $a$ = 0.778 nm |
| $YFe_2D_{2.9}$ | cubic | $a$ = 0.783 nm |
| $YFe_2D_{3.3}$ | rhombohedral | $a$ = 0.551 nm, $\alpha$ = 61.43° |
| $YFe_2D_{4.2}$ | rhombohedral | $a$ = 0.552 nm, $\alpha$ = 62.75° |

**Table 3.4. Refined parameters and atomic positions in the space group *Imm*2 for $YFe_2H_5$ [2].**

| Space group *Imm*2 | | | |
|---|---|---|---|
| Cell parameters | $a = 0.544$ | $b = 0.585$ | $c = 0.808$ |
| Atom | $x$ | $y$ | $z$ |
| Y1 | 0 | 0 | -0.020 |
| Y2 | 0 | 0.5 | 0.746 |
| Fe1 | 0.239 | 0 | 0.616 |
| Fe2 | 0 | 0.260 | 0.369 |

In the case of the $ErFe_2H_x$, the cubic structure maintains at several phases with different hydrogen concentration {α (x = 0 to 0.15), β (x = 1.25 to 2.0), γ (x = 2.25 to 2.75), δ (x = 3.2 to 3.65)}. At ε phase with x = 4 the hydride shows rhombohedral distortion [32,33]. An orthorhombic structure with the lattice parameters $a = 0.544$ nm, $b = 0.579$ nm and $c = 0.801$ nm appears during deuterization at 1 GPa and 473 K, and the sample forms $ErFe_2D_5$ single phase deuteride under these conditions [2].

The XRD analysis of $ErFe_2D_5$ at lower pressure revealed a coexistence of cubic and orthorhombic phases, what corresponds to a report from Ref. [33]. The weight percentage of the orthorhombic phase increased at the expense of the cubic phase as the hydrogen pressure was raised (Fig. 3.3), reaching nearly 100 % for 1.1 GPa.

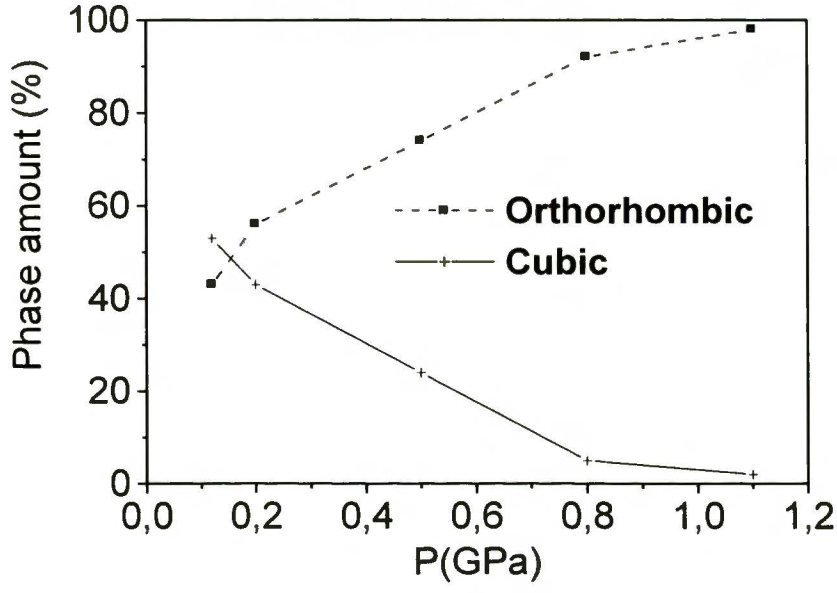


**Fig. 3.3. Evolution of the amount of cubic $ErFe_2D_4$ and orthorhombic $ErFe_2D_5$ versus applied hydrogen pressure [29].**

In the parent $RFe_2$ with the cubic $Fd\bar{3}m$ space group three different interstitial sites are available: R2Fe2, RFe3 and Fe4. Due to both geometrical and thermodynamical factors, the R2Fe2 site is primarily occupied by hydrogen atoms during the hydrogenation [2]. According to refinement of NPD pattern of $ErFe_2D_5$ with orthorhombic structure performed at 273 K (Fig. 3.4), deuterium atoms occupying interstitial sites are attributed to 6 atoms in the Er2Fe2 site and 2 atoms in the ErFe3 site whereas the Fe4 site is empty as shown in Table 3.5 [29].

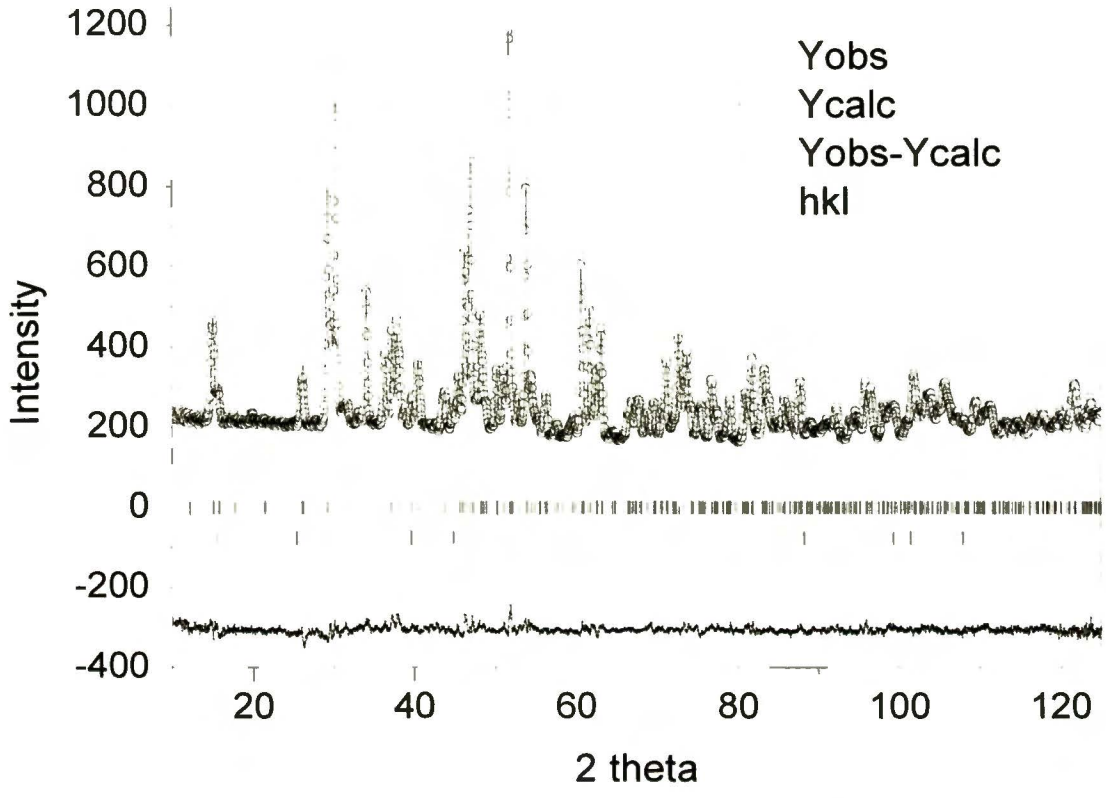


**Fig. 3.4. Refined NPD pattern of a $ErFe_2D_5$ compound measured on the 3T2 spectrometer at 270 K. The upper hkl bars correspond to the orthorhombic phase and the lower ones to the cubic $ErFe_2D_4$ phase [29].**

**Table 3.5. Refined cell parameters, atomic positions, thermal factors and deuteride occupancy numbers from the 3T2 NPD pattern of $ErFe_2D_5$ at 270 K. The D1–D6 sites are Er2Fe2 types interstitial sites and the D7–D8 are ErFe3 ones [29].**

| Atom (Wyckoff) | $x$ ($\delta x$) | y ($\delta y$) | z ($\delta z$) |
|---|---|---|---|
| Er1(2a) | 0 | 0.258(6) | 0 |
| Er2(2a) | 0 | 0.764(6) | 0.771(3) |
| Fe1(4b) | 0.252(3) | 0.255(3) | 0.636(6) |
| Fe2(2a) | 0 | -0.0260(6) | 0.392(6) |
| Fe3(2a) | 0 | 0.488(6) | 0.382(6) |
| D1(4b) | 0.044(6) | 0.233(9) | 0.275(6) |
| D2(4b) | 0.428(3) | 0.285(4) | 0.001(6) |
| D3(2a) | 0 | 0.384(9) | 0.712(6) |
| D4(2a) | 0 | 0.882(9) | 0.036(6) |
| D5(4b) | 0.216(6) | 0.584(6) | 0.952(6) |
| D6(4b) | 0.272(6) | 0.937(6) | 0.304(6) |
| D7(2a) | 0 | 0.072(9) | 0.584(9) |
| D8(2a) | 0 | 0.564(12) | 0.172(9) |

### 3.1.3. *$YMn_2 - H_2$ System*

The intermetallic $RMn_2$ compounds with Laves phase have been intensively discussed and reported because of its interesting structural and magnetic properties. Another reason is their potential application as hydrogen storage materials which store up to 4.5 H atoms per formula unit at relatively low pressures and temperatures [34,35,36]. The Mn-Mn distance in these compounds plays a significant role to induce a Mn magnetic moment. The hydrogenation can be considered as the application of a negative chemical pressure; it causes a large increase of lattice parameters and consequently the Mn-Mn distance. Thus, it is expected that $RMn_2H_x$ hydrides would exhibit a variety of interesting physical and chemical properties. $YMn_2H_x$ crystallizes

in the cubic C15 type Laves phase (*Fd m* space group) up to x = 3.5 with a continuous increase of the unit cell volume, while the hydrogen atoms are distributed at the 96g Y2Mn2 sites. For 3.5 < x < 4 a two phase range with a mixture of cubic C15 and rhombohedral phases is observed. For 4 ≤ x < 4.3 a single phase hydride with rhombohedral structure (*R3m* space group) was found [34,35,36,37].

Recently it was discovered that the space group of $RMn_2$ exposed to higher hydrogen pressure at higher temperature is drastically changed. For instance $YMn_2H_6$ with *Fm m* space group appeared during hydrogenation at 170 MPa and 473 K. Moreover it was revealed that formation of $YMn_2H_6$-type structure can be obtained equally starting from the C14 or C15 structure (Table 3.6) of the parent samples [5]. In the unit cell of cubic $YMn_2$ with C15 structure, the corners are occupied by Y atoms whereas in cubic $YMn_2H_6$ they are occupied by manganese (Fig. 3.5). The unit cell of this hydride has four formula units. In other words, there are four Y, eight Mn and 24-H atoms. Important feature is that the hydrogen or deuterium atoms are not located in the interstitial sites (R2Mn2 or RMn3) like in $YMn_2H_x$ (x<4.5) but form octahedra around the Mn atoms in 4a positions. The second Mn is randomly distributed with yttrium in 8c position [3].

$RMn_2H_6$ can be classified as isostructural with $M_2TH_6$ hydrides where *M* is an alkaline earth (*M* = Mg, Ca, Sr) or a divalent rare earth metal (*M* = Eu, Yb) and *T* is a transition metal (*T* = Fe, Ru, Os). For these hydrides the parent intermetallic compounds like $TM_2$ do not exist and therefore direct hydride formation is not possible [38,39]. They are synthesized by annealing of transition metal with an alkaline metal hydride in hydrogen atmosphere. However, the synthesis of $RMn_2H_6$ has been achieved by direct reaction of an intermetallic compound with hydrogen (deuterium). Concerning the nature of the Mn-D bonds it can be noticed that the Mn-D distance is close to those observed in other $M_2TH_6$ [3,39]. These hydrides can therefore be considered as coordination compounds rather than interstitial metal hydrides just like these $M_2TH_6$ compounds which are described as complex anions $TH_6^{4-}$ surrounded by a cage of divalent $M^{2+}$ cations.

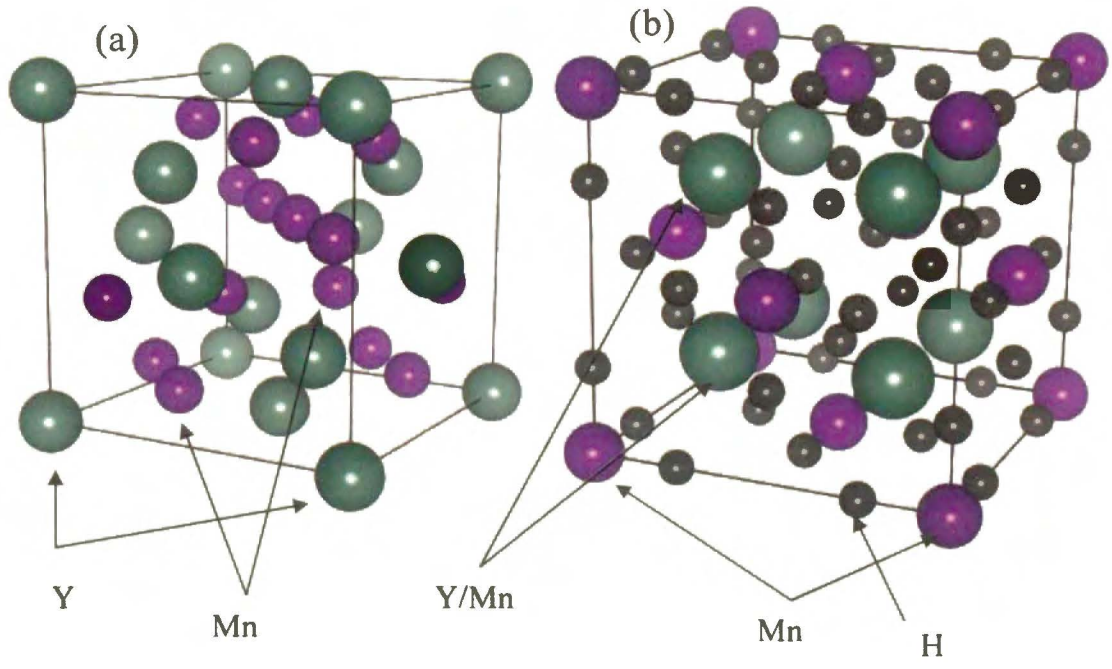


**Fig. 3.5. Schematic representation of crystal structure (a) $YMn_2$ with C15 structure with space group *Fd$\bar{3}$m* and (b) $YMn_2H_6$ with space group *Fm3m* [5,38]**

**Table 3.6. Structural properties of $RMn_2$ and $RMn_2D_6$ compounds (R=Er, Y, Ho and Dy) [5]**

| Sample | Space group | Unit cell parameter (nm) | | Unit cell volume ($nm^3$) | Ref. |
|---|---|---|---|---|---|
| | | *a* | *c* | | |
| $YMn_2$ (C15) | *Fd$\bar{3}$m* | 0.768 | - | 0.453 | [5] |
| $YMn_2D_6$ | *Fm$\bar{3}$m* | 0.669 | - | 0.299 | [38] |
| $DyMn_2$ (C15) | *Fd$\bar{3}$m* | 0.759 | - | 0.437 | [3] |
| $DyMn_2$ (C14) | *P6$_3$/mmc* | 0.536 | 0.874 | 0.217 | [3] |
| $DyMn_2D_6$ | *Fm$\bar{3}$m* | 0.672 | - | 0.303 | [3] |
| $HoMn_2$ (C15) | *Fd$\bar{3}$m* | 0.754 | - | 0.429 | [5] |
| $HoMn_2$ (C14) | *P6$_3$/mmc* | 0.533 | 0.869 | 0.214 | [5] |
| $HoMn_2D_6$ | *Fm$\bar{3}$m* | 0.668 | | 0.298 | [5] |
| $ErMn_2$ (C14) | *P6$_3$/mmc* | 0.529 | 0.864 | 0.210 | [5] |
| $ErMn_2D_6$ | *Fm$\bar{3}$m* | 0.668 | - | 0.298 | [5] |

## *3.2. $Y_6Mn_{23}$ and $YMn_{12}$ Compounds*

### 3.2.1. *$Y_6Mn_{23}$ – $H_2$ System*

$Y_6Mn_{23}$ is a face centered cubic (fcc) compound isostructural with $Th_6Mn_{23}$, which has the space group $Fm\bar{3}m$ [23]. Fig. 3.6 shows schematic representation of the $Y_6Mn_{23}$ compound, based on reported lattice parameter and atomic positions [40,41,42]. According to J.V. Florio et. al. [40], there are 4 formula units (116 atoms) in one unit cell and three different twenty-four-fold positions: 24*d* and *e* of space groups $Fm\bar{3}m$ and *F43*, and 24*g* of $F\bar{4}3m$ [40]. In addition, 24*f* of $F\bar{4}3m$ is equivalent to 24*e* of the other groups. The twenty-four yttrium atoms belong to these symmetries.

After exposure of $Y_6Mn_{23}$ to hydrogen (deuterium) gas at 6.2 MPa in conventional volumetric apparatus, the concentration of hydrogen corresponded to x = 24 ~ 25 in $Y_6Mn_{23}H_x$ and the parent structure remained unchanged within this concentration range [23,43].

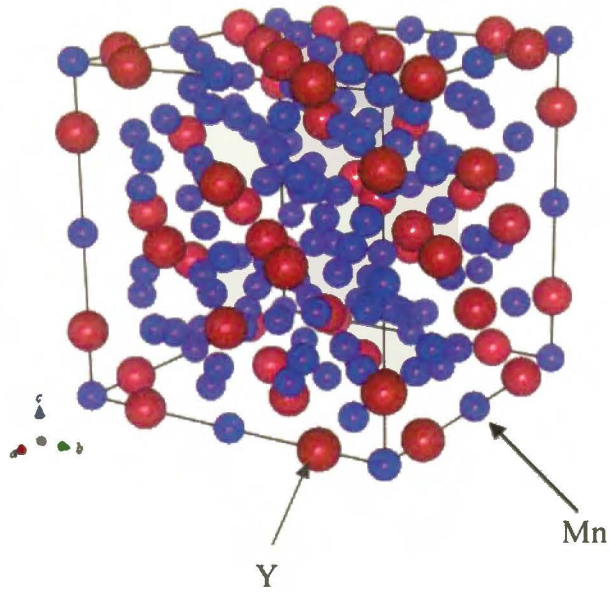


**Fig. 3.6. Schematic representation of crystal structure of $Y_6Mn_{23}$; atomic positions are based on Ref. [40].**

### 3.2.2. *$YMn_{12}$ – $H_2$ System*

$YMn_{12}$ has tetragonal structure isostructural with $ThMn_{12}$ with *I4/mmm* space group. According to J.V. Florio et. al., Th and Mn atoms occupy 2*a* site and 8*f*, 8*i*, 8*j* site, respectively [40]. Fig. 3.7 shows schematic representation of $YMn_{12}$ based on the atomic positions of $ThMn_{12}$; there are 2 formula units in one unit cell [40].

Unfortunately, according to our knowledge, there are no reports about hydrogen absorption properties of $YMn_{12}$, S. Obbade et. al. [44] carried out hydrogenation up to 1 MPa on $YFe_{11}Ti$ isostructural with $YMn_{12}$ structure and obtained $YFe_{11}TiH_{1.8}$. However, the unit cell volume showed only a simple expansion without any structural changes.

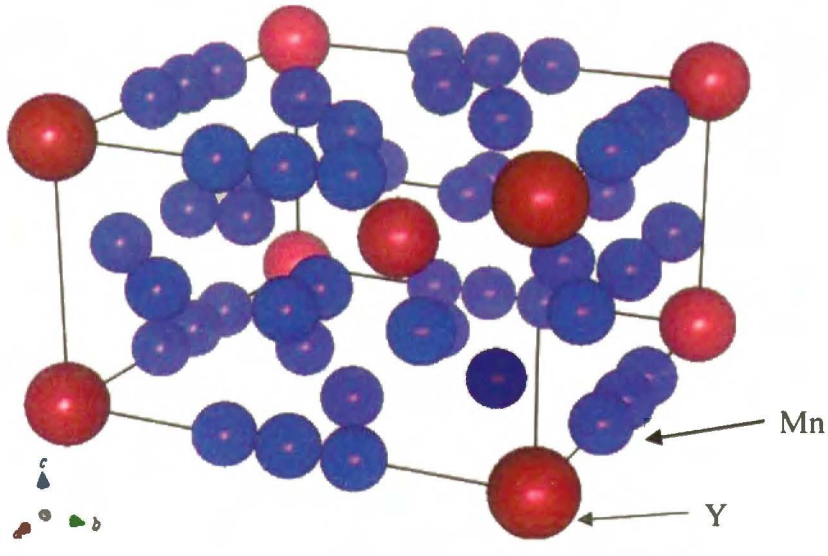


**Fig. 3.7. Scheme of $YMn_{12}$ structure.**

## *3.3. $R_7T_3$ Intermetallic Compounds*

### 3.3.1. *Crystal Structure of $R_7T_3$ Compounds*

$R_7T_3$ intermetallic compounds (R: rare earths and T: transition metals) were investigated extensively at beginning of 1970's by G. L. Olcese and A. Raman. According to them, all the R metals can form 7:3 phase with Rh atoms with $Th_7Fe_3$-type structure (Table 3.7) except R = Eu, Tm, Yb and Lu as shown in Fig. 3.8 [45]. Fig. 3.9 shows the structure with hexagonal (hcp) $P6_3mc$ space group, R atoms occupy three inequivalent positions indicated R(1), R(2) and R(3). There are two formula units in one unit cell [46]. As shown in Fig. 3.10, the unit cell volume decreases with increasing periodic number of rare earth [45,46] what is caused by lanthanide contraction which occurs due to unoccupied $4f$ orbital and occupied $5d$ and $6s$ orbitals with electrons. Subsequently, the attraction between nucleus and electrons becomes stronger with increasing the number of $4f$ electrons, and thus atomic or ionic radii of lanthanides decrease.

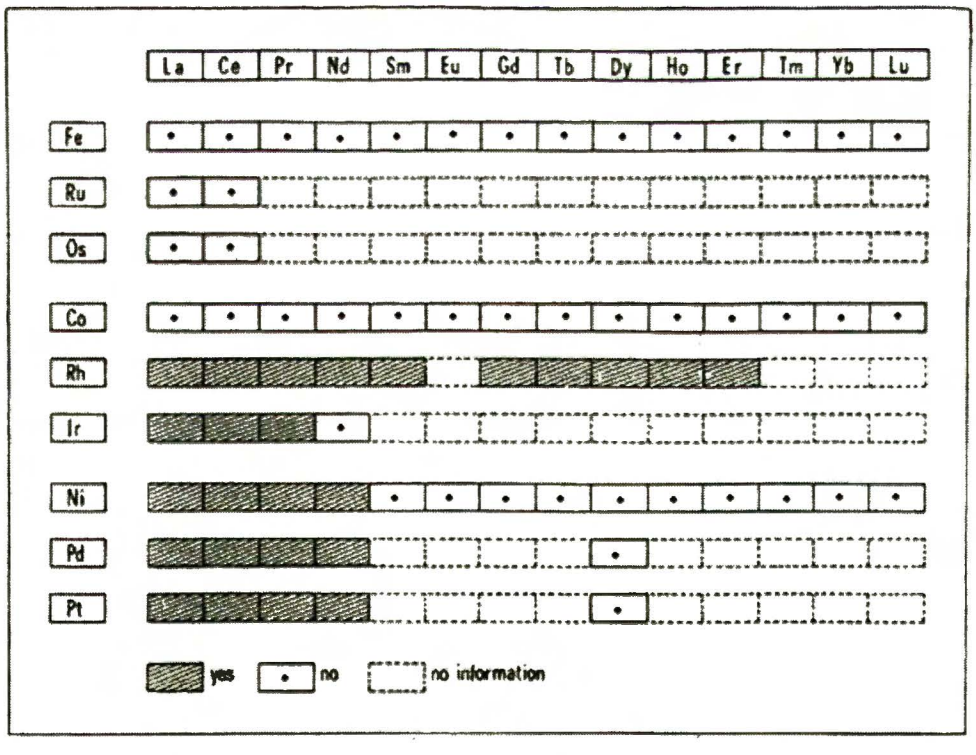


**Fig. 3.8. Occurence of the $R_7T_3$ compouds [45]**

**Table 3.7. Structural properties of $R_7Rh_3$ compounds [45]**

| Compounds | Structure type | Lattice parameters (nm) | | | Unit cell volume ($nm^3$) |
|---|---|---|---|---|---|
| | | *a* | *c* | *c/a* | |
| $La_7Rh_3$ | $Th_7Fe_3$ | 1.019 | 0.650 | 0.638 | 0.585 |
| $Ce_7Rh_3$ | $Th_7Fe_3$ | 1.002 | 0.638 | 0.636 | 0.555 |
| $Pr_7Rh_3$ | $Th_7Fe_3$ | 1.001 | 0.635 | 0.634 | 0.551 |
| $Nd_7Rh_3$ | $Th_7Fe_3$ | 0.998 | 0.631 | 0.632 | 0.544 |
| $Sm_7Rh_3$ | $Th_7Fe_3$ | 0.989 | 0.625 | 0.631 | 0.530 |
| $Gd_7Rh_3$ | $Th_7Fe_3$ | 0.985 | 0.618 | 0.627 | 0.520 |
| $Tb_7Rh_3$ | $Th_7Fe_3$ | 0.979 | 0.616 | 0.629 | 0.511 |
| $Dy_7Rh_3$ | $Th_7Fe_3$ | 0.975 | 0.611 | 0.626 | 0.503 |
| $Ho_7Rh_3$ | $Th_7Fe_3$ | 0.969 | 0.610 | 0.629 | 0.496 |
| $Er_7Rh_3$ | $Th_7Fe_3$ | 0.966 | 0.606 | 0.628 | 0.490 |

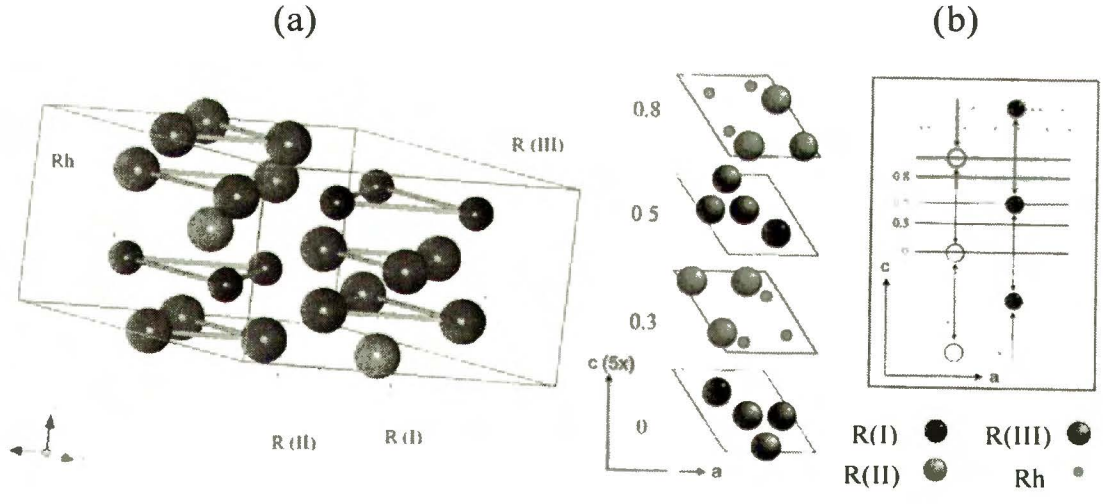


**Fig. 3.9. Schematic representation of (a) an unit cell of $R_7Rh_3$-type structure and (b) one unit cell with expanded the c axis scale [46]**

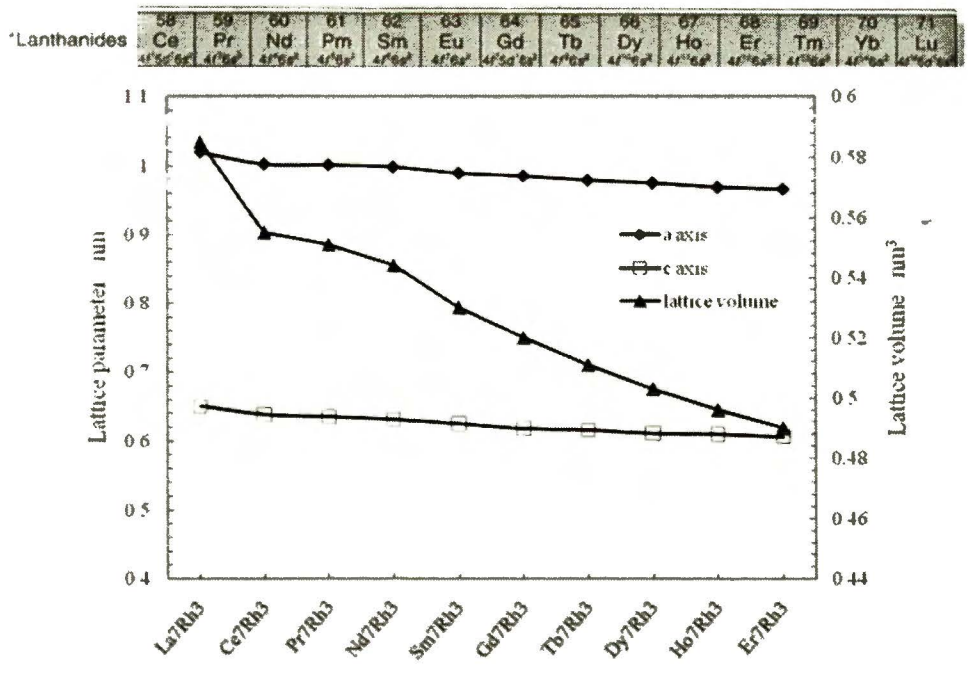


**Fig. 3.10. Periodic table of lanthanides and unit cell volumes of several $R_7Rh_3$ compounds [45]**

### 3.3.2. *Hydrogen Absorption in $R_7T_3$ Compounds*

Hydrogenations of $R_7T_3$ compounds have been investigated for a long time. The compounds are usually capable to absorb large quantities of hydrogen even under low pressure. Hydride formation is followed with a strongly exothermic reaction. For $La_7Ni_3$ hydrogenated at 5 MPa and room temperature P. Fischer and G. Busch et. al. found decomposition into $LaH_3$ and $LaNi_5$ [47,48]. In their study, the following decomposition process was proposed.

$$5La_7Ni_3 + 48H_2 \rightarrow 5La_7Ni_3H_{19.2} \rightarrow 32LaH_3 + 3LaNi_5 \qquad (3.1)$$

For $Th_7Fe_3$, $Th_7Co_3$ and $Th_7Ni_3$ hydrogenated by E. B. Boltich and coworkers at 4 MPa the hydrogen concentration was measured by using volumetric apparatus giving following hydrides formula: $Th_7Fe_3H_{30}$, $Th_7Co_3H_{21}$ and $Th_7Ni_3H_{24}$ [49]. However, XRD analyses of these hydrides showed not hexagonal peak patterns but only three or four peaks for all the hydrides [49,50]. Taking into account the decrease of the number of peaks in their XRD analyses, it seems that the hydrides were also decomposed into $ThH_x$ and other species like in the case of $La_7T_3$ alloys [48,50] (T: Transition metals). This could be related to high stability of $ThH_x$ and quick introduction of high pressure hydrogen gas to the samples. Fischer et. al. [47] confirmed the decomposition of $La_7Ni_3$ treated with deuterium into $LaNi_5D_x$ and $LaD_3$. Unfortunately Boltich et. al. [49] even did not show their XRD data for $Th_7T_3H_x$.

### 3.3.3. *Magnetic Properties of $R_7Rh_3$ Intermetallics*

Magnetic properties of $R_7T_3$ compounds have been investigated extensively for a long time since fundamental magnetic properties of rare earths depend on the number of 4*f* electrons (Chap. 3.2.1) and the empirical data are in good agreement with theoretical calculations. For example, T. Tsutaoka and coworkers have investigated magnetic properties of many $R_7Rh_3$ series intermetallics and calculated their *gJ* values (*g*: Landé's *g*-factor, *J*: total angular momentum) [51,52,53,54,55] which show magnitude of a magnetic moment of the rare earth ions. *J* is the sum of total orbital angular momentum *L* and total spin angular momentum *S* (thus, $J = L + S$), while *g*-factor for lanthanide ions is defined as [56]

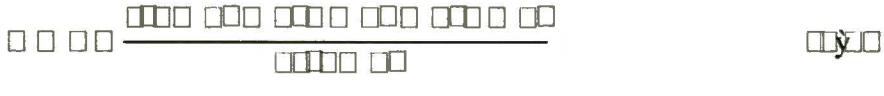

*gJ* value shows magnitude of magnetic moment evaluated using Bohr magneton. In the case of $Dy^{3+}$, this value is 10. It means that each dysprosium atom has 10 $\mu_B$ when all magnetic moments in the atom are aligned in the magnetic field.

Fig. 3.11 shows the magnetic susceptibilities of $Tb_7Rh_3$, $Dy_7Rh_3$ and $Ho_7Rh_3$ as a function of temperature at magnetic field $H$ = 11 kOe [51]. A susceptibility change of $Dy_7Rh_3$ and $Ho_7Rh_3$ are similar. According to T. Tsutaoka, $Dy_7Rh_3$ and $Ho_7Rh_3$ exhibit antiferromagnetic properties below $T_N$ = 56 K and 34 K, respectively. These compounds also show spontaneous magnetization below $T_C$ = 34 K for $Dy_7Rh_3$ and 20 K for $Ho_7Rh_3$.

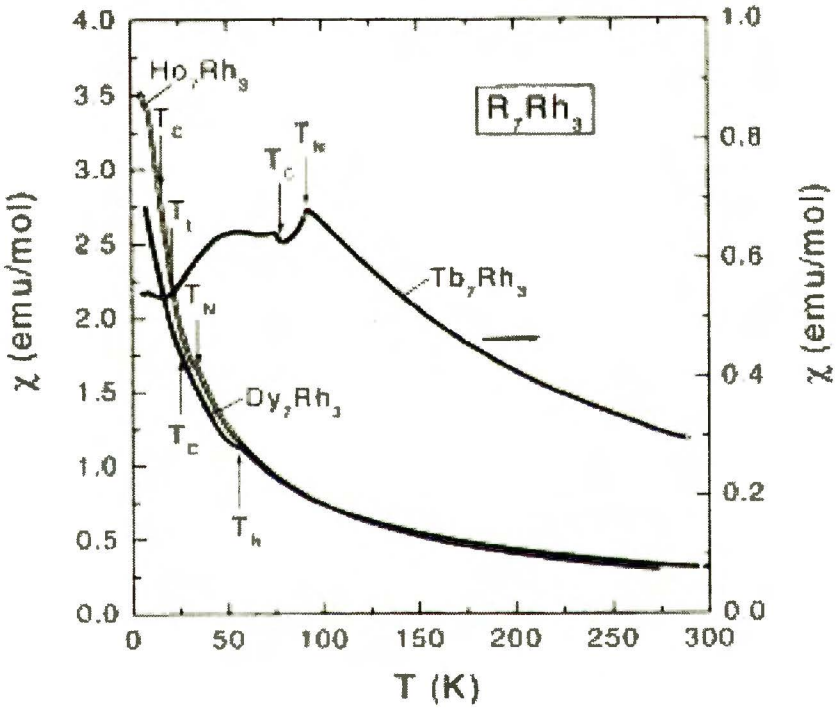


**Fig. 3.11. Magnetic susceptibility of $Tb_7Rh_3$, $Dy_7Rh_3$ and $Ho_7Rh_3$ as a function of temperature. $T_N$, $T_C$ and $T_t$ indicate the transition temperatures [51].**

On the other hand, the $Tb_7Rh_3$ shows reentrant magnetism (antiferromagnetic, ferrimagnetic and another antiferromagnetic phase) with transition temperatures $T_N$, $T_C$ and $T_t$ equal to 91, 74 and 24 K, respectively. At high temperature region, the $\chi$-T curves show Curie – Weiss behavior. The effective magnetic moments determined from the reciprocal magnetic susceptibilities are in fair agreement with values for the free trivalent R ions.

Fig. 3.12 shows magnetization curves (a) in the *c*-plane and (b) along the *c*-axis at various temperatures in $Ho_7Rh_3$ [52]. In the figure (a), a ferromagnetic character can be seen in temperature range between 4.2 K and 20 K where magnetization increases steeply with increasing magnetic field up to 10 kOe. This means that a spontaneous magnetization exists below 20 K, and this temperature corresponds to the magnetic transition point $T_C$ shown in Fig. 3.11. Along the *c*-axis (Fig. 3.12 (b)), magnetization increases markedly at H = 6 kOe below 20 K. It is called "metamagnetic transition"; in this transition electron spins rotate suddenly as to align in the direction of magnetic field. This critical field does not show any pronounced change with increasing temperature and disappears at 20 K.

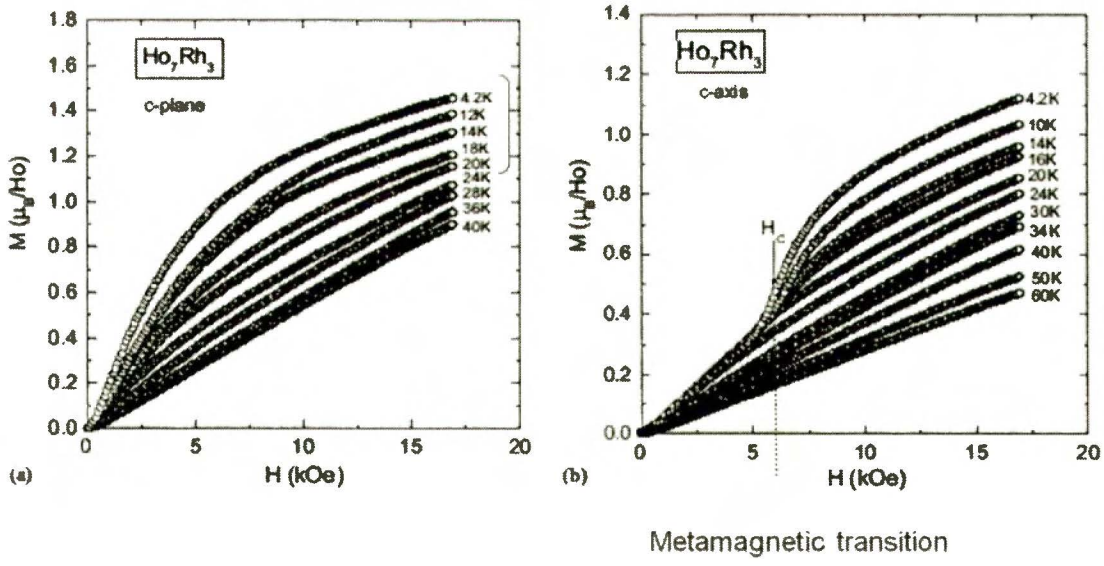


**Fig. 3.12. Magnetization curves of $Ho_7Rh_3$ (a) in the *c*-plane and (b) along the *c*-axis at various temperatures [52]**

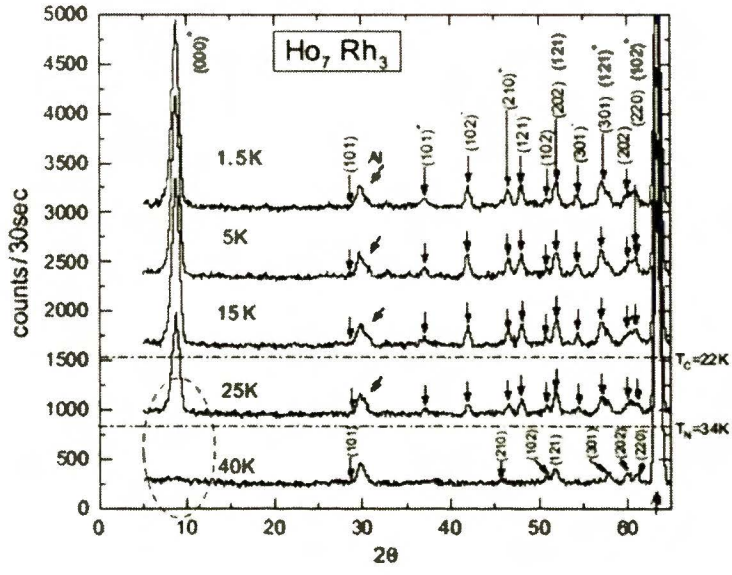


**Fig. 3.13. Powder neutron diffraction patterns of $Ho_7Rh_3$ at various temperatures [52]**

Fig. 3.13 shows the neutron diffraction patterns of $Ho_7Rh_3$ at various temperatures. A strong $(0,0,0)^{\pm}$ reflection is observed at $2\theta = 8.724°$ and $T = 1.5$ K. Since the magnetization measurements suggest the existence of an antiferromagnetic component in the principle plane, it may indicate a helically modulated magnetic structure along the *c*-axis.

As shown in Fig. 3.11, the$Tb_7Rh_3$ single crystal transforms from paramagnet to antiferromagnet at $T_N = 91$ K, then to ferromagnet at $T_C = 73$ K and to another antiferromagnet at $T_t = 27$ K. Fig. 3.14 shows the magnetization curves along the c-axis (a) and in the c-plane (b) at various temperatures [53]. At 4.2 K, the magnetization increases linearly with the magnetic field up to 17 kOe, and is far from the theoretical $gJ$ value of 9.0 $\mu_B$ for $Tb^{3+}$ for both axes. In Fig. 3.14 (a) a small residual magnetization (0.04 $\mu_B$/Tb at 35 K) and hysteresis appear in the temperature range between 27 and 75 K along the *c*-axis. Simultaneously, a metamagnetic transition is observed in the temperature range from 35 to 70 K. Thus, a ferrimagnetic state, with a small magnetic moment along the *c*-axis, exists in this temperature range. As seen in Fig. 3.14 (b), the magnetization in the *c*-plane increases linearly with

increasing magnetic field up to 17 kOe at all temperatures and the slope of magnetization against magnetic field has a maximum at about 95 K. This indicates that the basic magnetic structure in the *c*-plane is antiferromagnetic below 95 K. In Fig. 3.15 and 3.16, three successive metamagnetic transitions with large hysteresis were observed in the measurement of the high-field magnetization of polycrystalline $Tb_7Rh_3$ at 1.5 K [51,53]. This indicates that $Tb_7Rh_3$ is in an antiferromagnetic state at low temperature. The residual magnetization $M_R$, the critical metamagnetic field $H_C$ along the *c*-axis and the magnetization value $M_H$ at 17 kOe along the *c*-axis and in the *c*-plane can be seen on the figures. It is evident that three magnetic phases exist in $Tb_7Rh_3$: an antiferromagnetic phase at $T < T_t = 27$ K, a ferrimagnetic phase at 27 K $< T < T_C = 73$ K and another antiferromagnetic phase at 73 K $< T < T_N = 91$ K.

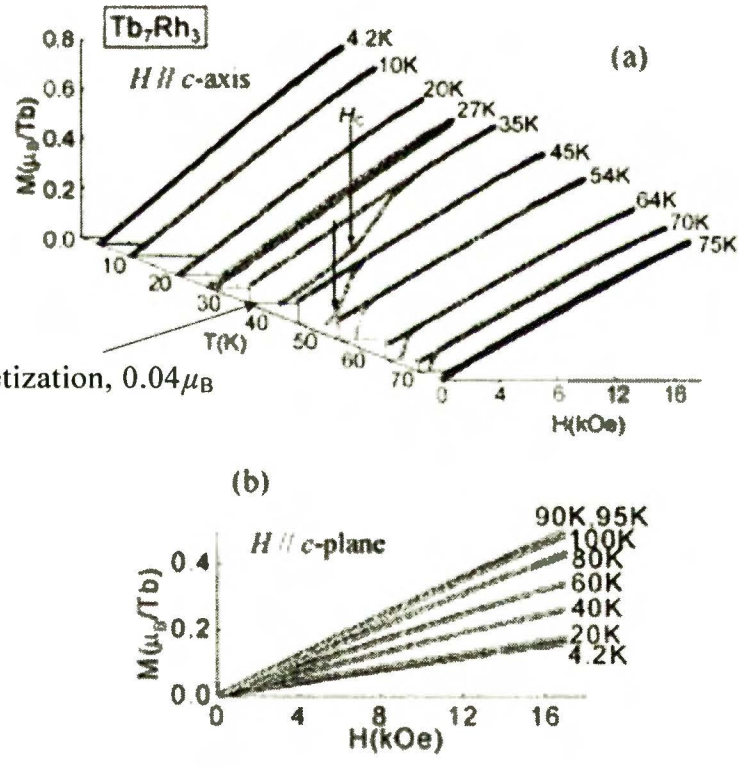


Residual magnetization, $0.04\mu_B$

**Fig. 3.14. Magnetization curves (a) along the *c*-axis and (b) in the *c*-plane at various temperatures [53]**

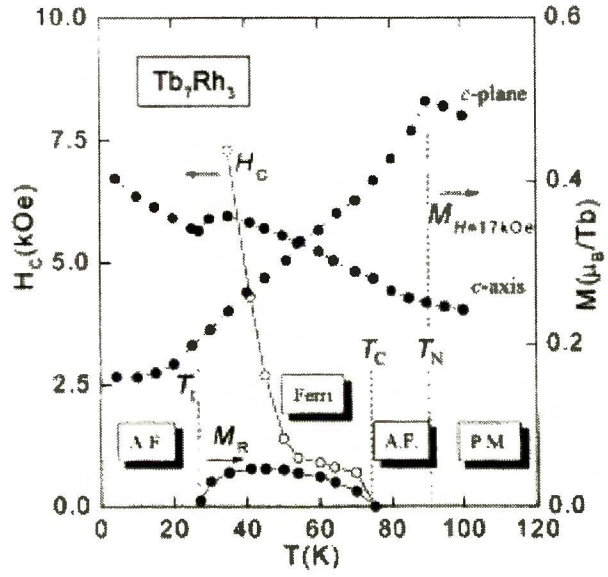


**Fig. 3.15. Temperature variation of the residual magnetization $M_R$, the magnetization value at $M_H$ = 17 kOe and critical metamagnetic field $H_C$ [53]**

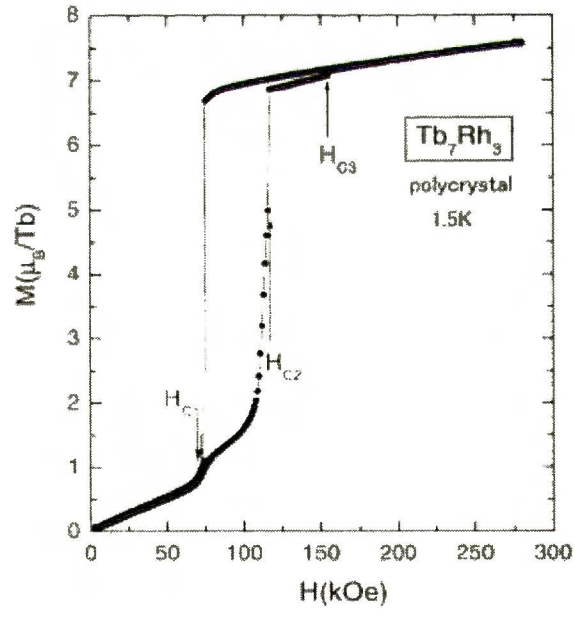


**Fig. 3.16. Magnetization curves for $Tb_7Rh_3$ at 1.5 K [51].**

The $R_7Rh_3$ compounds with light rare earth (R = Ce, Pr, Nd) show a ferromagnetic behavior and metallic transport properties at low temperature as reported in Ref. [46,54]. In contrary, $Sm_7Rh_3$ and heavy rare earth compounds (R = Gd, Tb, Dy, Ho and Er) show an antiferromagnetic behavior even though their metallic transport properties also appear at low temperature. This property is completely different from light rare earth compounds. For example, the negative temperature coefficient of $Y_7Rh_3$ in the high temperature region and the metallic conductivity at low temperature are of non-magnetic origin [53,55,57,58] (Fig. 3.17).

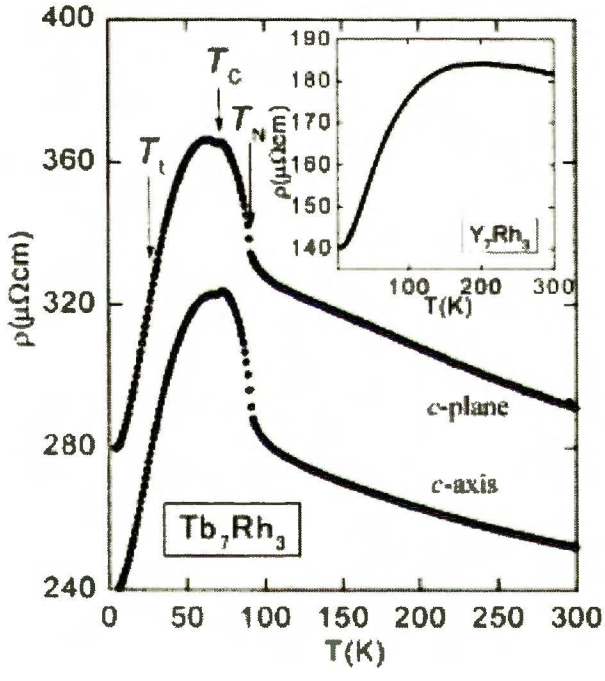


**Fig. 3.17. Electrical resistivity $\rho$ along the $c$-axis and in the $c$-plane of $Tb_7Rh_3$ as a function of temperature. The inset shows the temperature dependence of $\rho$ for a $Y_7Rh_3$ polycrystal [53].**

### 3.3.4. *Magnetic Properties of $R_7T_3$ Intermetallics with Hydrogen*

The $R_7T_3$ alloys interact with and can absorb hydrogen as explained in chap. 3.3.2. For example, $Th_7T_3$ compounds forms $Th_7T_3H_{30}$ by hydrogenation [49]. In such hydrogen rich hydrides the magnetic behavior is substantially different from that of the parent samples. Also the superconductivity behavior of metals is significantly altered. These various considerations aroused interest in studies to ascertain the influence of hydrogen on the behavior of the $R_7T_3$ systems.

$Th_7Fe_3$ readily absorbs hydrogen to the composition $Th_7Fe_3H_{30}$. The susceptibility of the host material is approximately $20 \times 10^{-3}$ emu $mol^{-1}$ $Oe^{-1}$ over the range 4 – 300 K. In contrast with this the hydride shows magnetization-temperature behavior characteristic of ferromagnetic (or ferrimagnetic) material (Fig. 3.18). The Curie temperature is above 300 K. The saturation magnetization measured at 4.2 K corresponds to 1.4 $\mu_B$ per atom of iron in the sample, what suggests that it is ferromagnetic.

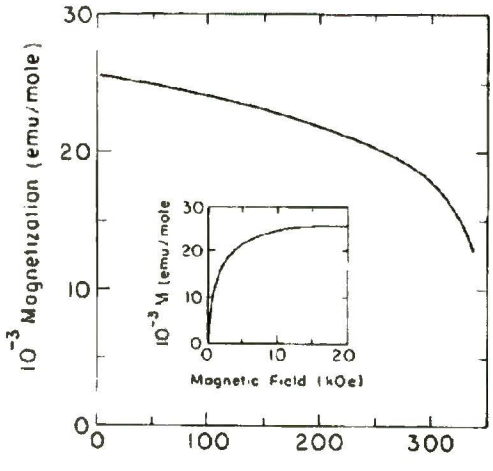


**Fig. 3.18. The magnetization - temperature behavior of $Th_7Fe_3H_{30}$ and in the inset the magnetization vs. magnetic field at 4.2 K [49].**

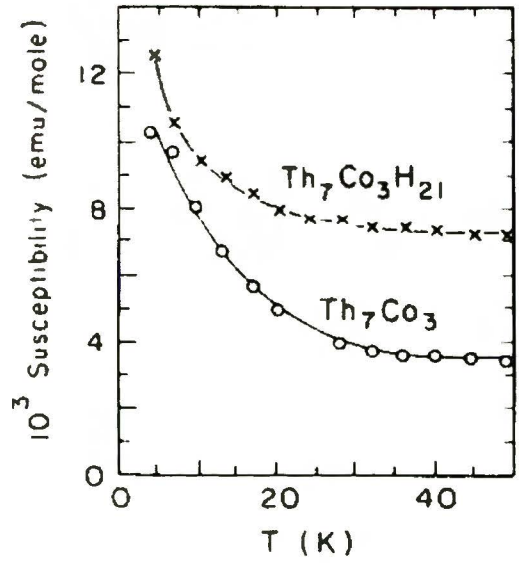


**Fig. 3.19. The temperature dependence of the susceptibility of $Th_7Co_3$ (○) and $Th_7Co_3H_{21}$ (×) below 50 K [49].**

The contrasting behavior of $Th_7Fe_3$ and its hydride is ascribed to the influence of hydrogen on the number of electrons in the d band. The band is filled in the host metal, rending the iron non-magnetic and the system as a whole a Pauli paramagnet. The discussed results suggest that hydrogen in effect captures electrons from the d band and this restores the iron moment, setting the stage for the ferromagnetic ordering which takes place below about 325 K.

Hydrogenated $Th_7Co_3$ readily absorbs hydrogen to form $Th_7Co_3H_{21}$. The susceptibilities of the host and hydride are shown in Fig. 3.19 for temperatures below 50 K. At higher temperatures both susceptibilities ware essentially constant.

Data for $Th_7Ni_3$ and its hydride are given in Fig. 3.20 and in Table 3.8. The behavior of the nickel compound is clearly at variance with that of the other two systems in that hydrogenation in this case decreases the susceptibility; obviously there is no indication of ferromagnetism.

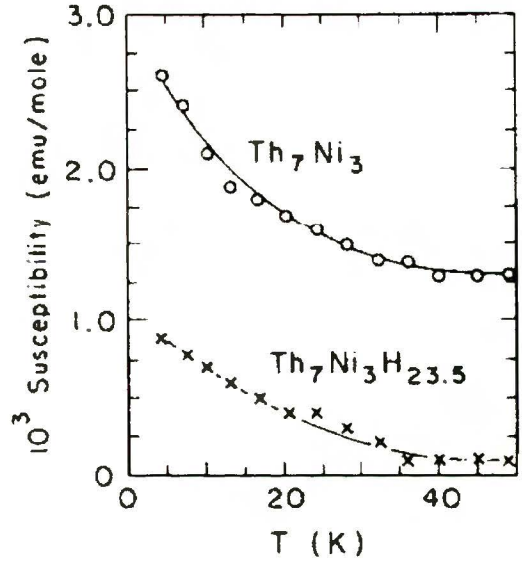


**Fig. 3.20 The temperature dependence of the susceptibility of $Th_7Ni_3$ (○) and $Th_7Ni_3H_{23.5}$ (×) below 50 K [49].**

**Table 3.8. Magnetic properties of $Th_7Fe_3$, $Th_7Co_3$ and $Th_7Ni_3$ and their hydrides. (pp=Pauli paramagnet) [49].**

| | Susceptibility ($\times 10^3$) at 300 K (emu/mol Oe) | $T_C$ (K) | $\mu_S$ at 4.2 K ($\mu_B$/f.u.) |
|---|---|---|---|
| $Th_7Fe_3$ | 20 | pp | 4.2 |
| $Th_7Fe_3H_{30}$ | - | ≈325 | |
| $Th_7Co_3$ | 3.5 | pp | |
| $Th_7Co_3H_{21}$ | 7.2 | pp | |
| $Th_7Ni_3$ | 1.3 | pp | |
| $Th_7Ni_3H_{24}$ | 0.1 | pp | |

# 4. Aim of Studies

In this study, we have aimed at followings;

(i) The assemblage of Sieverts' apparatus for high pressures and direct measurement of hydrogen absorption (*p-C* isotherms) in $Zr(Co_{1-x}Cr_x)_2$ and $Zr(Fe_{1-x}Cr_x)_2$ (x=0~0.9) at room temperature.

(ii) Hydrogenations of $ZrCo_2$-based pseudobinary alloys under high pressure and high temperature conditions, and structure analyses of the obtained hydrides.

(iii) High pressure deuterium treatment of $RFe_2$ (R = Ho, Dy, Tb and Gd) compounds at 373 K and structure analyses of the obtained deuterides in search of existence of orthorhombic $RFe_2D_5$ deuterides, or other phases with high deuterium content.

(iv) Syntheses of hydride from pseudobinary $(Y_{1-x}Dy_x)Mn_2$ alloys in order to check possibility of replacement of yttrium by rare earth element in 8c positions of $RMn_2H_6$ hydrides.

(v) Hydrogenations of $Y_6Mn_{23}$ and $YMn_{12}$ compounds under high pressure and high temperature conditions, aimed at syntheses of novel hydrides. Also verification of hypothesis that ratio of Y:Mn in 8c positions can be smaller than 1:1.

(vi) Hydrogenations of $R_7Rh_3$ (R=Y, La, Nd, Tb, Dy, Ho and Er) compounds at moderate and high pressures, and analyses of crystal structures of products in order to synthesize stable hydrides with possibly high hydrogen concentration. Measurements of magnetic properties of these hydrides.

In our laboratory, a main subject is synthesis of new hydrides and determination of their structures. However, we extended studies also for magnetic properties.

Moreover, *p-C* (pressure - composition) isotherms were measured by using Sieverts' apparatus which has been made for investigations of hydrogen concentrations in metals under high-pressure conditions.

The selection of materials to be treated by hydrogen at high hydrogen pressure, XRD measurements, structure refinement and *p-C* isotherm measurements have been done in the Institute of Physical Chemistry PAS. Selected properties of successfully synthesized novel hydrides were measured in the framework of collaboration with France, Japan and Taiwan.

# 5. Experimental Methods

## *5.1. Preparations of Samples*

All samples used in this study were selected by us. $Zr(Co_{1-x}Cr_x)_2$, $Zr(Fe_{1-x}Cr_x)_2$, $Zr(Co_xFe_{1-x})_2$, $(Y_{1-x}Dy_x)Mn_2$, $Y_6Mn_{23}$ and $YMn_{12}$ were prepared by Advanced Industrial Science and Technology (AIST) Kansai Centre in Osaka Japan. $RFe_2$ and $(Zr_xTi_{1-x})Co_2$ were prepared at Centre National de la Recherche Scientifique (CNRS) in France and National Taiwan University in Taiwan, respectively. These samples were made by using arc melting method, and their XRD confirmed cubic structure with C15 Laves phase space group $Fd\bar{3}m$ for $RFe_2$, $ZrCo_2$-based, $ZrFe_2$-based and $(Dy_xY_{1-x})Mn_2$ pseudobinary; cubic structure with space group $Fm\bar{3}m$ for $Y_6Mn_{23}$ and tetragonal structure with space group *I4/mmm* for $YMn_{12}$, respectively.

On the other hand, $R_7Rh_3$ compounds were prepared using arc melting method at Hiroshima University in Japan. XRD analyses of the obtained $R_7Rh_3$ compounds led to hexagonal structure with space group $P6_3mc$ as shown in Fig. 3.9.

All samples investigated in this study are listed in Table 5.1.

**Table 5.1. Samples investigated in this study.**

| System | Compound | Sample | Measurement |
|---|---|---|---|
| Zr-based alloys | $Zr(Cr_xCo_{1-x})_2$ | *$ZrCo_2$<br>*$ZrCr_{0.2}Co_{1.8}$<br>*$ZrCr_{0.5}Co_{1.5}$<br>*ZrCrCo<br>$ZrCr_{1.5}Co_{0.5}$<br>$ZrCr_{1.8}Co_{0.2}$<br>$ZrCr_2$ | High hydrogen pressure treatment, XRD measurement, *p-C* isotherm (*) |
| | $Zr(Cr_xFe_{1-x})_2$ | $ZrFe_2$<br>$ZrCr_{0.2}Fe_{1.8}$<br>$ZrCr_{0.5}Fe_{1.5}$<br>ZrCrFe | *p-C* isotherm |
| | Zr-Co-Fe | $ZrCo_{1.5}Fe_{0.5}$<br>$ZrCo_{0.2}Fe_{1.8}$ | High hydrogen pressure treatment, XRD and magnetic measurement |
| | $(Zr_{1-x}Ti_x)Co_2$ | $Zr_{0.9}Ti_{0.1}Co_2$<br>$Zr_{0.75}Ti_{0.25}Co_2$<br>$Zr_{0.5}Ti_{0.5}Co_2$<br>$Zr_{0.25}Ti_{0.75}Co_2$<br>$Zr_{0.1}Ti_{0.9}Co_2$ | |
| R (Y and rare earth) based alloys | $RFe_2$ | $DyFe_2$<br>$HoFe_2$<br>$TbFe_2$<br>$GdFe_2$ | High hydrogen pressure treatment, XRD |
| | $(Dy_{1-x}Y_x)Mn_2$ | $DyMn_2$<br>$Dy_{0.9}Y_{0.1}Mn_2$<br>$Dy_{0.75}Y_{0.25}Mn_2$<br>$Dy_{0.25}Y_{0.75}Mn_2$<br>$Dy_{0.1}Y_{0.9}Mn_2$<br>$YMn_2$ | High hydrogen pressure treatment, XRD measurement |
| | Y-Mn | $Y_6Mn_{23}$<br>$YMn_{12}$ | |
| | $R_7Rh_3$ | $Y_7Rh_3$<br>$Dy_7Rh_3$<br>$Ho_7Rh_3$<br>$Er_7Rh_3$<br>$Tb_7Rh_3$ | Low and high hydrogen pressure treatment, XRD and magnetic measurement |

## *5.2. Sieverts' Apparatus and Measurements of p-C Isotherms*

The *p-C* isotherms of $Zr(Co_{1-x}Cr_x)_2$ and $Zr(Fe_{1-x}Cr_x)_2$ compounds have been measured by Sieverts' apparatus which was made in our laboratory (Fig. 5.1). Tubes and valves (products of SITEC company) of this apparatus were made of austenitic stainless steel AISI 316Ti (modified SUS 316-type) which shows good resistance to hydrogen corrosion. Hydrogen gas pressure was measured by three sensors (for three different pressure ranges; 0.35, 20 and 70 MPa) connected to a monitor Druck DPI-145. Reaction vessel of Cu-Be alloy (made in Institute workshop according to our design), which endures high pressure hydrogen gas, was attached at the left side of the Sieverts' apparatus (Fig. 5.2). A sample for *p-C* isotherm measurement was placed in the vessel and exposed to hydrogen. The apparatus is connected to two pressure intensifiers via a capillary. Fig. 5.3 shows the intensifiers. Preliminary compression of hydrogen gas up to 100 MPa can be done by the left one (A) in Fig. 5.3. Further compression up to 1 GPa is possible applying compressor (B) in Fig. 5.3. However, the Sieverts' apparatus has been designed for pressures not exceeding 0.35 GPa.

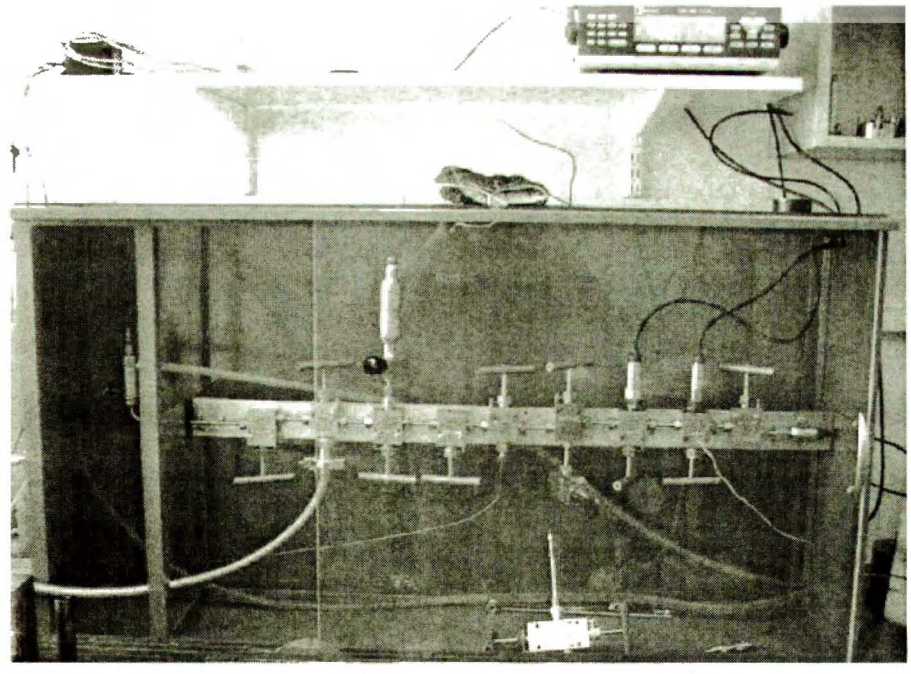

**Fig. 5.1. High-pressure type Sieverts' apparatus.**

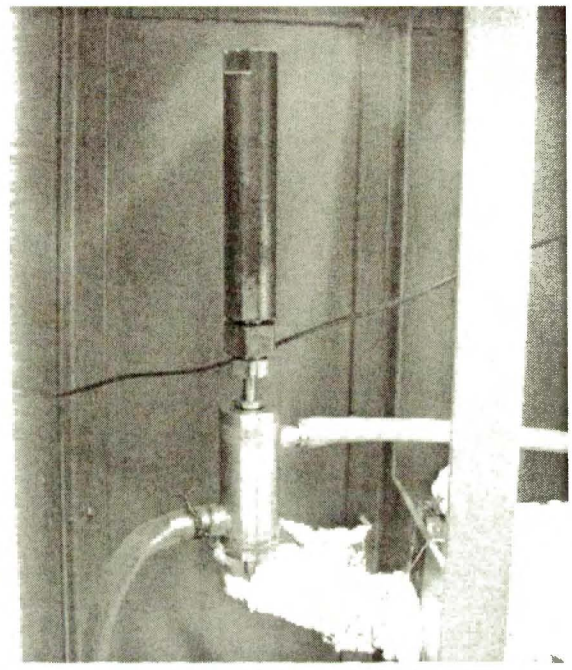

**Fig. 5.2. Reaction vessel made of Cu-Be alloy.**

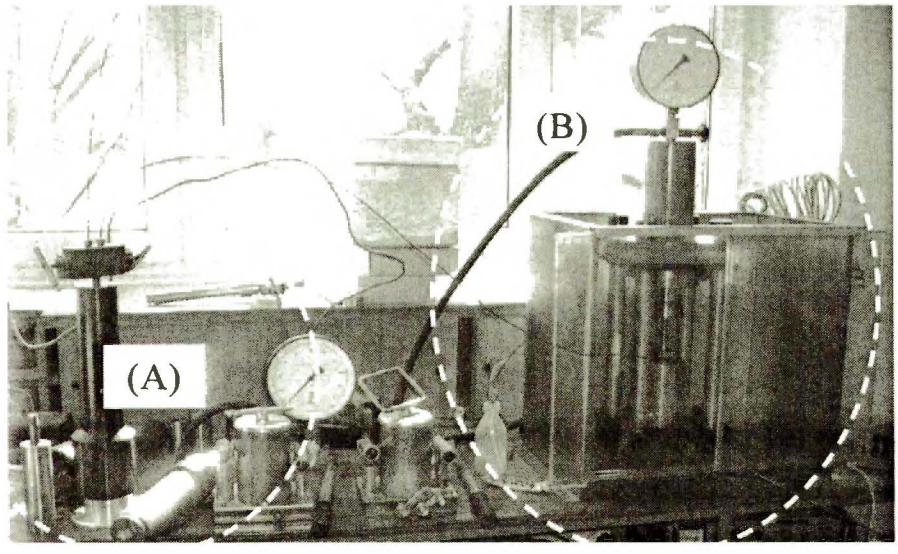


**Fig. 5.3. The pressure intensifiers connected to Sieverts' apparatus (Fig. 5.9) via capillary; (A) pressure intensifier to compress $H_2$ gas up to 100 MPa and (B) to compress the gas up to 1 GPa.**

Fig. 5.4 shows a scheme of the Sieverts' apparatus composed of hydrogen deposit part with the volume V1 and the reaction vessel with the volume V2. Before the measurement of *p-C* isotherm, an accurate weight of the sample and the volume V2 must be measured for further calculation of hydrogen concentration in the sample.

In this study, samples (usually about 0.5 g) were weighted by Mettler Toledo balance, and volume V2 with the sample was measured by using argon gas. After these preliminary measurements, the sample was heated in vacuum up to 473 K for 8 hours for surface activation. In general, the surface of metals or alloys exposed to atmosphere or low vacuum for long time may be covered with oxide layers or contaminated by residual gases [10,59,60,61,62] which should be removed. Fig. 5.5 shows the effect of heat activation on hydrogen absorption capacity of $Ti_{0.44}Zr_{0.56}Cr_{0.85}Fe_{0.7}Ni_{0.2}Mn_{0.25}Cu_{0.03}$ (Ti-Cr alloy) [62]. This alloy was put in a reaction vessel and charged with 0.68 MPa hydrogen gas at 293 K. At this initial stage, the alloy did not react with hydrogen due to contamination of its surface. Then, the sample heating was started. Initially the hydrogen pressure increased as temperature of reaction vessel increased up to 873 K. This temperature was maintained for 8 hours. During this time the hydrogen pressure gradually decreased what means that the sample became active and able to absorb hydrogen. After 8 hours, the furnace was turned off. When the temperature returned to 293 K, the hydrogen pressure became lower than before the heat activation. Consequently, from this difference of pressures the amount of absorbed hydrogen was calculated giving H/(Ti-Cr alloy) = 2.1.

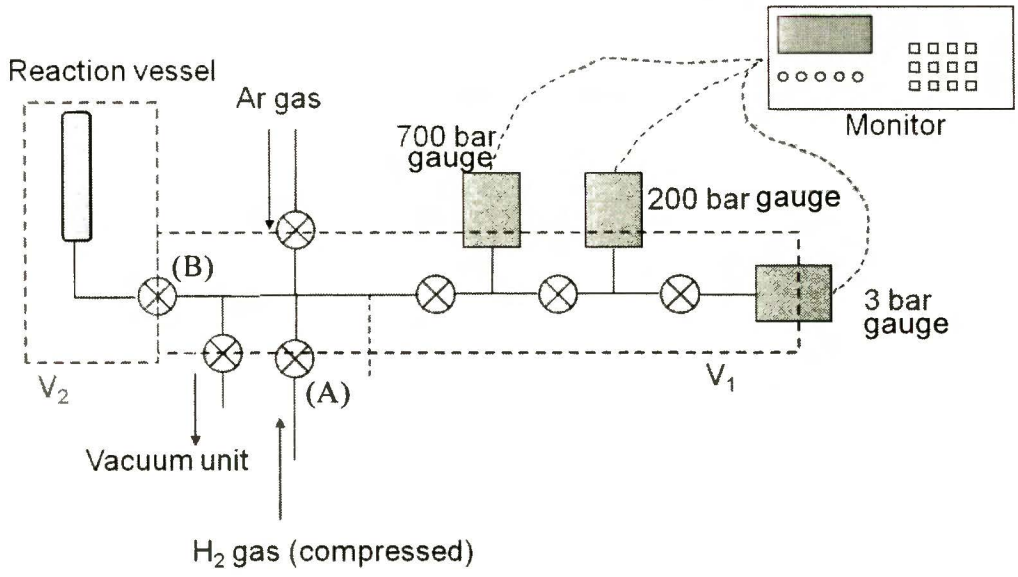


**Fig. 5.4. Scheme of the Sieverts' apparatus.**

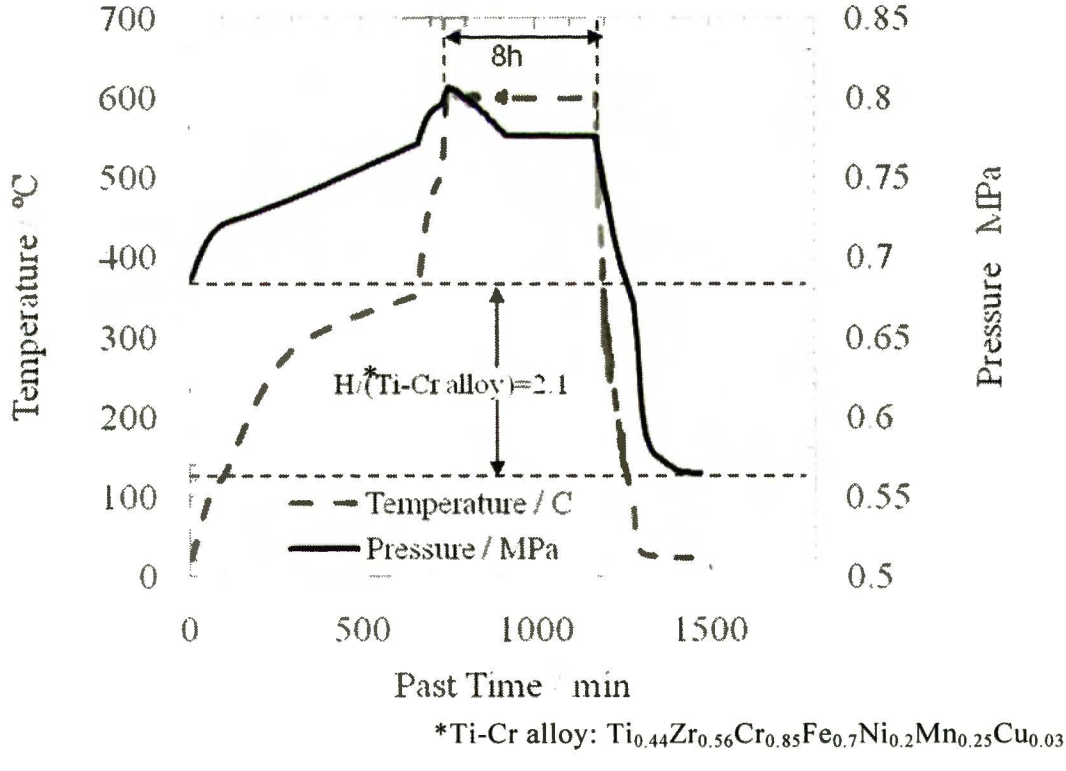


*Ti-Cr alloy: $Ti_{0.44}Zr_{0.56}Cr_{0.85}Fe_{0.7}Ni_{0.2}Mn_{0.25}Cu_{0.03}$

**Fig. 5.5. The effect of heat activation on capacity of hydrogen absorption in the $Ti_{0.44}Zr_{0.56}Cr_{0.85}Fe_{0.7}Ni_{0.2}Mn_{0.25}Cu_{0.03}$.**

Measurements of *p-C* isotherms by using Sieverts' apparatus shown in Fig. 5.4 were performed as follows;

(1) After evacuation of whole system, all valves were closed.

(2) By opening valve (A), hydrogen from pressure intensifier was conducted into the V1. Then the pressure $p(1)$ and the temperature $T(1)$ was measured.

(3) Next, by opening valve (B) the hydrogen gas flows from V1 into V2. After reaction is stopped, the equilibrium pressure $p(2)$ and the temperature $T(2)$ were measured.

(4) Amount of hydrogen absorbed in a sample was calculated from difference between $p(2)$ and $p(1)$ by using hydrogen fugacity and the equation of state.

(5) Having closed the valve (B), we introduce more hydrogen gas to V1 and repeat processes (2)~(5).

Thus, we can accurately evaluate hydrogen concentration during the measurements of *p*-C isotherms. It is especially convenient for alloys with high equilibrium pressure or high desorption rate as $LaNi_5$ for example [63].

## *5.3. Syntheses of Metal Hydrides*

Hydrogenations (or deuterizations) of investigated alloys have been carried out in the pressure range up to 1 GPa by using high-pressure compressor and other equipment in our laboratory. Primarily, the samples were crushed and put in small containers (Fig. 5.6) which then were placed in the high-pressure vessel made of Cu-Be alloy and high strength steel (Fig. 5.7). Then, they initially were kept in vacuum for 24 hours at 373 K. After that the hydrogen gas was introduced gradually from a pressure intensifier (Fig. 5.8) to initialize process of hydrogen absorption. When the pressure exceeded 70 MPa the connection with pressure intensifier has been closed and further compression of hydrogen (up to 1 GPa) proceeded only in the high pressure vessel placed under hydraulic press (Fig. 5.9). Synthesis of hydride at constant pressure and temperature was as long as several days (sometimes several months). Then the vessel was cooled down by liquid nitrogen to inhibit desorption of hydrogen from the hydrides, the pressure was released and samples were removed for further investigations. For instance, the crystal structures of the obtained hydrides were analyzed by Bruker XRD, WinPlotR and Socabim PDFMaint JCP2 as reference data.

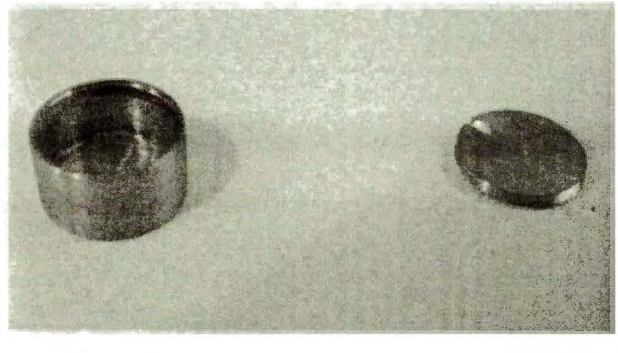

**Fig. 5.6. The container for samples ($\phi$ = 12mm).**

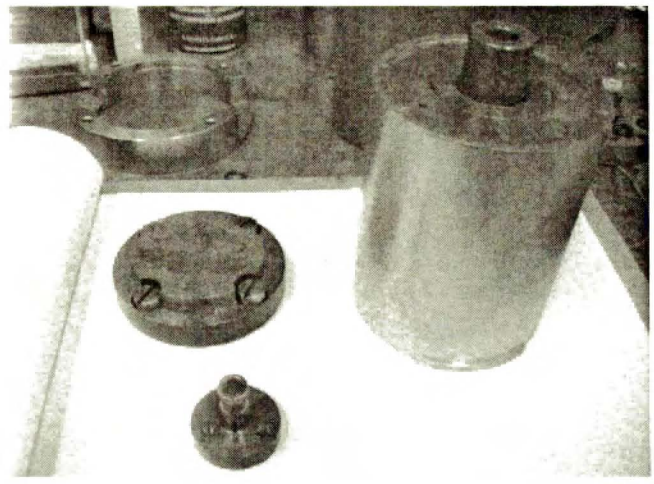

**Fig. 5.7. The high-pressure vessel.**

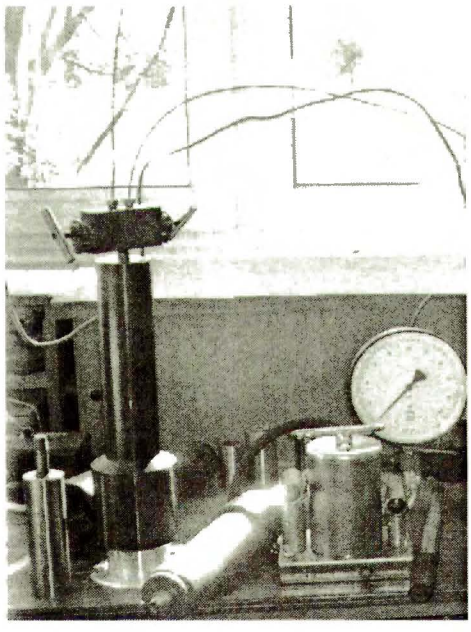

**Fig. 5.8. The pressure intensifier.**

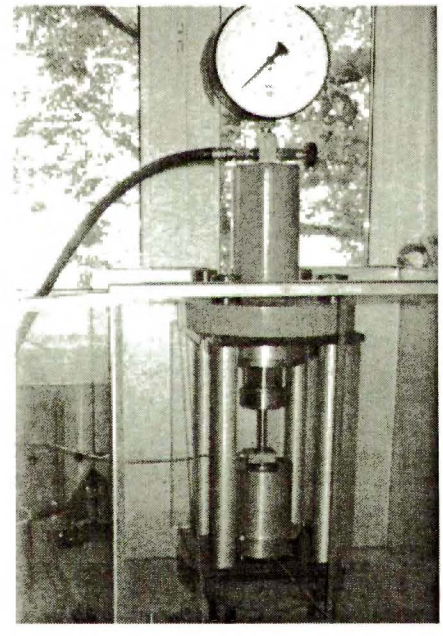

**Fig. 5.9. The high-pressure vessel under hydraulic press.**

# 6. Results and Discussion

## *6.1. Zr based Pseudobinary Laves Compounds – $H_2$ ($D_2$) Systems*

### 6.1.1. *p-C Isotherms of $Zr(Co_{1-x}Cr_x)_2$ and $Zr(Fe_{1-x}Cr_x)_2$ Compounds*

The *p-C* isotherms of hydrogen absorption in $Zr(Co_{1-x}Cr_x)_2$ (x=0~0.5) compounds have been measured at 293 K up to 70 MPa. Absorption and desorption isotherms are plotted in Fig. 6.1. The isotherm curve of $ZrCo_2$ did not show neither plateau nor β-phase formation within 70 MPa. However sample pulverized during the measurement due to small hydrogen uptake in the α-phase. The isotherm of $ZrCo_{1.8}Cr_{0.2}$ was located markedly below that of $ZrCo_2$ but also in this case pressure range was not sufficient to reach the plateau level.

Comparing to $ZrCo_2$ and $ZrCo_{1.8}Cr_{0.2}$, the equilibrium pressure of hydride formation in $ZrCo_{1.5}Cr_{0.5}$ decreased markedly. The plateau pressure of hydride formation lies between 2~3 MPa with maximum 1 MPa of absorption/desorption hysteresis. ZrCoCr showed the lowest equilibrium pressure and the highest hydrogen concentration (H/M > 1) among the isotherms of all hydrides in Fig. 6.1. The isotherm also showed large β-phase region above 0.08 MPa without second plateau up to 70 MPa.

From these results, it became clear that with increasing Cr contents the $Zr(Co_{1-x}Cr_x)_2$ hydrides tend to be more stable and contain more hydrogen.

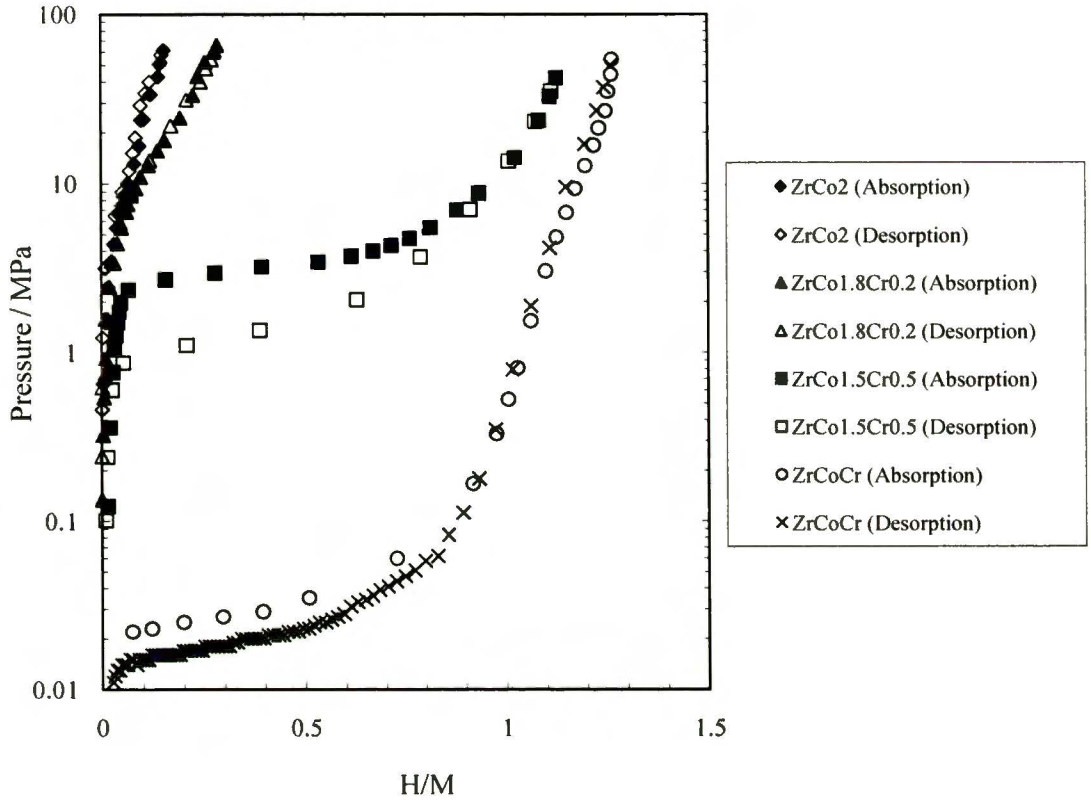


**Fig. 6.1. *p-C* isotherms of $Zr(Co_{1-x}Cr_x)_2$-$H_2$ system at 293 K up to 70 MPa.**

Fig. 6.2 shows *p-C* isotherms of $Zr(Fe_{1-x}Cr_x)_2$ compounds at 293 K up to 70 MPa. The isotherm of $ZrFe_2$ like $ZrCo_2$ did not show plateau in the measurement within 70 MPa. The α-phase of the sample exists up to 30 MPa and plateau region lies above 70 MPa. $ZrFe_{1.8}Cr_{0.2}$ showed α-phase, plateau and β-phase, and the compound absorbed hydrogen up to H/M > 1 within 70 MPa. In the case of $ZrCo_{1.8}Cr_{0.2}$, the β-phase did not appear and the maximum hydrogen concentration was only H/M = 0.3 in the same range of the pressure even though both compounds had the same Cr content. Plateau region of $ZrFe_{1.8}Cr_{0.2}$-$H_2$ extends between 4 and 8 MPa and above 8 MPa (H/M > 0.9) we have β-phase only.

Plateau pressure of $ZrFe_{1.5}Cr_{0.5}$ was placed around 0.3 MPa, and the maximum hydrogen concentration at 70 MPa was H/M = 1.2. ZrFeCr with the highest

Cr contentamong the investigated samples showed the lowest plateau pressure located around 0.01 MPa and the highest hydrogen concentration in Fig.6.9. The single α-phase part of isotherm of ZrFeCr was placed at pressures too low to measure by using our pressure system. Above plateau both $ZrFe_{1.5}Cr_{0.5}$ and ZrFeCr showed large β-phase regions with monotonic increase of H concentration up to 70 MPa.

From these results, it became clear that with increasing Cr content the equilibrium pressure decreases, while hydrogen absorption capacity and stability of the $Zr(Fe_{1-x}Cr_x)_2$ hydride increases. Comparing *p-C* isotherms of $Zr(Co_{1-x}Cr_x)_2$ and $Zr(Fe_{1-x}Cr_x)_2$, it could be concluded that at any particular value x, the plateau pressure of $Zr(Co_{1-x}Cr_x)_2$ is higher as shown in Fig. 6.10. This corresponds to the data reported about $ZrCo_2H_x$ and $ZrFe_2H_x$ compounds [28].

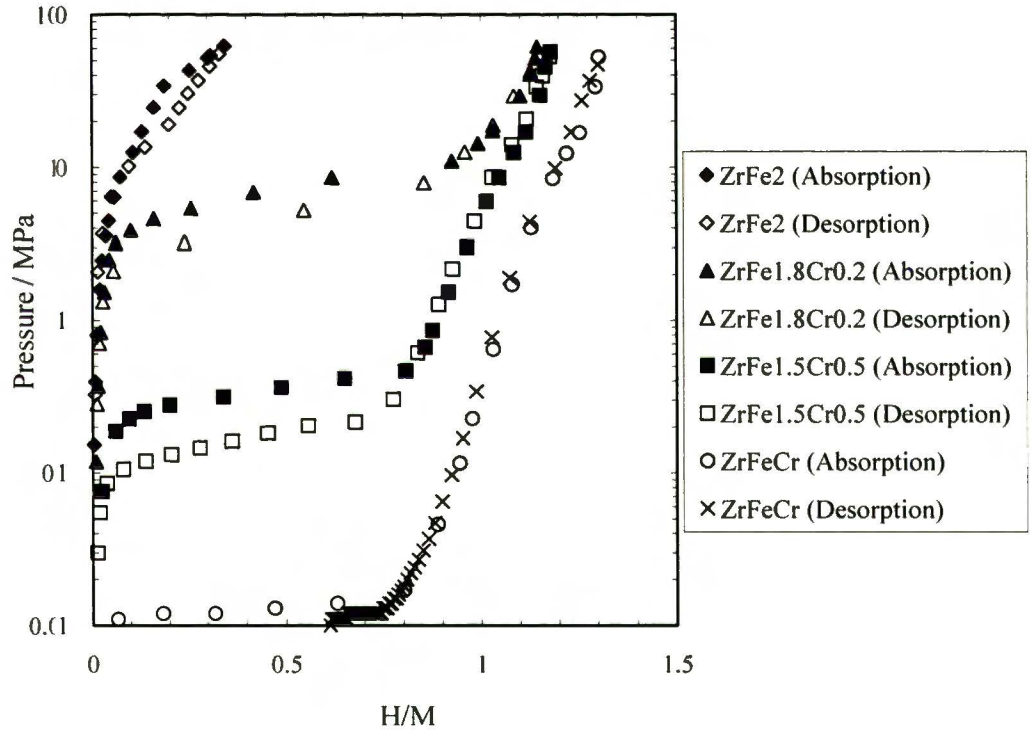


**Fig. 6.9. *p-C* isotherms of $Zr(Fe_{1-x}Cr_x)_2$ for hydrogen absorption and desorption at 293 K up to 70 MPa.**

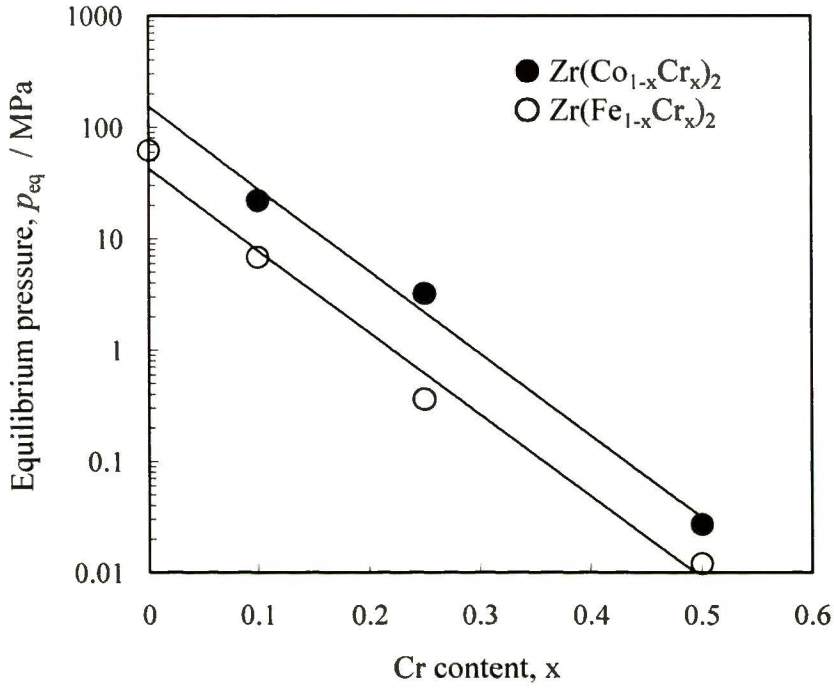


**Fig. 6.10. Change in equilibrium pressure at plateau (α- and β-phase) region of $Zr(Co_{1-x}Cr_x)_2$ and $Zr(Fe_{1-x}Cr_x)_2$ as a function of Cr content, x.**

## 6. .2. *Structure Changes of $Zr(Co_{1-x}Cr_x)_2$ by Deuterizations*

All $Zr(Co_{1-x}Cr_x)_2$ compounds (x = 0 ~ 1) were deuterized at 1 GPa and 373 K for 5 days. Fig. 6.1 shows XRD patterns of $ZrCo_2$ (x = 0) with cubic structure C15 Laves phase and its deuteride. The XRD pattern of the parent sample exhibited sharpened peaks and the positions corresponded to a reference Socabim PDFMaint JCP2. There is a report that small unidentified peak appears at 2θ = 51° of $ZrCo_2$ parent sample [64], but such peak did not appear in diffraction pattern of our sample. The deuteride was immediately immersed in liquid nitrogen and kept there until XRD measurement. The resulted peak pattern in Fig. 6.11 shows coexistence of two phases; deuteride phase and parent phase probably from deuteride decomposition. The synthesized deuteride peaks appear at 2θ = 34.9° and 41.4°, while peaks of the parent phase are

present at 2θ = 36.5°, 43.0° and 45.0°. The third peak of deuteride coincides with peak form parent phase at 43°. $ZrCo_2$ deuteride is not stable, thus it can be observed only immediately after high pressure deuterium treatments [27,28].

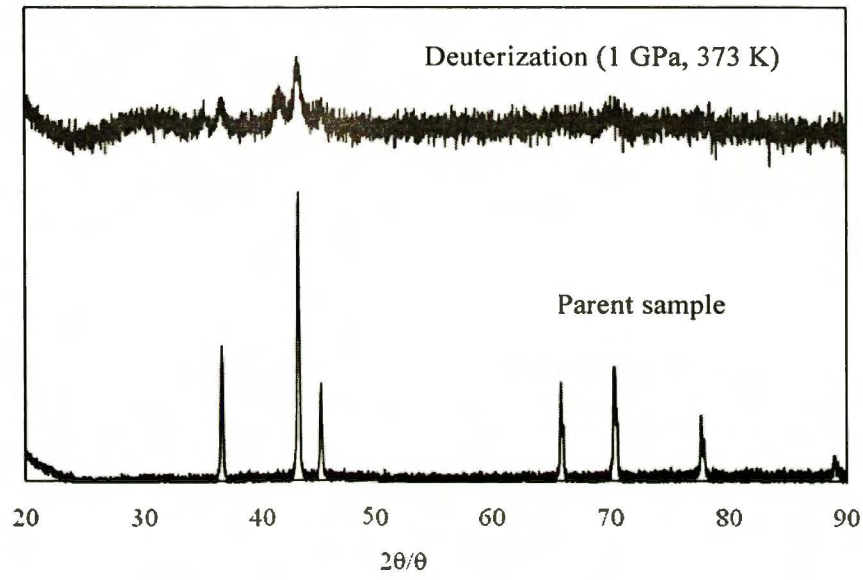


**Fig. 6.11. XRD patterns of $ZrCo_2$ before and after deuterization.**

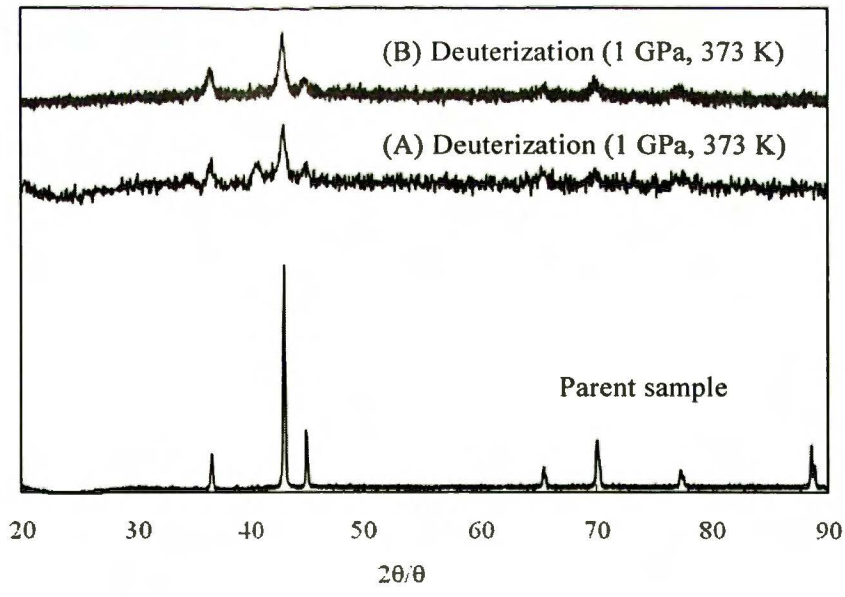


**Fig. 6.12. XRD patterns of $ZrCo_{1.8}Cr_{0.2}$ before and after deuterium treatment; (A) XRD analysis for 20 minutes and (B) XRD analysis for 2 hours.**

Fig. 6.12 shows peak patterns of cubic $ZrCo_{1.8}Cr_{0.2}$ parent sample and its deuteride. The diffraction pattern (A) was received short time (about 20 minute) after pressure release. It exhibits small deuteride peaks at $2\theta = 33.5^{\circ}$ and $40.2^{\circ}$. However, diffraction pattern (B) which was measured 2 hours later shows only peaks from the parent sample. The deuteride peaks disappeared in the pattern (B) because of rapid desorption of deuterium.

$ZrCo_{1.5}Cr_{0.5}$ has cubic structure as two previous samples. After exposure to deuterium, the peak positions (Fig. 6.13) shifted toward low angle side like in the deuterides of $ZrCo_2$ and $ZrCo_{1.8}Cr_{0.2}$. In contrast to two former samples intensity of peaks of deuteride are much stronger than those of the parent sample. These small peaks at $2\theta = 36.1^{\circ}$, $42.6^{\circ}$ and $43.3^{\circ}$ correspond to the parent sample which partly did not form the deuteride phase. However, the partial decomposition of deuteride is also not excluded.

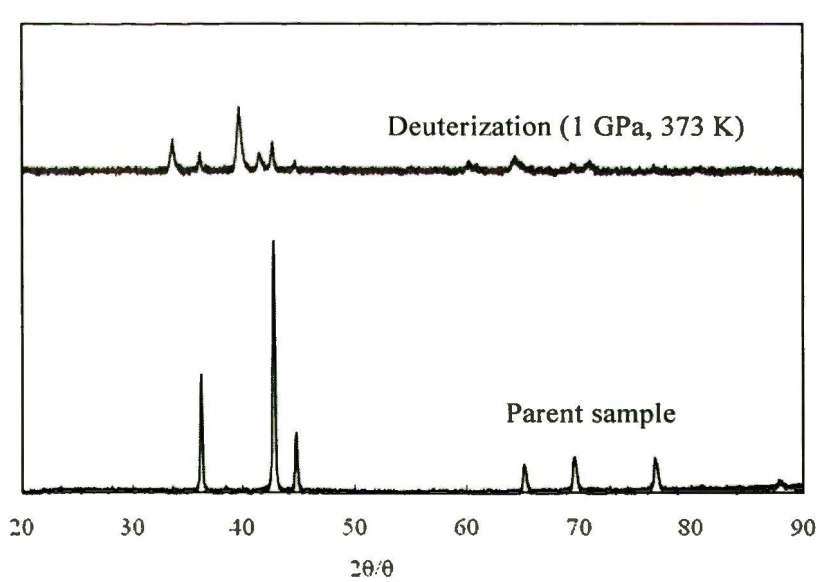


**Fig. 6.13. XRD patterns of $ZrCo_{1.5}Cr_{0.5}$ before and after deuterization.**

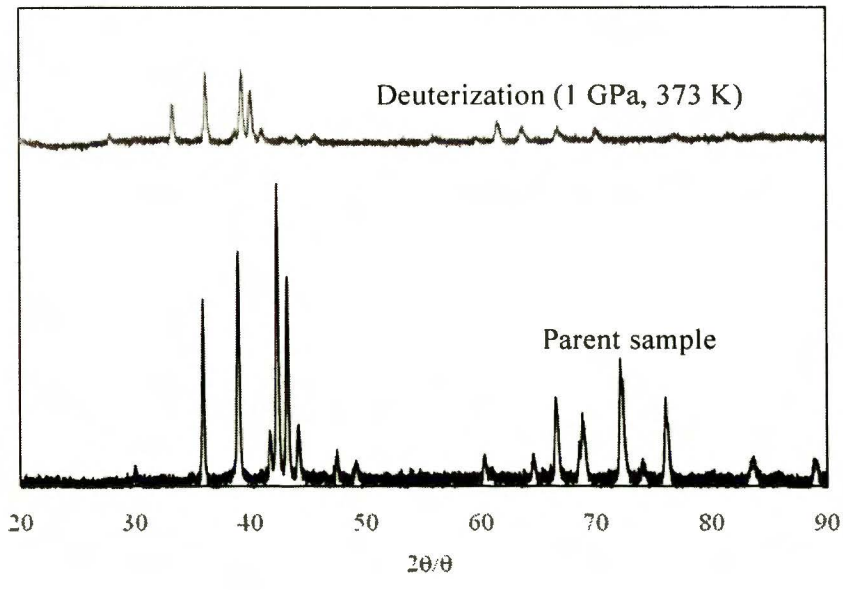


**Fig. 6.14. XRD patterns of ZrCoCr and its hydride.**

The crystal structure of ZrCrCo was hexagonal, thus different from previous three samples which were cubic. After deuterization, the peak positions of the deuteride shifted toward low angle side without any phase transition (Fig. 6.14). In the diffraction pattern of this deuteride, there are no peaks of parent phase what confirm that stability of ZrCrCo deuteride is higher than that of previous three deuterides.

The parent $ZrCo_{0.5}Cr_{1.5}$ has also hexagonal structure as ZrCoCr. As shown in Fig. 6.15, the peaks for the deuteride were broadened and split by deuterization whereas the pattern of ZrCoCr hydride exhibited sharp peaks. Taking into account coexistence of two hexagonal deuterides with slightly different deuterium concentration, we calculated separately their lattice parameters.

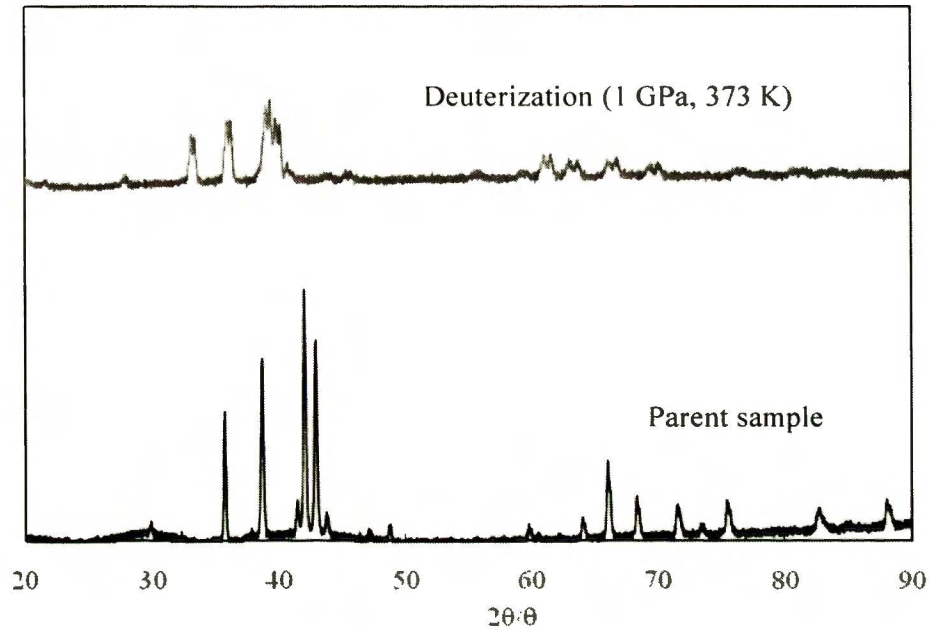


**Fig. 6.15. XRD patterns of $ZrCo_{0.5}Cr_{1.5}$ before and after deuterization.**

Fig.6.16 shows the peak patterns of parent $ZrCo_{0.2}Cr_{1.8}$ and its deuteride. The parent sample showed cubic structure again. The peak positions of the deuteride appeared at lower angle side corresponding to the expansion of the lattice without change of crystal symmetry. Let us remark that sample in which at least half amount of cobalt was substituted by chromium are stable at normal conditions. Therefore after deuterium treatment we can receive stable single deuteride phase for $ZrCoCrD_x$, $ZrCo_{0.2}Cr_{1.8}D_x$ and $ZrCr_2D_x$ (Fig. 6.17). In the case of $ZrCo_{0.5}Cr_{1.5}$ we got two-phase product but both are deuterides. Peaks of the parent sample were not present on the pattern.

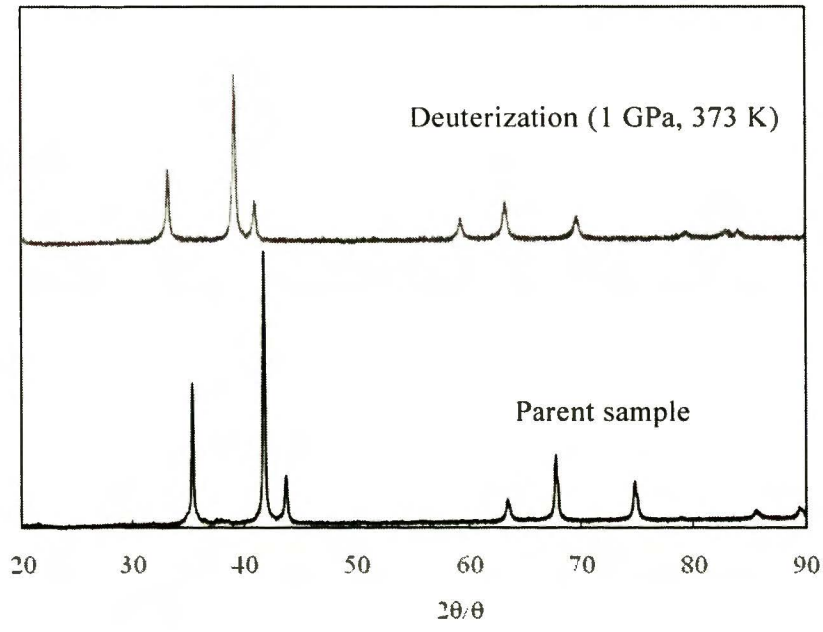


**Fig. 6.6. XRD patterns of $ZrCo_{0.2}Cr_{1.8}$ before and after deuterization.**

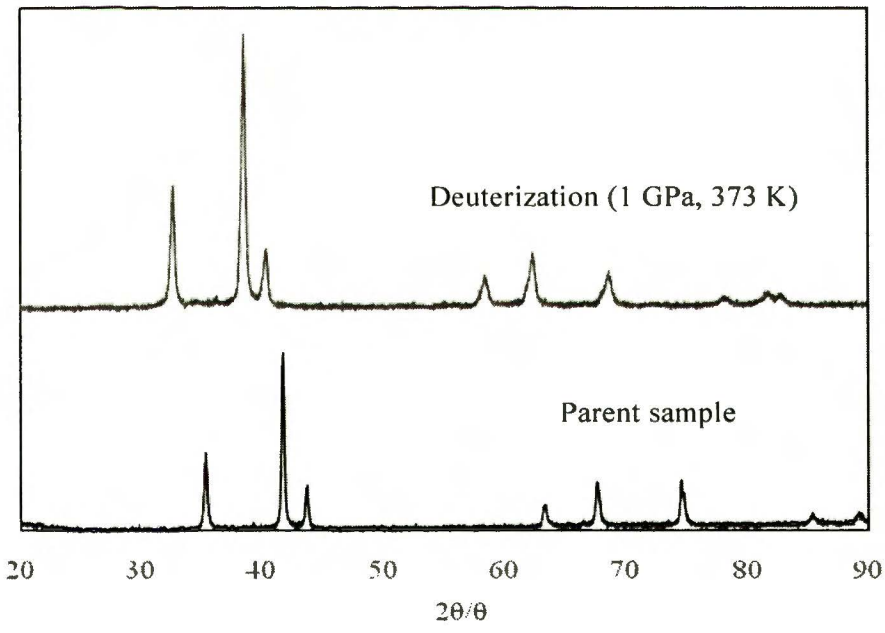


**Fig. 6.17. XRD patterns of $ZrCr_2$ before and after deuterization.**

Table 6.1 shows crystallographic parameters of $Zr(Co_{1-x}Cr_x)_2$ compounds and their deuterides. Most parent compounds have cubic structure except ZrCoCr and $ZrCo_{0.5}Cr_{1.5}$ which have hexagonal symmetry. This tendency of the structure change corresponds to results of Shaltiel et. al. [26]. Volume expansion resulted from deuterium absorption increases with increasing chromium concentration. The higher expansion of molecular volume corresponds to higher deuterium uptake. This is also in agreement with general tendency that hydrogen absorption increases with increasing lattice parameter of the parent phase. Concluding, increasing chromium concentration stimulates deuterium absorption and stability of deuterides in Zr-Co-Cr system.

**Table 6.1. Crystallographic data of $Zr(Co_{1-x}Cr_x)_2$ compounds and their deuterides**

| Samples | | Lattice Parameter (nm) | | Unit cell volume | Volume expansion |
|---|---|---|---|---|---|
| | | *a* | *c* | ($nm^3$) | (%) |
| $ZrCo_2$ | Parent | 0.695 | - | 0.336 | - |
| | Deuteride | 0.720 | - | 0.373 | 11.2 |
| $ZrCr_{0.2}Co_{1.8}$ | Parent | 0.698 | - | 0.340 | - |
| | Deuteride | 0.727 | - | 0.385 | 13.1 |
| $ZrCr_{0.5}Co_{1.5}$ | Parent | 0.705 | - | 0.350 | - |
| | Deuteride | 0.751 | - | 0.424 | 21.2 |
| ZrCrCo | Parent | 0.501 | 0.821 | 0.178 | - |
| | Deuteride | 0.537 | 0.881 | 0.220 | 23.1 |
| $ZrCr_{1.5}Co_{0.5}$ | Parent | 0.505 | 0.828 | 0.183 | - |
| | Deuteride Left | 0.541 | 0.885 | 0.225 | 23.0 |
| | Deuteride Right | 0.542 | 0.887 | 0.226 | 23.5 |
| $ZrCr_{1.8}Co_{0.2}$ | Parent | 0.719 | - | 0.372 | - |
| | Deuteride | 0.766 | - | 0.449 | 21 |
| $ZrCr_2$ | Parent | 0.720 | - | 0.373 | - |
| | Deuteride | 0.772 | - | 0.461 | 23.6 |

### 6.1.3. *$Zr(Co_{1-x}Fe_x)_2$ Deuterides*

In chapter 6.1.1, the resulted *p-C* isotherms of $ZrCo_2$ and $ZrFe_2$ have shown that hydrogen equilibrium pressure of $ZrCo_2$ is higher than that of $ZrFe_2$. The $ZrCo_2D_2$ is unstable at normal conditions and decomposes into $ZrCo_2$ within a few hours whereas $ZrFe_2D_{3.5}$ can be maintained for a long time. We observed sometimes self ignition of $ZrFe_2D_{3.5}$ samples when they contacted with air. This effect was never observed for $ZrCo_2H_2$ hydrides. This can be explained by the presence of very fine Fe particles at the surface which act as catalysts for oxidation.

In order to understand better the roles played by iron and cobalt in the hydrogenation properties of these Zr based Laves phases compounds, we studied the hydrogenation of pseudo-binary $ZrCo_{1.5}Fe_{0.5}$ and $ZrCo_{0.2}Fe_{1.8}$ compounds. $ZrCo_{2-x}Fe_x$ pseudobinary alloys have cubic C15 structure for whole composition range. Their lattice parameter increases with increasing Fe content. The XRD patterns of the corresponding deuterides indicate that the C15 structure is maintained with an increase of the cell parameter for both $ZrCo_{0.2}Fe_{1.8}$ and $ZrCo_{1.5}Fe_{0.5}$. In table 6.2, the cell parameters of the $ZrCo_{1.5}Fe_{0.5}D_{2.7}$ and $ZrCo_{0.2}Fe_{1.8}D_{3.3}$ deuterides compared with those of $ZrCo_2$ and $ZrFe_2$ deuterides. The relative cell volume $\Delta V/V$ increases progressively from 11.7 to 23.1 % upon Fe for Co substitution. Assuming a cell volume increase of 0.0027 $nm^3$/D atom, it is possible to estimate the average D content in the deuterides. Its progressive increase from 1.8 to 3.8 D/f.u. versus the Fe content indicates that Fe favors the D(H) solubility in the $Zr(Co_{1-x}Fe_x)_2$ compounds. This effect can be also related to increasing interatomic distance in the parent compounds.

**Table 6.2. Cell parameters of $Zr(Co_{1-x}Fe_x)_2$ intermetallic compounds and corresponding deuterides. The D content is estimated assuming cell volume increase of 0.0027 $nm^3$/D atom**

| Composition | Intermetallic | Deuteride | $\Delta V$ ($nm^3$) | $\Delta V/V$ (%) | D / f.u. |
|---|---|---|---|---|---|
| $x_{Fe}$ | $a$ (nm) | $a$ (nm) | | | |
| 0 | 0.696 | 0.722 | 0.0393 | 11.7 | 1.82 |
| 0.25 | 0.699 | 0.737 | 0.0587 | 17.2 | 2.72 |
| 0.9 | 0.707 | 0.752 | 0.0725 | 20.5 | 3.36 |
| 1 | 0.798 | 0.758 | 0.0817 | 23.1 | 3.78 |

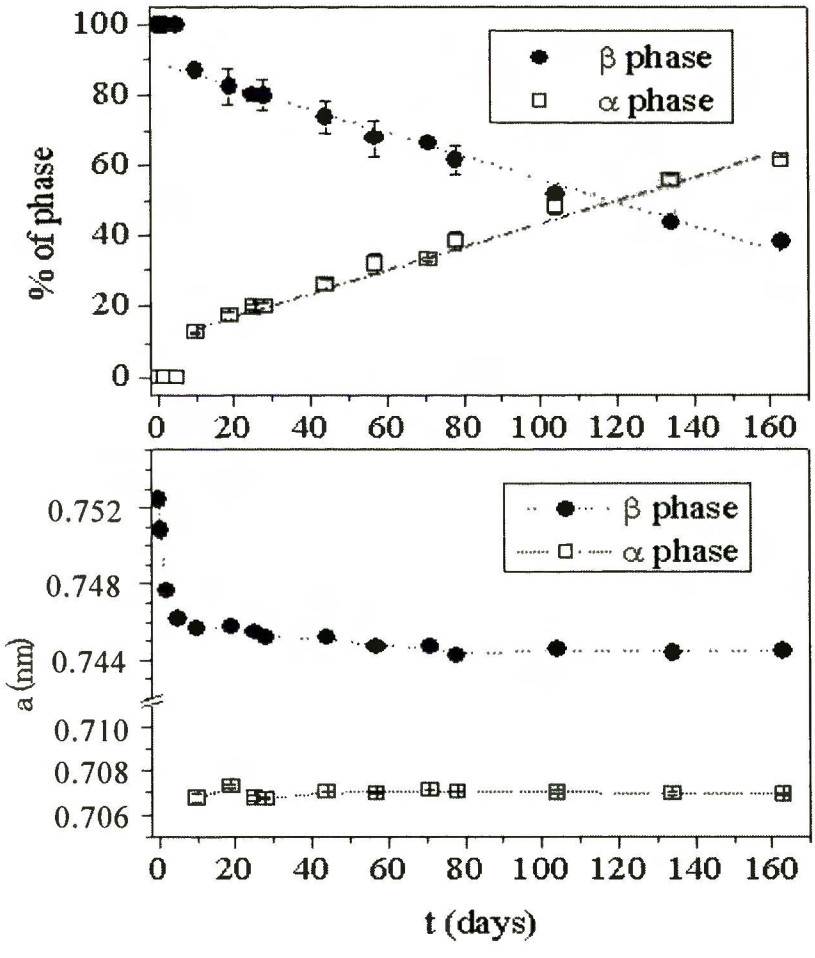


**Fig. 6.18. Evolution of phase percentage (%) and cell parameters of α and β phase in $ZrCo_{0.2}Fe_{1.8}D_x$ versus aging time at normal conditions.**

In order to observe the kinetics of decomposition of the $Zr(Co_{1-x}Fe_x)_2$ deuterides at normal conditions, XRD measurements have been performed as a function of time. During first 10 days $ZrCo_{0.2}Fe_{1.8}D_x$ (Fig. 6.18) remains as a single phase with a decrease of the cell parameter revealing a deuterium desorption from the deuteride β phase. Then a precipitation of the cubic α phase is observed. After these 10 days, the cell parameters of both α and β phase vary only slightly versus the aging time. The percentage (%) of the β phase decreases almost linearly versus time, indicating a regular phase transformation into the α phase due to deuterium desorption. After 4 months, about half of the β phase has been decomposed. Moreover, we observed the decomposition process of the $ZrCo_{0.2}Fe_{1.8}D_x$ after the deuterization at 1 GPa and 373 K. As shown in Fig. 6.19, the peak intensities of deuteride phase decreased and that of parent phase increased gradually within several months. However the deuteride phase remained yet after 5 months of the decomposition process at 298 K. Therefore, it can be roughly estimated that the full deuterium desorption process will be completed within 8-9 months. $ZrCo_{1.5}Fe_{0.5}D_x$ decomposes much faster, as after only one day 1/3 of the β phase has already been transformed into the α phase, and after two weeks it decomposed completely. In the case of $ZrCo_2$ the full decomposition occurred within a few hours. This difference of kinetics of D desorption shows that the Fe for Co substitution not only increases the deuterium solubility, but also strongly improves the stability of the deuteride.

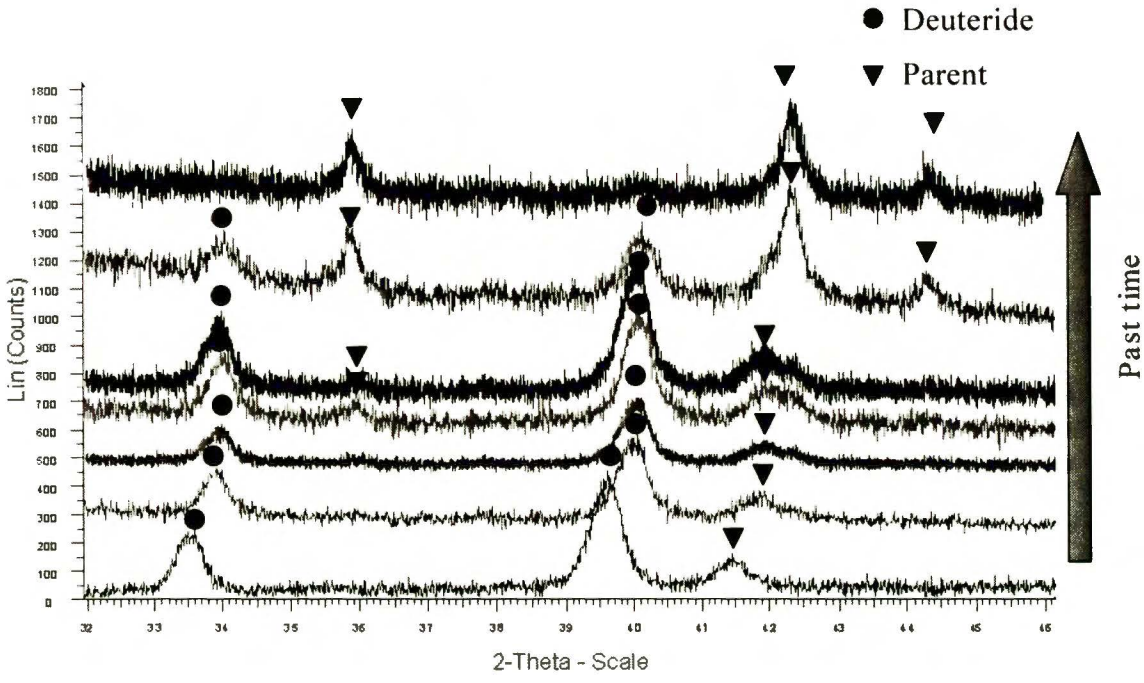


**Fig. 6.19. The decomposition process of $ZrCo_{0.2}Fe_{1.8}D_x$.**

## 6.1.4. *$Zr_xTi_{1-x}Co_2 - H_2$ System*

Titanium compounds such as TiFe, TiCo and TiNi of CsCl-type structure are well known as good hydrogen absorbers. However, $TiFe_2$ and $TiCo_2$ are supposed to be non-hydride forming alloys just like $ZrCo_2$ and $ZrFe_2$ before their treatment up to 1 GPa ($H_2$) range [27,28]. For this reason, there are few reports relative to hydrogen dissolution in these compounds.

Both $ZrCo_2$ and $TiCo_2$ have $Cu_2Mg$-type cubic structure with C15 Laves phase (Fig. 6.20 or Fig. 3.1). The interstitial sites in the compounds are tetrahedral sites that are formed by Zr or Ti and Co atoms. Although Laves phase compounds are typical size factor compounds, the stability of the structures is also closely related to the electron concentration, implying that the crystal structures are strongly governed by the valence state of the constituent atoms [65]. Taking into account that interatomic

distance in $TiCo_2$ is smaller than that of $ZrCo_2$ one can expect that hypothetical $TiCo_2H_x$ hydride would be less stable and should have higher formation pressure than $ZoCo_2H_x$.

The $(Ti_{1-x}Zr_x)Co_2$ alloys with x = 0.10, 0.50, 0.75, and 0.90 were prepared in argon atmosphere by an arc-melting method using a non-consumable tungsten electrode and a water-cooled copper tray. Zirconium (purity of 99.95%), titanium (purity of 99.95%) and cobalt (purity of 99.95%) were used as starting materials. The alloys were re-melted three times to ensure their good homogeneity. The melted buttons were sealed in evacuated quartz tubes for further homogenization annealing at 1123 K for 7 days, then were cooled down and crushed to small pieces. High pressure hydrogen treatment at 1.0 GPa ($H_2$) has been performed in the piston-cylinder apparatus described in Chap. 5.3. Temperature range was from 298 K to 373 K. After hydrogen treatment, the high pressure apparatus was cooled down to 263 K, samples were taken out and put in liquid nitrogen to prevent hydrogen desorption.

The phase identification of the prepared samples was carried out by powder X-ray diffractometry (XRD) using a PANalytical X'Pert PRO diffractometer. For parent alloys the diffraction intensity was measured from 20° to 80° with a step of 0.02° and a counting time of 10 second per step. For hydrides it was measured from 41° to 45° with a step of 0.05° and a counting time of 10 second per step. Magnetic hysteresis of $(Ti_{1-x}Zr_x)Co_2$ ($0 < x < 1$) alloys and hydride were measured using superconducting quantum interference device (SQUID) magnetometer (Quantum Design, MPMS-XL7) under an applied magnetic field within the range of 40000 to −40000 Oe at 300 K [66].

$Zr_xTi_{1-x}Co_2$ ($x = 0.1 \sim 0.9$) alloys did not show crystal structure changes in whole composition range. Fig. 6.21 shows XRD pattern of the parent samples. The peak patterns were maintained for all compounds but the positions of peaks shifted to high angle side with increasing Ti content, what means that the substitution of Zr by Ti in the $(Ti_{1-x}Zr_x)Co_2$ alloys leads to decrease of the lattice parameter.

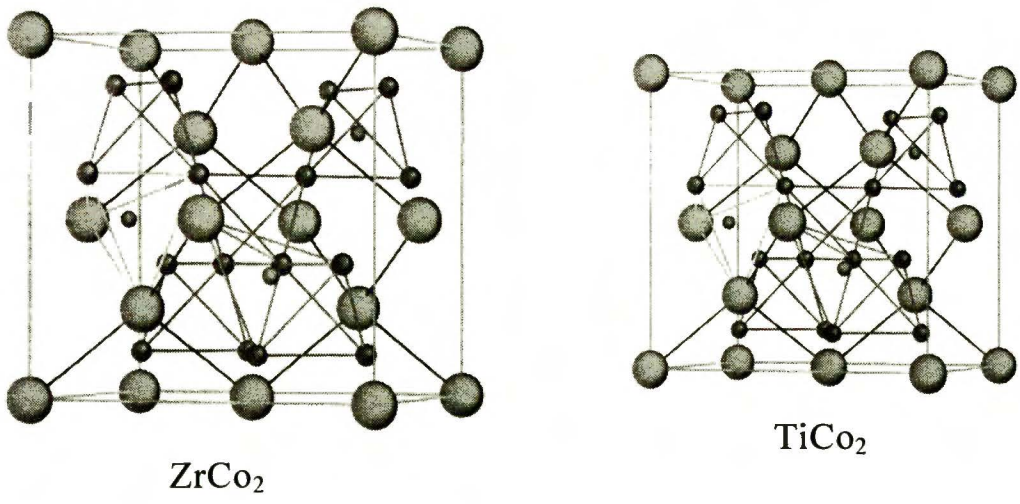


**Fig. 6.20. Schematic representations of $ZrCo_2$ and $TiCo_2$.**

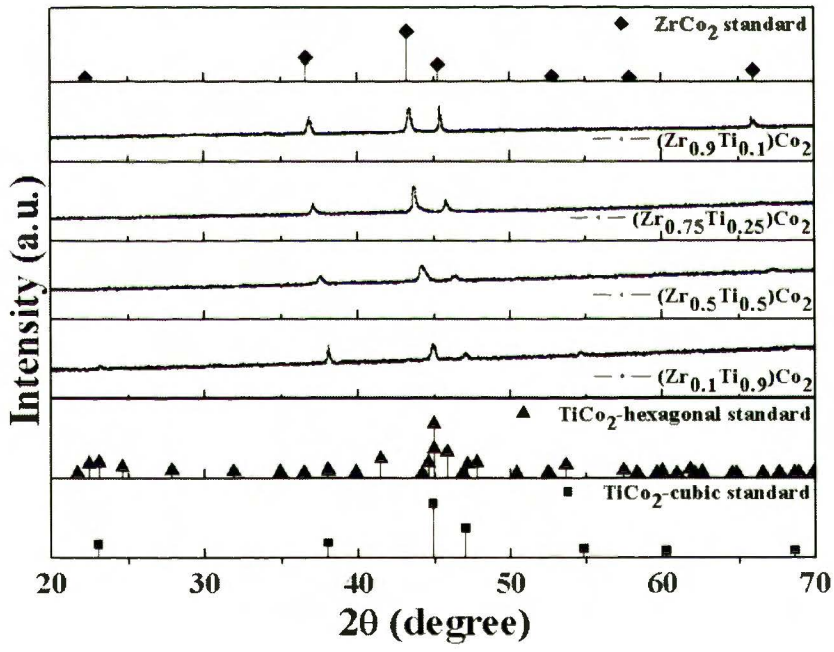


**Fig. 6.21. XRD patterns of $Zr_xTi_{1-x}Co_2$ parent samples.**

Fig. 6.22 shows XRD patterns of $Zr_xTi_{1-x}Co_2$ hydrogenated at 0.5 GPa and 1 GPa. The analyses were carried out for short scanning time and narrow range of diffraction angles ($2\theta = 44^\circ \sim 45^\circ$) considering the hydrogen desorption rates of the

compounds are very high. After treatment at 0.5 GPa ($H_2$) hydrides were formed only in $Zr_{0.9}Ti_{0.1}Co_2$ and $Zr_{0.75}Ti_{0.25}Co_2$. When pressure of synthesis was 1 GPa ($H_2$) the hydride phase appeared also in $Zr_{0.5}Ti_{0.5}Co_2$ alloy. From these results it is clear that with increasing Ti concentration in the parent alloy the hydride formation pressure increases and hydride, if formed, has smaller stability. For this reason a special care is necessary for sample handling and a very fast XRD measurement device is also needed.

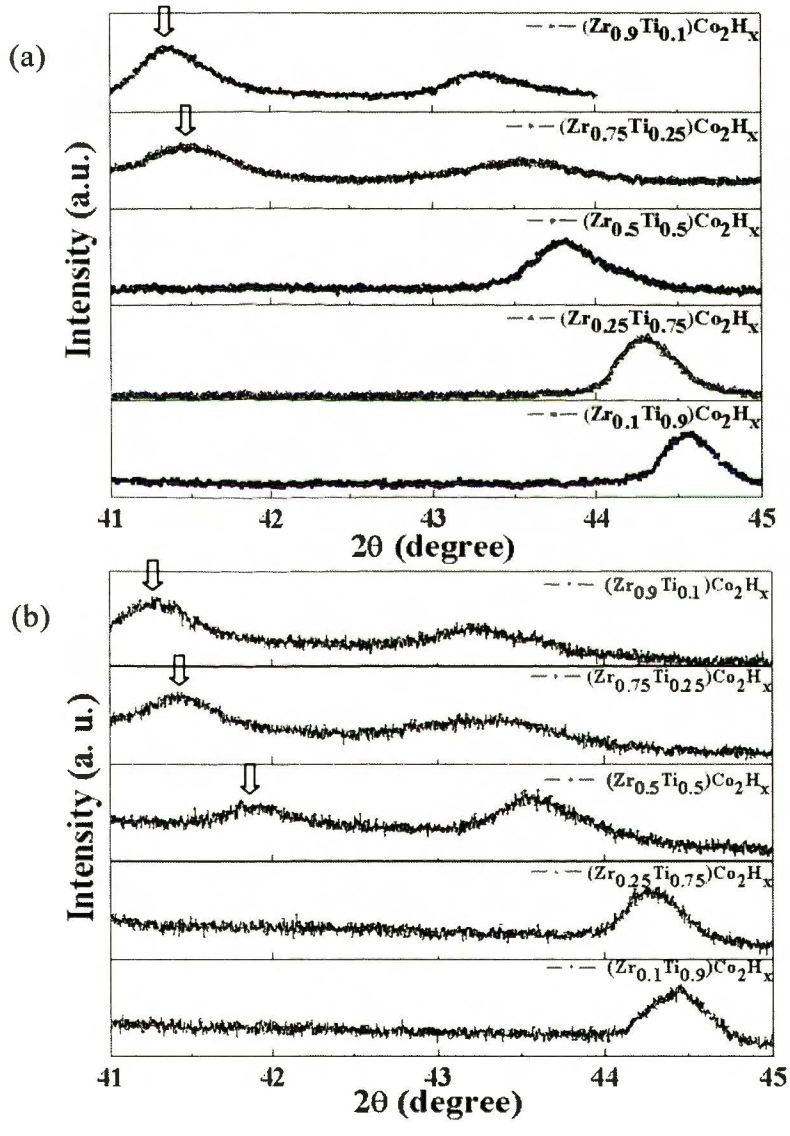


**Fig. 6.22. XRD patterns of $Zr_xTi_{1-x}Co_2$ hydrides; the samples hydrogenated at (a) 0.5 GPa and (b) 1 GPa. Arrows show hydride peaks.**

In order to understand the effect of Zr substitution on dehydriding kinetics, desorption rates (the XRD peaks ratio of hydride/parent alloy) were measured as shown in Fig. 6.23. This shows the in-situ XRD patterns for discharging process of $(Ti_{0.1}Zr_{0.9})Co_2$ hydride. There are three sets of hydride/parent alloy peaks ratios labeled as I, II, and III. The positions of XRD peak for hydride are labeled as dot line; parent alloy is dash line. The variation for each set of hydride/parent alloy can be clearly identified. During the discharging process, the XRD signal of hydride is decreasing and that of the parent alloy is increasing simultaneously.

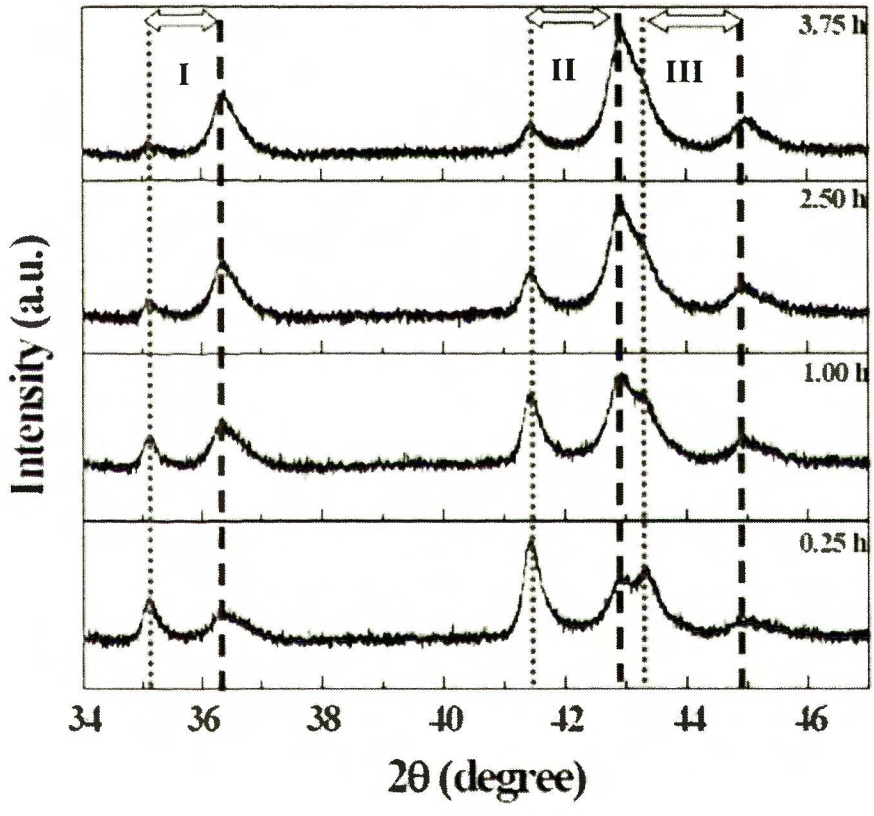


**Fig. 6.23. *in-situ* XRD patterns of discharging process for $Ti_{0.1}Zr_{0.9}Co_2$ hydride during exposure to ambient conditions. There are three sets of hydride/parent alloy peaks labeled as I, II, and III. The dot lines are for hydride and the dash are for parent alloy.**

Hydrogen atoms present in the interstitial sites, expand the lattice volume increasing the Co–Co distance to a considerable extent which ultimately results in changes of magnetic properties. In Fig. 6.24 (a), it can be seen that the hydride formation of $(Ti_{0.10}Zr_{0.90})Co_{2.00}$ alloy causes the reduction of magnetic susceptibility. The volume effect should increase the magnetization due to enhanced localization of the 3*d* orbitals of Co. However for hydride the role of hydrogen becomes dominant over the volume expansion effect resulting in the decrease of magnetic moment. Fig. 6.24 (b) is the *in-situ* SQUID measurement of magnetization during the desorption process of $(Ti_{0.10}Zr_{0.90})Co_{2.00}$. Hydride and α-solid solution coexisted during the desorption process, the hydrogen released from the hydride causing the increase of the amount of parent alloy. The magnetic susceptibility therefore increased and shifted back to the value of the parent alloy. This result also means that the hydrogen absorption in these alloys is a reversible process [66].

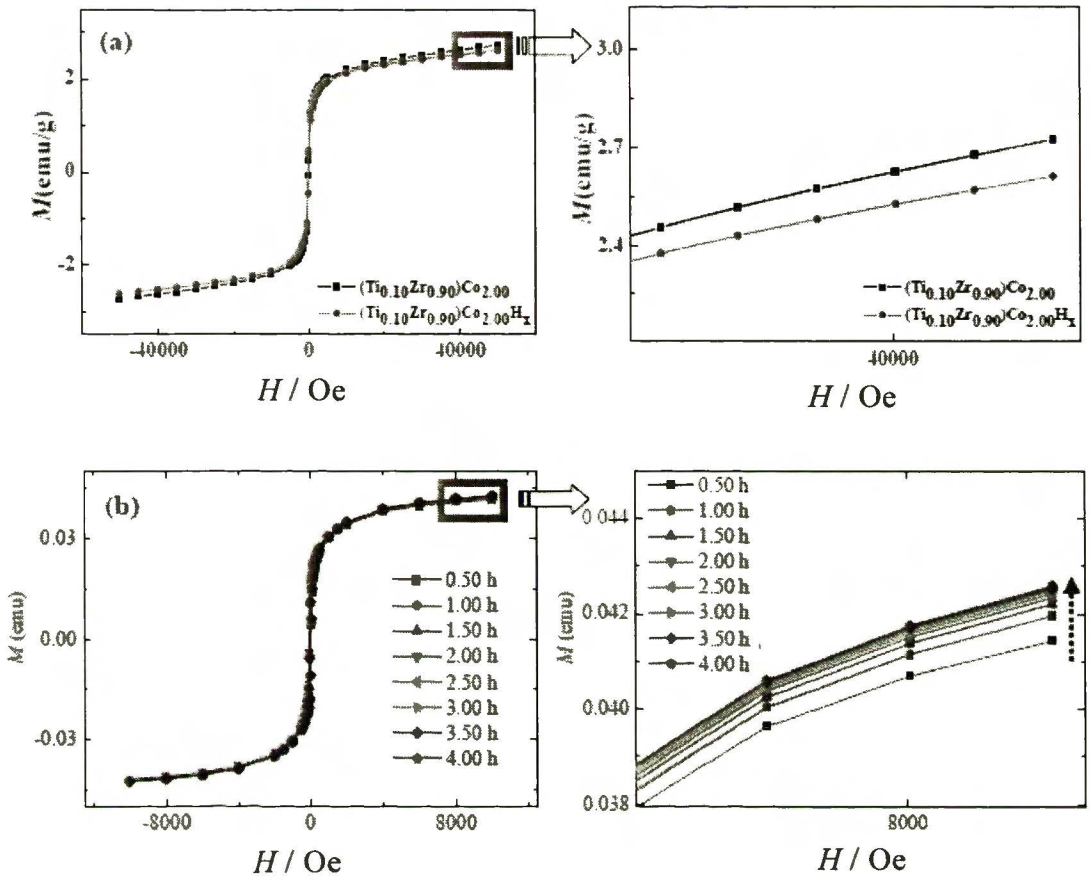


**Fig. 6.24. (a) Magnetization v.s. applied magnetic field curves of $(Ti_{0.10}Zr_{0.90})Co_{2.00}$ alloy and hydride samples at 5 K, (b) in-situ magnetization v.s. applied magnetic field curve of $(Ti_{0.10}Zr_{0.90})Co_{2.00}$ hydride at 300 K.**

## *6.2. Yttrium or Rare Earth based Alloys*

As shown in Chap. 6.1.1 and 6.1.2, $ZrCo_2$- and $ZrFe_2$-based pseudobinary alloys can form hydrides directly from the parent phase and hydrogen in a first order chemical reaction followed with discontinuous increase of the lattice parameter. A salient feature of these systems is that they can form only one β-hydride and during its formation space group does not change. However, hydrogen concentration range in this β-hydride can be quite large.

More complicated are $RFe_2H_2$ (R = Y or rare earths) systems in which several hydrides with different hydrogen concentration and different space groups can exist in various intervals of hydrogen pressure.

A lowering of the crystal symmetry with a change of the space group was observed in C15 cubic $YFe_2$ and $ErFe_2$ [29]. The structure changes occurred at low pressures and for both compounds hydrides up to about 4 H/f.u. [67] were reported. Then Raj et. al. [68] found that increasing pressure to 5 MPa resulted in appearance of orthorhombic phase $ErFe_2H_5$ coexisting with cubic $ErFe_2H_4$. Soon later the single orthorhombic $YFe_2H_5$ and $ErFe_2H_5$ were synthesized [29].

The next goal of this study was therefore to prove possible existence of the orthorhombic $RFe_2H_5$ (R = Gd, Tb, Dy and Ho) phases analogous to $ErFe_2H_5$ and $YFe_2H_5$.

Moreover, we investigated more about the very unusual $RMn_2H_6$ hydrides. From our experience these hydrides form for several $RMn_2$, R being a heavy rare earth. As shown in Chap. 3.1.3, the 8c sites of Fm□m lattice of $YMn_2H_6$ hydride are occupied statistically by Y and Mn atoms. It was therefore interesting to learn whether in these 8c positions is possible (or not) to substitute Y by a rare earths (like Dy) or by Mn. In order to answer this question we extended experiments for pseudobinary $(Y_xDy_{1-x})Mn_2$ alloys and for Y-Mn alloys containing more Mn in their chemical formula ($Y_6Mn_{23}$ and $YMn_{12}$). Finally, we applied high hydrogen pressure technique for exploration of $R_7Rh_3$ which will be described in separate chapters.

All samples were prepared by arc-melting of high purity metals. To ensure homogeneity the samples were re-melted several times and annealed in inert atmosphere for two weeks. Then bulk alloys were crushed to fine powder and their

crystal structures were checked by XRD. The XRD patterns were measured by a D8 Brucker diffractometer equipped with a rear graphite monochrometer using CuKα radiation. XRD patterns were refined with the Rietveld method, using the FullProf code. The line shapes were refined with a Pearson VII function.

### 6.2.1. *$RFe_2H_5$ Hydrides*

It has been evidenced that orthorhombic $RFe_2H_5$ with R = Y and Er can be stabilized under high hydrogen or deuterium pressure [29]. Purpose of this study was therefore to investigate whether this orthorhombic phase can be also formed for $RFe_2$ compounds with R = Gd, Tb, Ho and Dy. Samples of these compounds have been submitted for several days to deuterium pressure of 1 GPa at 373 K. The XRD patterns are presented in Fig. 6.25 and their refinements in Table 6.3. The previous results for R = Y, Er [2] have been added for comparison. For R = Gd, Tb the above mentioned conditions lead to the formation of only C15 cubic hydride, with a relative cell volume increase of 28.1 %. For R = Dy and Ho, a mixture of orthorhombic and cubic phase was obtained. It is noticeable that the amount of orthorhombic phase increases with the atomic number of the rare earth. This probably means that the orthorhombic distortion is favored by the smaller radius of the rare earth. The cell volume enlargement is slightly larger for the orthorhombic phase than for the cubic phase of the same material. But this change remains small, what means that the hydrogen content should be very close in both cubic and orthorhombic phases. In previous work [29], it was observed that $ErFe_2H_5$ undergoes at 390 K a transition which was interpreted as a structural change from orthorhombic to cubic phase due to order-disorder transition of deuterium in the lattice. It is possible that the cubic and orthorhombic structures have close enthalpy of formation and that the orthorhombic structure become more stable for a smaller rare earth radius. For $YFe_2H_5$, 100 % of the orthorhombic structure was obtained, although the equivalent cell volume of the cubic $YFe_2H_5$ hydride ($V_{cubic} = 2 \times V_{orthorhombic} = 0.514$ nm$^3$) is intermediate between those of $GdFe_2D_5$ and $TbFe_2D_5$. This means that although the Y intermetallic compounds have often a close structural behavior to the corresponding heavy rare earth compounds,

some differences may occur in the hydride or deuterides phase stabilities.

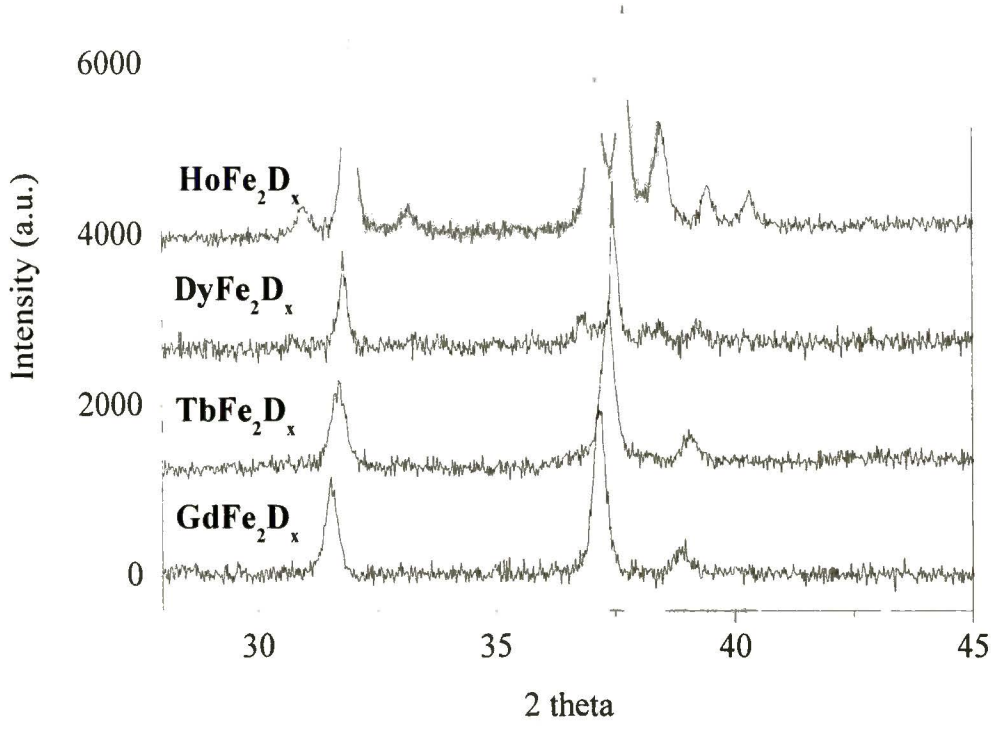


**Fig. 6.25. XRD patterns of the $RFe_2D_x$ compounds.**

**Table 6.3. Cell parameters of $RFe_2D_x$ phases.**

| Compound | Orthorhombic phase | | | | C15 cubic phase | | | |
|---|---|---|---|---|---|---|---|---|
| | Phase (%) | *a* (nm)<br>*b* (nm)<br>*c* (nm) | *V* (nm$^3$) | $\Delta V/V$ (%) | Phase (%) | *a* (nm) | *V* (nm$^3$) | $\Delta V/V$ (%) |
| $GdFe_2D_x$ | | | | | 100 | 0.803 | 0.518 | 28.6 |
| $TbFe_2D_x$ | | | | | 100 | 0.800 | 0.512 | 29.1 |
| $DyFe_2D_x$ | 48.7 | 0.539<br>0.581<br>0.802 | 0.251 | 28.3 | 51.3 | 0.795 | 0.502 | 28.0 |
| $HoFe_2D_x$ | 69.6 | 0.542<br>0.579<br>0.801 | 0.251 | 28.9 | 30.4 | 0.793 | 0.498 | 28.0 |
| *$ErFe_2D_x$ | 92.0 | 0.542<br>0.579<br>0.801 | 0.252 | 30.6 | 8.0 | 0.790 | 0.493 | 27.8 |
| *$YFe_2D_x$ | 100 | 0.544<br>0.585<br>0.808 | 0.257 | 28.9 | | | | |

*Data from Ref. [2]

## 6.2.2. *$Y_{1-x}Dy_xMn_2H_6$ Pseudobinary Hydrides*

So far, it was reported that the $RMn_2$ compounds with R = Y, Gd, Dy, Ho and Er can form hydrides or deuterides with 6 H(D)/f.u. [5,3,69,70]. These phases crystallize with a different cubic structure than their parent $RMn_2$ compounds. These compounds are isostructural to complex metal hydride like $Mg_2FeH_6$ with $K_2PtCl_6$ type structure [39], but here the Mg site is replaced by a disordered substitution of R and Mn atoms.

This means a complete structural reorganization of parent $RMn_2$ alloys upon H absorption. It was interesting to learn whether similar reorganization can occur in pseudobinary alloys in which Y was substituted by a rare earth like Dy.

$Y_{1-x}Dy_xMn_2$ compounds with x = 0.1, 0.25, 0.75 and 0.9 were exposed during 14 days to 1 GPa of hydrogen at 373 K. Single cubic phases, isostructural to $YMn_2H_6$ and $DyMn_2H_6$ were obtained. Their cell parameters and cell volumes are reported and compared to their parent compound values in Table 6.4. The Y for Dy substitution leads to an increase of the cell parameters of the intermetallic compound whereas a slight decrease of the cell parameter is observed upon Y for Dy substitution in the hydrides. This shows that in the $RMn_2H_6$ phase the cell parameter is not very sensitive to the size of the R element. These results indicate that the structural stability of the $RMn_2D_6$ phase does not depend on the nature of the rare earth element for R = Y and heavy rare earth. On the other hand, several trial to obtain this cubic phase for light rare earth with R = Nd and Pr were until now not successful.

**Table 6.4. Cell parameters of $Y_{1-x}Dy_xMn_2$ intermetallic and hydrides**

| Sample | Parent compound | | Hydride | |
|---|---|---|---|---|
| | *a* (nm) | *V* ($nm^3$) | *a* (nm) | *V* ($nm^3$) |
| $DyMn_2H_6$ | 0.7587 | 0.4367 | 0.6717 | 0.3031 |
| $Dy_{0.9}Y_{0.1}Mn_2H_6$ | 0.7586 | 0.4366 | 0.6711 | 0.3022 |
| $Dy_{0.75}Y_{0.25}Mn_2H_6$ | 0.7600 | 0.4389 | 0.6710 | 0.3021 |
| $Dy_{0.25}Y_{0.75}Mn_2H_6$ | 0.7631 | 0.4444 | 0.6709 | 0.3020 |
| $Dy_{0.1}Y_{0.9}Mn_2H_6$ | 0.7659 | 0.4493 | 0.6707 | 0.3017 |
| $YMn_2H_6$ | 0.7660 | 0.4495 | 0.6707 | 0.3017 |

### 6.2.3. $Y_6Mn_{23} - H_2$ and $YMn_{12} - H_2$ Systems

Hydrogenations of $Y_6Mn_{23}$ and $YMn_{12}$ have been carried out at 1 GPa hydrogen gas and 373 K for 5 days by using high pressure apparatus in our laboratory. The bulk samples were crushed with acetone to inhibit oxidation and their crystal structures were analyzed by XRD. Then the crushed samples were placed in the high pressure vessel which was evacuated for one night at 373 K. Hydrogen gas was introduced into the evacuated vessel gradually up to 0.2 MPa, and after this preliminary hydrogenation the pressure was increased to 1 GPa ($H_2$). After syntheses are finished, the XRD data of hydrides were measured and compared with those of parent samples.

Fig. 6.26 shows XRD patterns of the $Y_6Mn_{23}$ parent sample, and for the reference the peak positions of $Y_6Mn_{23}$ taken from PDFMaint JCP2. Lattice parameter of the parent $Y_6Mn_{23}$ sample is $a$ = 1.243 nm and its unit cell volume $V$ = 1.921 nm$^3$. These values are in good agreement with the reference data [43]. Small amount of $YMn_2$ was only contamination of the sample.

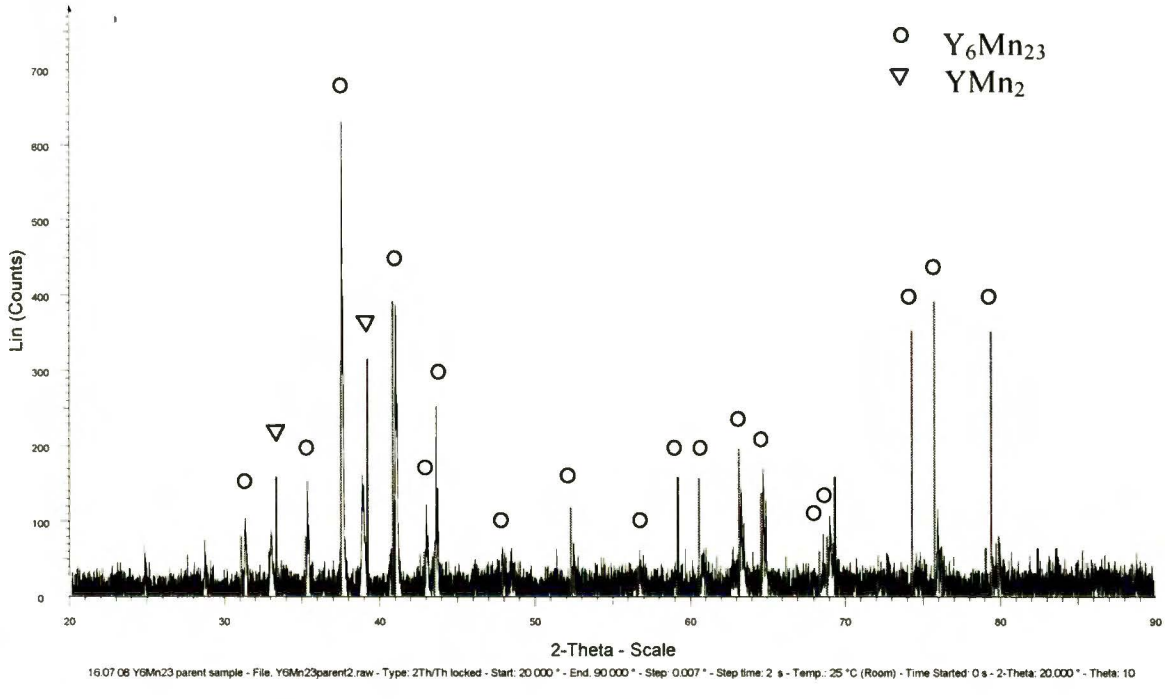


**Fig. 6.26. Peak pattern of $Y_6Mn_{23}$ parent sample.**

Fig. 6.27 shows peak patterns of $Y_6Mn_{23}$ parent sample and its hydride. The peak pattern of the hydride was changed drastically from that of the parent sample. The fitting program of crystal structure WinPlotR led to a space group *Fm□m* and $a$ = 0.669 nm for the hydride. K. Hardman-Rhyne et. al. [23] also deuterized the compound up to $Y_6Mn_{23}D_{23}$ and determined the crystal structure by using neutron diffraction at 4 K. They found that this structure is tetragonal with *P4/mmm* and lattice parameters $a$ = 0.903 nm and $c$ = 1.27 nm, therefore very different from our result. The crystal structure of our hydride differs also from $Y_6Mn_{23}H_{25}$ [41], since the XRD pattern and determined lattice parameter of hydride in our study are surprisingly almost the same as for $YMn_2H_6$ [5,38,71] (Fig. 3.3). This result strongly suggests that parent structure collapsed and transformed into $YMn_2H_6$-type structure in such way that four Mn atoms took 4a positions each being surrounded with 6 hydrogen atoms while remaining yttrium and Mn atoms were located statistically in available 8c sites. It means that our $Y_6Mn_{23}$ hydride exists in the form of $(Y_{18/29}Mn_{40/29})MnH_6$ in the $YMn_2H_6$-type structure.

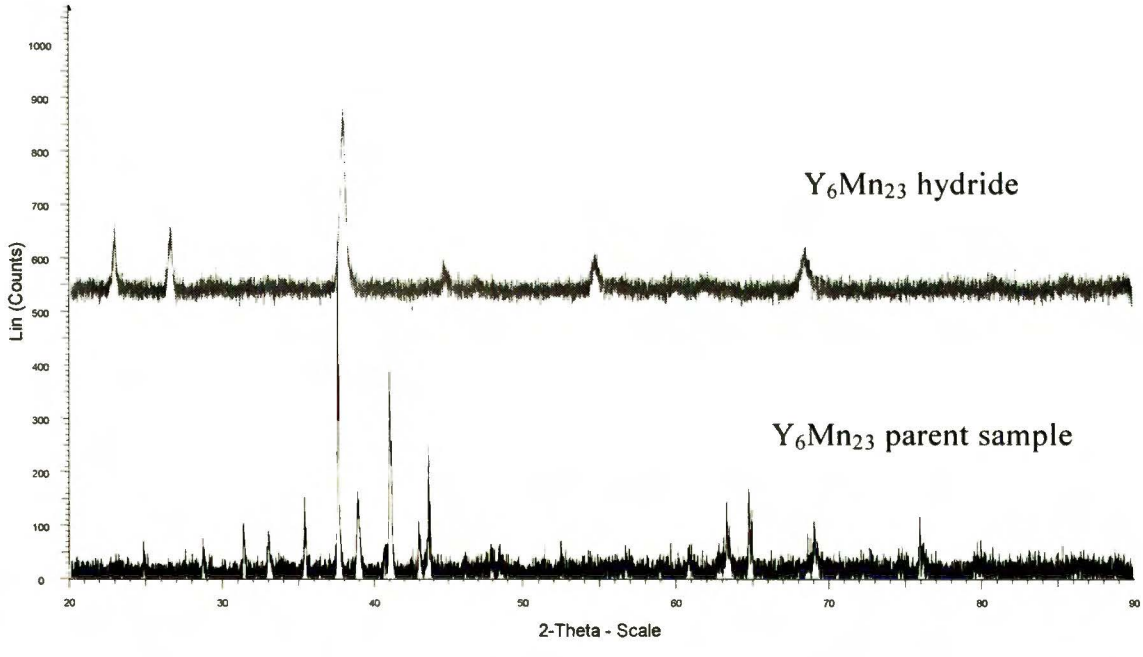


**Fig. 6.27. Peak patterns of $Y_6Mn_{23}$ and its hydride with $YMn_2H_6$-type structure.**

Crystal structure of $YMn_{12}$ parent sample was investigated by XRD (Fig. 6.28), and the result led to $ThMn_{12}$-type tetragonal structure (space group *I4/mmm*) with lattice parameters $a$ = 0.860 nm, $c$ = 0.479 nm and unit cell volume $V$ = 0.354 $nm^3$ in good agreement with the reference in JCP2. Fig.6.29 shows XRD peak patterns of $YMn_{12}$ parent sample and its hydride synthesized under high hydrogen pressure. The pattern of the hydride differed from that of parent sample, and it could be fit to cubic structure. From peaks at $2\theta$ = 23°, 26°, 38°, 55° and 69° it can be seen clearly, even though back-ground intensity is high, that the pattern of hydrogenated sample is the same as $Y_6Mn_{23}$ hydride synthesized under high $H_2$ pressure and $YMn_2H_6$. As the result of WinPlotR analysis, lattice parameter was $a$ = 0.669 nm identical with that of $YMn_2H_6$ as shown in Table 6.5. Let us remark that according to our knowledge the hydrides of $YMn_{12}$ were not yet reported, whereas the structure of $YFe_{11}Ti$ isostructural with $YMn_{12}$ maintains tetragonal structure up to $YFe_{11}TiH_{1.8}$ during the hydrogenation up to 1 MPa [44]. It means that we succeeded the first synthesis of $YMn_{12}$ hydride with high hydrogen concentration. Moreover the $YMn_{12}$ transformed into $(Y_{3/13}Mn_{23/13})MnH_6$ during high pressure hydrogen treatment.

This result is very interesting for the following reasons:

- It is first hydride found for the $YMn_{12}$ alloy
- It contains high hydrogen concentration 2H:M ratio
- It is formed through radical restructurization of the lattice and resulting hydride is of the $YMn_2H_6$-type. This confirms very unusual strong tendency of manganese to form very stable $(MnH_6)^{x-}$ anions network.

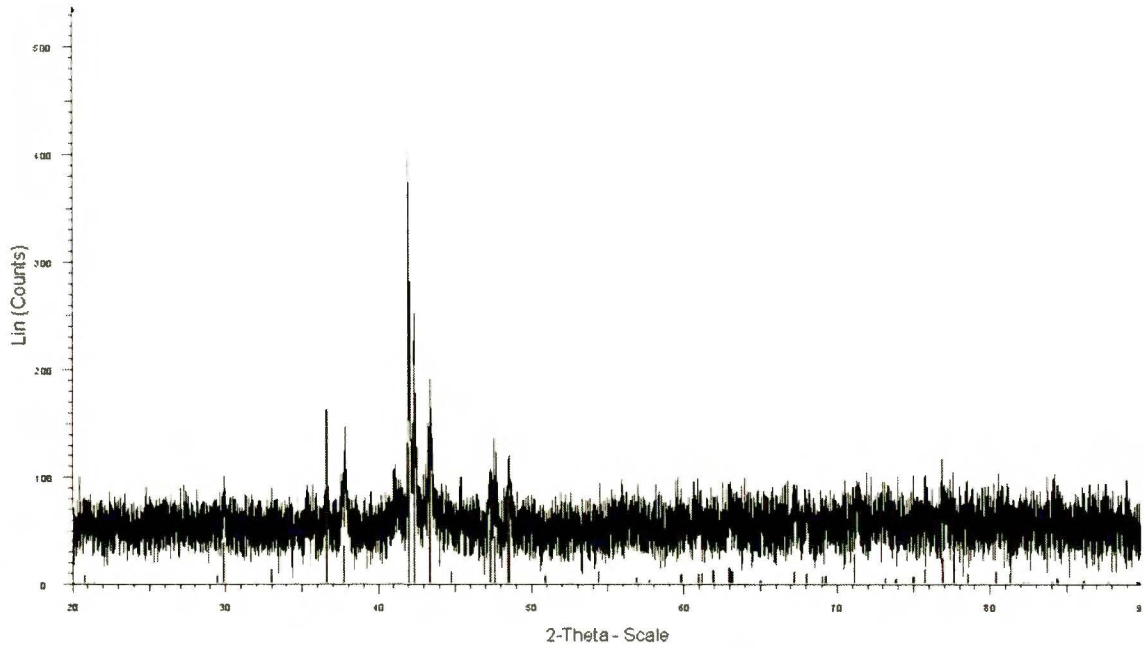


**Fig. 6.28. Peak pattern of $YMn_{12}$.**

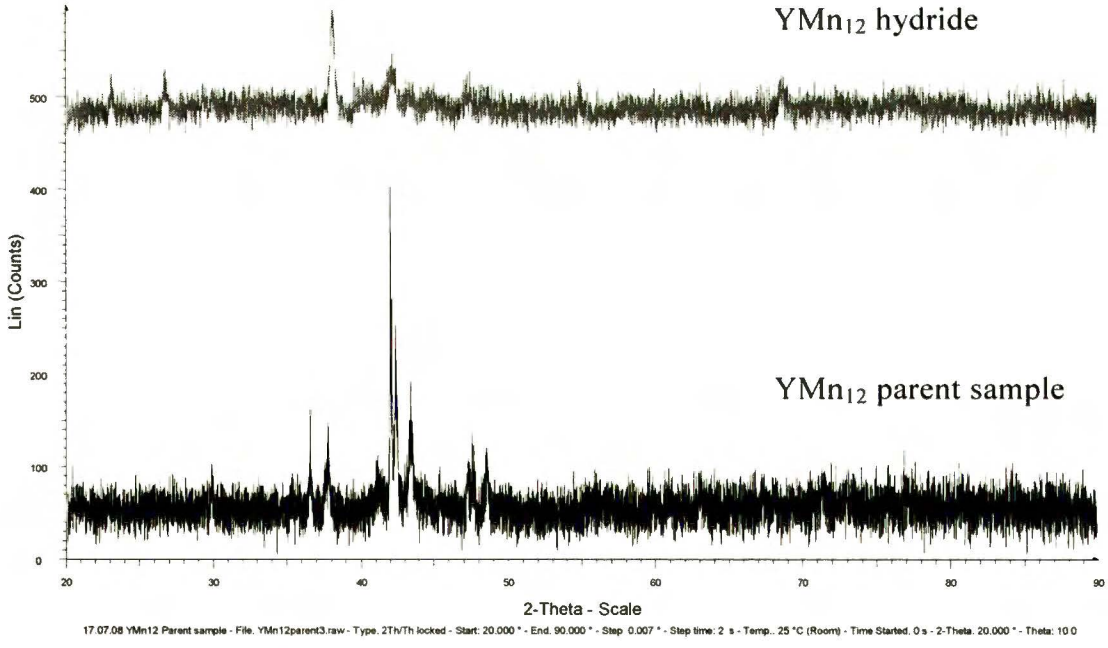


**Fig. 6.29. XRD pattern of $YMn_{12}$ and its hydride.**

$RMn_2$ series alloys (R=Y, Er, Ho, Dy and Gd) formed $RMn_2H_6$ structures at 1 GPa and 373 K through total reconstruction of the parent (C14 and C15) lattice [5,3,38]. Both $Y_6Mn_{23}$ and $YMn_{12}$ formed also $YMn_2H_6$-type structures with random substitution of Y and Mn atoms in 8c site (Fig. 6.30), where the occupancy fraction of Mn atoms increases as the Mn content in the parent compounds increases. Therefore, the lattice parameters of hydrides of $Y_6Mn_{23}$ and $YMn_{12}$ are similar to that of $YMn_2$ as shown in Table 6.5.

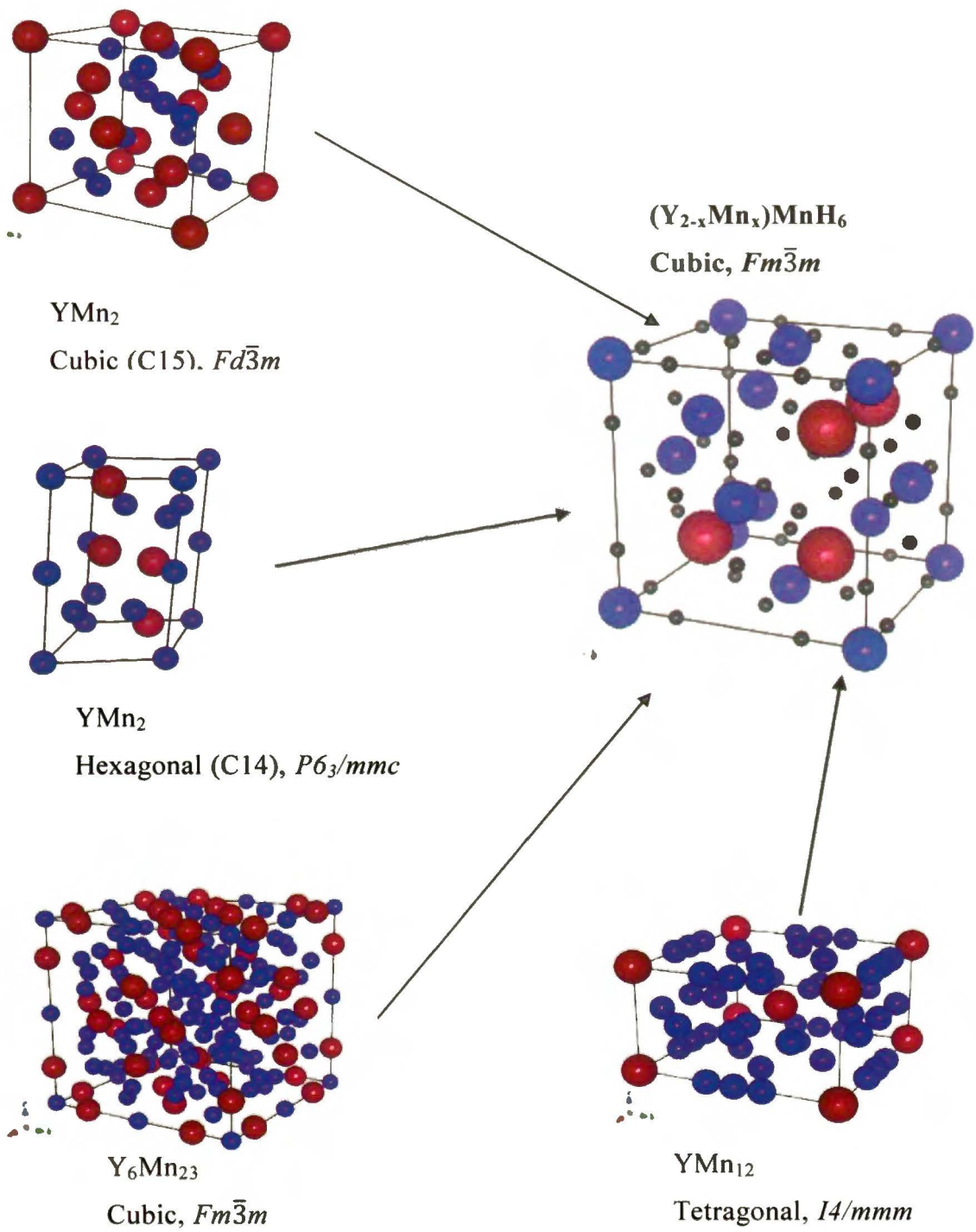


**Fig. 6.30. Schematic representations of Y-Mn series compounds and their hydride; four different compounds form $YMn_2H_6$-type structure at 1 GPa and 373 K.**

**Table 6.5. Crystallographic parameters of Y-Mn series compounds and their hydrides.**

| Sample | Structure type | Lattice parameters | |
|---|---|---|---|
| | | *a* (nm) | *c* (nm) |
| $YMn_2$ | *Fd*$\bar{3}$*m* (Cubic) | 0.768 | - |
| $YMn_2H_6$ | *Fm*$\bar{3}$*m* (Cubic) | 0.669 | - |
| $Y_6Mn_{23}$ | *Fm*$\bar{3}$*m* (Cubic) | 1.243 | - |
| $(Y_{18/29}Mn_{40/29})MnH_6$ | *Fm*$\bar{3}$*m* (Cubic) | 0.669 | - |
| $YMn_{12}$ | *I4/mmm* (Tetragonal) | 0.860 | 0.479 |
| $(Y_{3/13}Mn_{23/13})MnH_6$ | *Fm*$\bar{3}$*m* (Cubic) | 0.669 | - |

Under high hydrogen pressure we succeeded for the first time to synthesize novel hydride from $Y_6Mn_{23}$ with hydrogen concentration two times higher than in $Y_6Mn_{23}H_{25}$ hydride known so far. In the case of $YMn_{12}$ we got the hydride phase for the first time. It is especially interesting that hydrides received under high hydrogen pressure from $YMn_2$, $Y_6Mn_{23}$ and $YMn_{12}$ in principle are isostructural and have cubic structure with *Fm*$\bar{3}$*m* space group in which 4a sites are occupied only by manganese (Mn1) while 8c sites are filled randomly by yttrium and manganese (Mn2) [71] in ratio depending on the parent composition, thus manganese to yttrium ratio is 1:1, 9:20 and 3:23 for $YMn_2$, $Y_6Mn_{23}$ and $YMn_{12}$, respectively. This result together with former received for $(Y_xDy_{1-x})Mn_2$ pseudobinary alloys confirms that 8c positions in Fm$\bar{3}$m lattice of $RMn_2H_6$ hydrides can randomly accommodate yttrium, rare earth or manganese in various ratios.

## 6.2.4. $R_7Rh_3 - H_2$ ($D_2$)*Systems*

### *6.2.4.1. Crystal Structures of $R_7Rh_3$ Deuterides*

$R_7Rh_3$ (R = Ho, Y, Dy, Tb and Er) intermetallics have been deuterized between 0.2 MPa and 1 GPa at several temperature conditions. As shown in Fig. 6.31, $Ho_7Rh_3$ absorbed large amount of deuterium and formed deuteride without changes of crystal symmetry even at pressure as low as 0.6 MPa. The peak positions remained almost unchanged up to 0.5 GPa if deuterium gas was introduced very slowly at the initial absorption stage. The rapid introduction of deuterium at 0.3 GPa, 0.5 GPa or 1 GPa ($D_2$) to the $Ho_7Rh_3$ samples resulted in its decomposition as can be seen in the XRD patterns (Fig. 6.31). For example, the sample exposed to deuterium at 0.5 GPa and 373 K was decomposed whereas the same pressure condition led to the $Ho_7Rh_3D_x$ deuteride at 298 K. Thus, rapid deuterium charge and high deuterium absorption rate caused was cause of the decomposition. E.B. Boltich and coworkers reported that the number of peaks of $Th_7Fe_3$, $Th_7Co_3$ and $Th_7Ni_3$ ($Th_7Rh_3$ type structure) decreased after their hydrogenations and it was impossible to attribute the hydride patterns to hexagonal structure [46], but they rather indicated decompositions of the samples. In the pattern received after deuterium treatment of $Ho_7Rh_3$ at 0.5 GPa and 373 K (Fig. 6.31) also, the number of peaks decreased and $HoH_3$ at $2\theta = 27°$ and 28.5°, and one peak of $HoH_2$ at 33.5° can be seen. At $2\theta = 37°$, there is a large peak which can be indexed as $HoH_{1.8}$ according to Shashikala [72]. From our result and these references, it is clear that $Ho_7Rh_3$ sometimes lost hexagonal structure by high-pressure deuterium treatment and decomposed into $HoD_{1.8\sim2}$ and $HoD_{2.7\sim3}$, what can be seen at XRD diffraction pattern. However if reaction was conducted carefully the deuteride was obtained without change of the crystal symmetry.

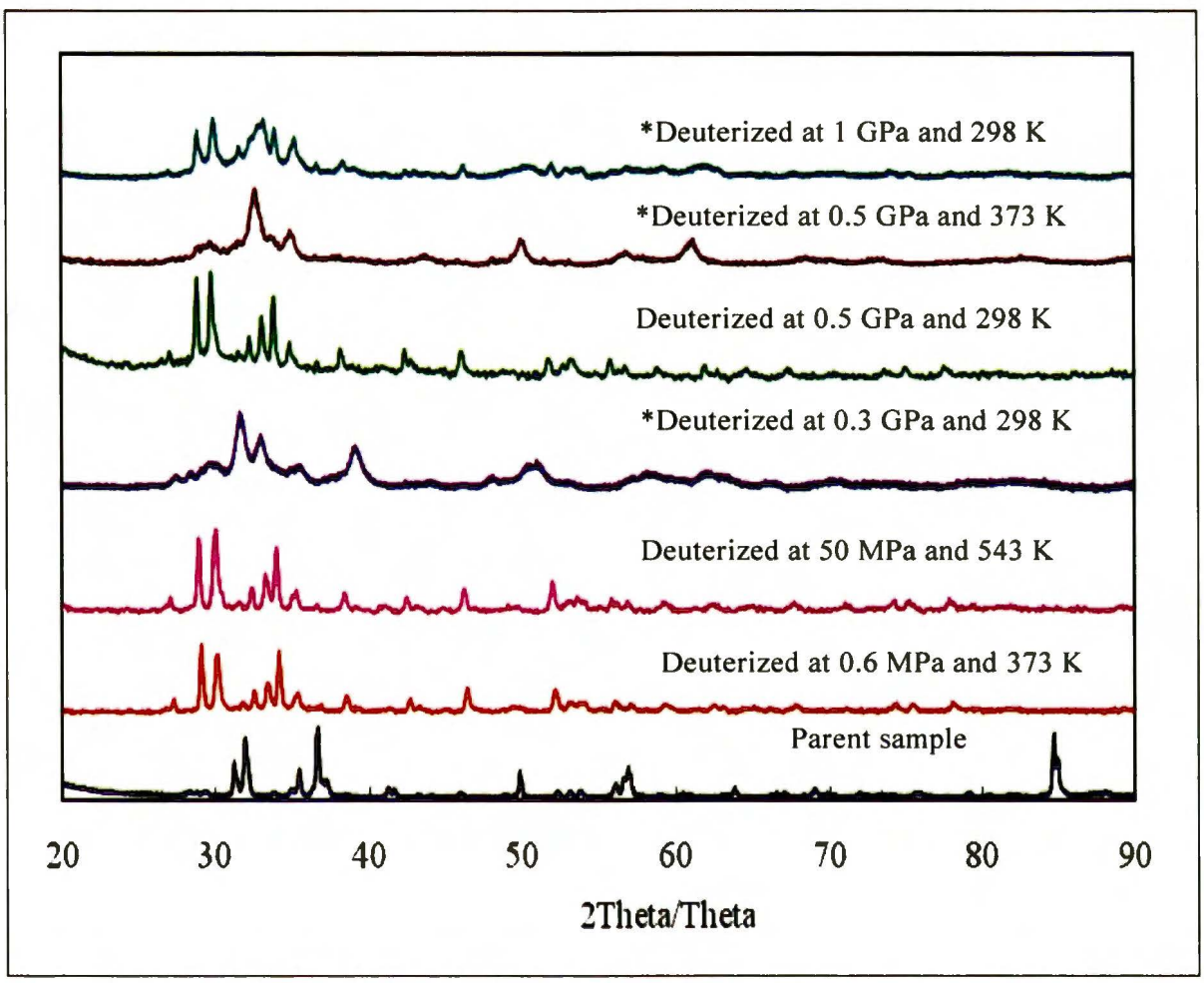


**Fig. 6.31. XRD diffraction patterns of $Ho_7Rh_3$ and the deuterides at several pressures and temperatures. (*rapid charging with deuterium)**

As shown in Fig. 6.32, $Dy_7Rh_3$, $Y_7Rh_3$ and $Er_7Rh_3$ also absorbed deuterium and formed deuterides without decomposition between 0.6 MPa and 0.5 GPa by introducing deuterium slowly. However, as shown in Fig. 6.33, under 1 GPa and 298 K $Dy_7Rh_3$ decomposed into $DyD_2$ ($CaF_2$-type) and $DyD_3$ ($BiF_3$ or $HoH_3$-type) as can

be seen from their peak positions corresponding to those. K. Aoki and coworkers [73,74,75] who investigated thermal decomposition of $DyFe_2$ hydride at 673K found $DyD_2$ and $DyD_3$ in decomposition products. At 773 K, the peaks were sharpened and dark particles could be observed in bright field image of SEM. In the matter of fact, the deuterized $Dy_7Rh_3$ after decomposition had also such darkened particle. For $Er_7Rh_3$ treated at 0.9 GPa and 298 K the peaks from $ErH_3$ and $ErH_2$ can also be seen in Fig. 6.32 (c). These peak positions correspond to reports from T. Palasyuk, et. al. [76,77] and K. Aoki et. al. [78] From these results, it seems that the mechanism of decompositions of $R_7Rh_3$ by high pressure deuterium may also be related to strongly exothermic reaction responsible for uncontrolled increase of temperature. This reaction is irreversible due to the high stability of deuteride (or hydride) of a rare earth. The hydrogen equilibrium pressure at plateau region of $Er_7Rh_3$–$H_2$ system lies below 0.1 MPa at 263 K and the alloy absorbs hydrogen up to $Er_7Rh_3H_{17\sim18}$ at these temperature and the pressure conditions (Fig. 6.34).

The stability of $R_7Rh_3$ deuteride (hydride) can also be seen in exposing to vacuum at high temperature condition. Fig. 6.35 shows XRD patterns of $Y_7Rh_3$ parent sample (a); deuterized at 0.2 MPa and 373 K (b); and evacuated sample (b) for 5 hours at 553 K (c). Even though the peaks positions of sample (c) shifted slightly towards high angle side after the evacuation, their positions are close to those of sample (b). It means that deuterium (hydrogen) atoms remain in $R_7Rh_3$ deuteride (hydride) even after exposure to vacuum and high temperature condition.

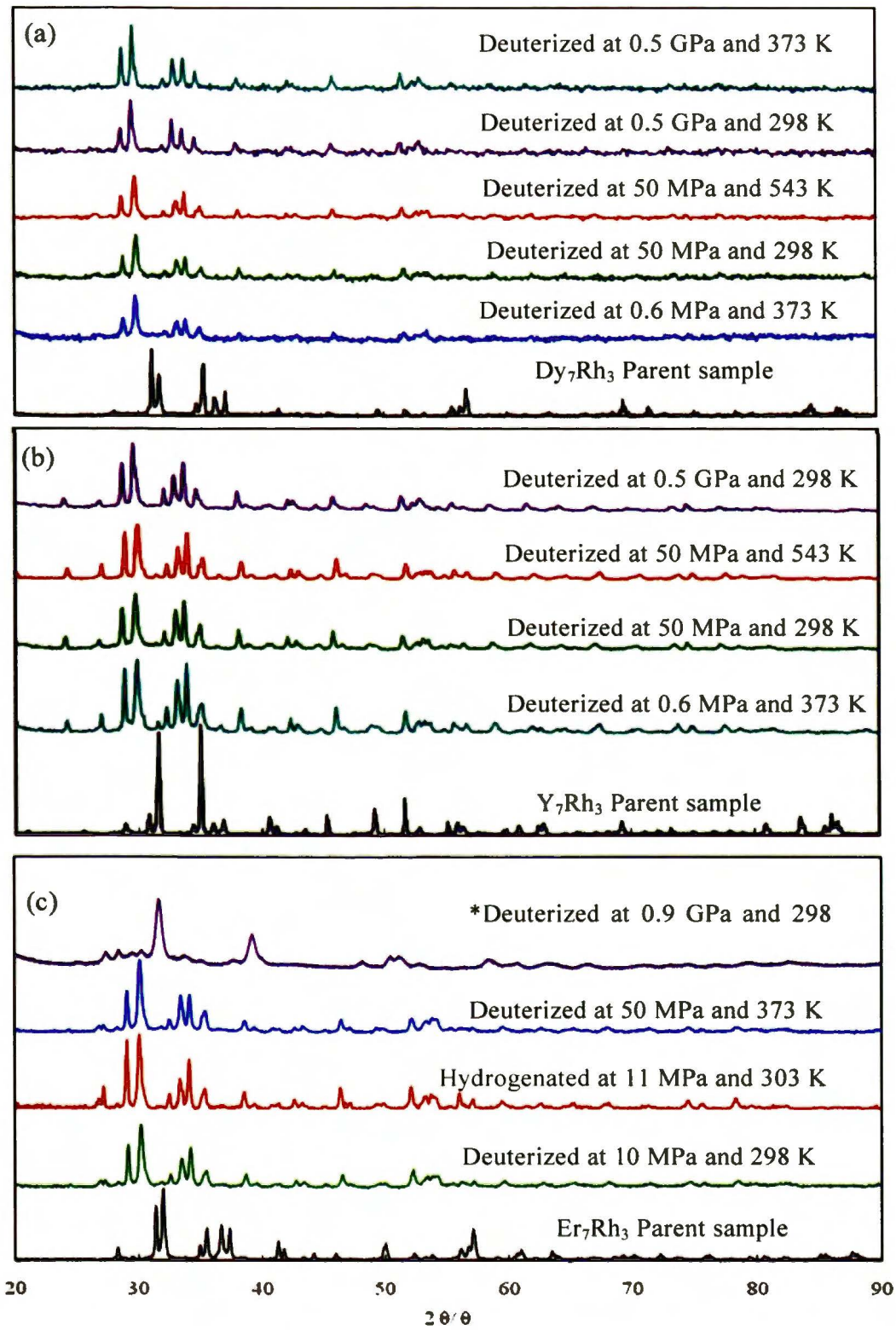


**Fig. 6.32. XRD patterns of several $R_7Rh_3$ compounds and their deuterides: (a) $Dy_7Rh_3$ deuterized up to 0.5 GPa; (b) $Y_7Rh_3$ deuterized up to 0.5 GPa and (c) $Er_7Rh_3$ deuterized up to 0.9 GPa. (*rapid charging with deuterium)**

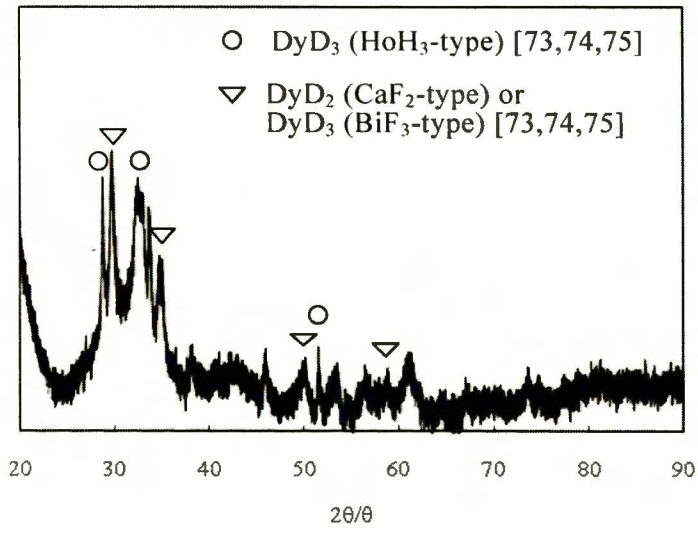


**Fig. 6.33. XRD pattern of $Dy_7Rh_3$ after treatment by deuterium at 1 GPa and 298 K. (rapid charging with deuterium)**

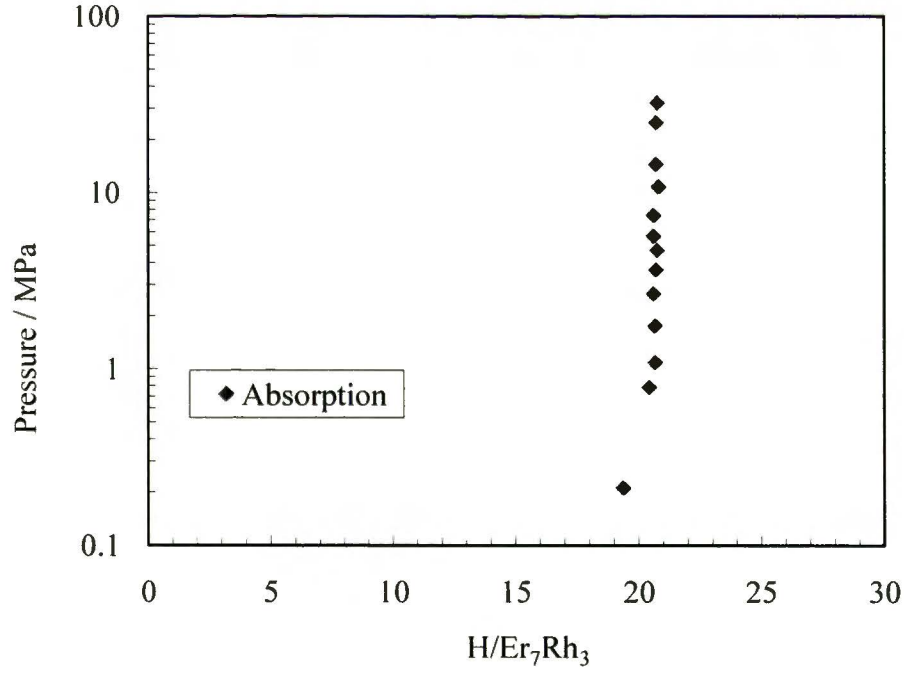


**Fig. 6.34. *p-C* isotherm of $Er_7Rh_3$-$H_2$ system at 263 K.**

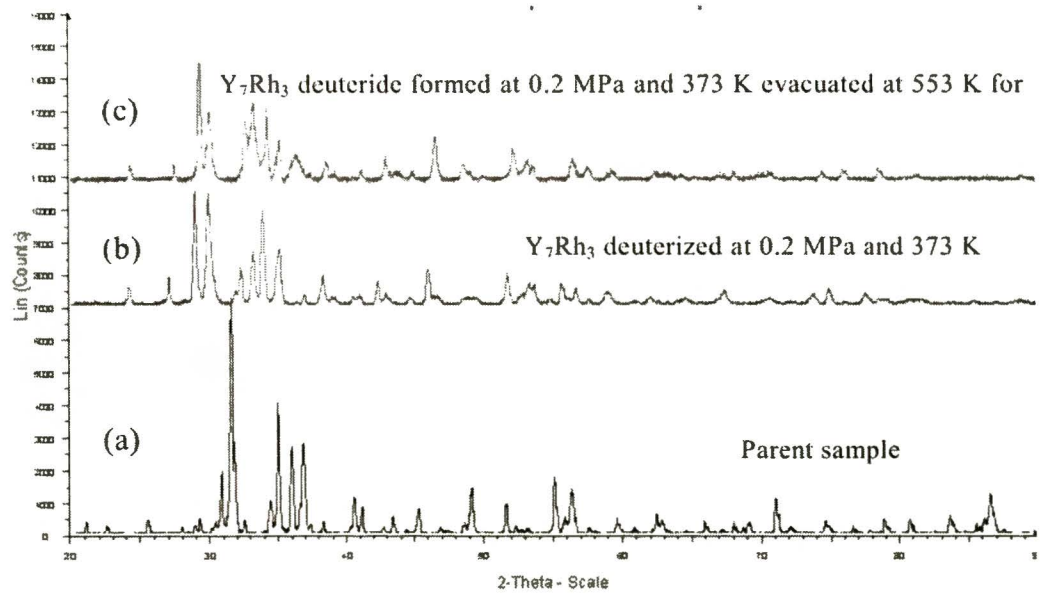


**Fig. 6.35. XRD patterns of parent $Y_7Rh_3$ and the deuterides: (a) parent sample; (b) deuteride synthesized at 0.2 MPa and 373 K and (c) deuteride (b) evacuated at 553 K for 5 hours.**

**Table 6.6. Crystallographic data of $R_7Rh_3$ and their deuterides.**

| Sample | Lattice parameters [nm] | | Unit cell volume [$nm^3$] | Volume expansion [%] |
|---|---|---|---|---|
| | *a* | *c* | | |
| $Y_7Rh_3$ | 0.976 | 0.618 | 0.509 | - |
| $Y_7Rh_3D_x$ | 1.029 | 0.662 | 0.607 | 19.3 |
| $Dy_7Rh_3$ | 0.975 | 0.611 | 0.503 | - |
| $Dy_7Rh_3D_x$ | 1.026 | 0.664 | 0.605 | 20.37 |
| $Ho_7Rh_3$ | 0.969 | 0.610 | 0.496 | - |
| $Ho_7Rh_3D_x$ | 1.025 | 0.661 | 0.601 | 21.02 |
| $Er_7Rh_3$ | 0.965 | 0.607 | 0.490 | - |
| $Er_7Rh_3D_x$ | 1.014 | 0.655 | 0.583 | 19.0 |

Deuterizations of $R_7Rh_3$ intermetallics at several pressure and temperature conditions, resulted in synthesis of deuterides with simple expansions of the lattice providing the deuterization proceeded gradually (slowly), especially at initial deuterium absorption. As shown in Table 6.6 all deuterides maintained hexagonal structure with space group *P6₃mc* with the volume expansions around 20 %.

When a $R_7Rh_3$ hydride/deuteride decomposed, we could identify only rare earth hydrides ($RD_2$ and/or $RD_3$) in the resulting diffraction pattern. The Rh peak did not appear on the XRD patterns. This behavior has also been reported for decomposition in $Gd_3T$ (T = Ni or Co) – $H_2$ system, where $GdH_x$ peaks appeared without T peaks although both elements were found in elemental analysis by EDX (Energy Dispersive X-ray) [79]. Explaining this fact, N.V. Tristan et. al. pointed out that T metals transformed to a dispersed phase not detectable by the X-ray analysis [80]. Consequently, we concluded that Rh was transformed to dispersed phase like Ni or Co in references [79,80] since Rh could also be observed in selected arbitrarily two areas from SEM (Scanning Electron Microscope) image (Fig. 6.36) in a measurement of EDX for $Dy_7Rh_3$ deuteride (Table 6.7).

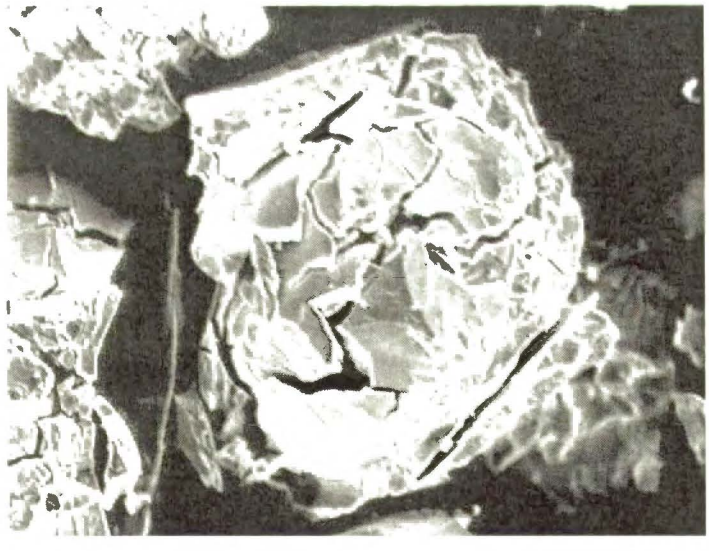

**Fig. 6.36. SEM image of $Dy_7Rh_3$ deuteride.**

**Table 6.7. Elemental analysis using EDX for $Dy_7Rh_3$ deuteride**

| Elements | Area 1 | Area 2 | Conditions | |
|---|---|---|---|---|
| | Atomic % | Atomic % | | |
| O (K) | 36.09 | 23.98 | Lifetime: | 180 sec |
| Rh (L) | 18.66 | 21.74 | Accelerating voltage: | 15.0 kV |
| Dy (L) | 45.25 | 54.28 | | |

After deuterization (hydrogenation) of $R_7Rh_3$, the deuterides tend to oxidize rapidly in ambient atmosphere due to the high reactivity of rare earths with $O_2$ [81]. Fig. 6.37 shows observation by laser microscope of surface of $Tb_7Rh_3$ hydride which was exposed to air for 2 days. In this figure, it is clear that the hydride was partially oxidized. Since oxidation of metals or alloys may be obstacle to hydrogen penetration, we must prevent them from contact with the air. The same should be kept in mind when hydrides are prepared for further investigations (structural, magnetic etc.).

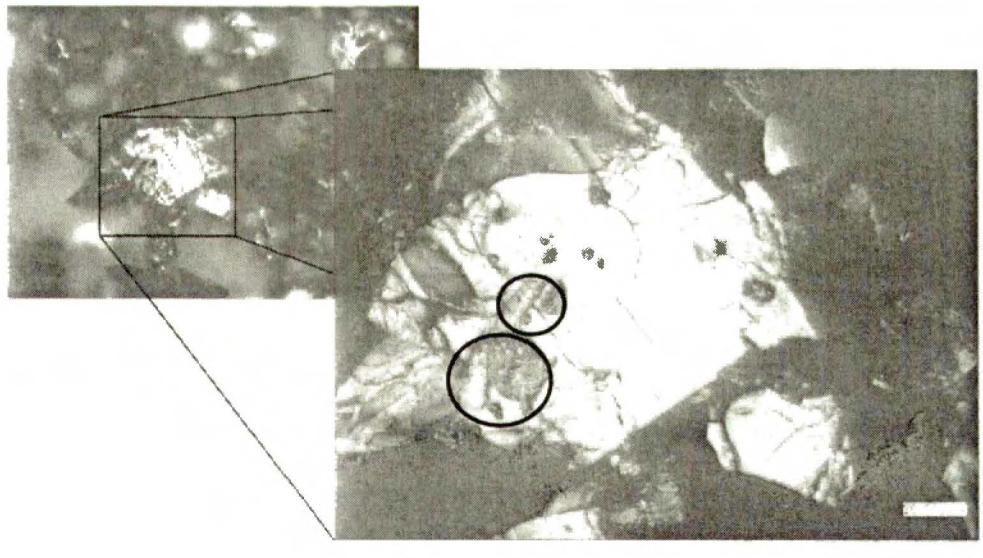

**Fig. 6.37. Surface observation of $Tb_7Rh_3$ exposed to air for 2 days after its hydrogenation, by laser microscope. Oxidized areas are surrounded with solid line.**

### *6.2.4.2. Magnetic Properties of $Dy_7Rh_3$ and $Tb_7Rh_3$ Hydrides*

Comparison of magnetic susceptibilities of $Tb_7Rh_3$ and $Tb_7Rh_3$ based hydrides measured at 11 kOe is given in Fig. 6.38. At low temperature region the magnetic susceptibilities of hydrides are markedly higher than for the parent sample like for $Th_7Ni_3$ hydride [49,50]. The hydrogen-free $Tb_7Rh_3$ has shown reentrant magnetic properties with antiferromagnetic, ferrimagnetic and another antiferromagnetic phase [51,82]. On the other hand, the $Tb_7Rh_3$ based hydrides exhibit only ferromagnetic or ferrimagnetic ordering at low temperatures confirmed for $Tb_7Rh_3H_{27}$ where residual magnetizations with large hysteresis was observed at 4.2 K (Fig. 6.39). The ferromagnetic or ferrimagnetic ordering can be seen at 80 K while the $Tb_7Rh_3$ sample has the Curie temperature at 73 K [82]. The hydrides do not have metamagnetic transitions in contrast to the parent sample in which such transition takes place at 35 K [82]. The residual magnetization of hydrides is relatively high and large hysteresis of magnetization curves is observed even at 75 K.

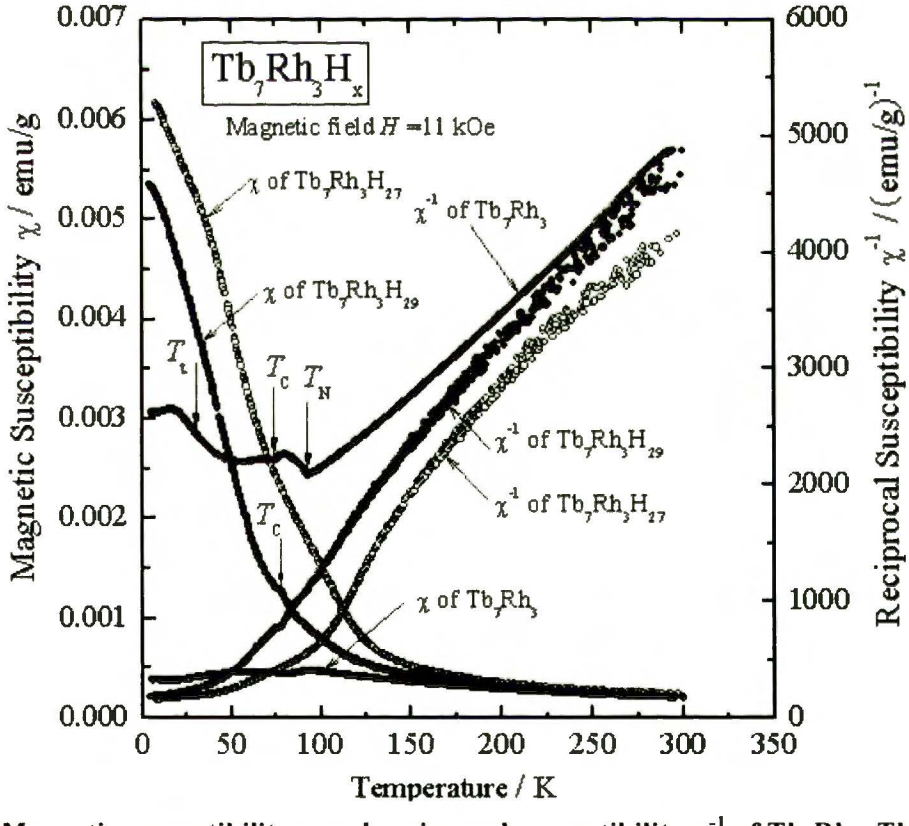


**Fig. 6.38. Magnetic susceptibility $\chi$ and reciprocal susceptibility $\chi^{-1}$ of $Tb_7Rh_3$, $Tb_7Rh_3H_{29}$ and $Tb_7Rh_3H_{27}$ as a function of temperature. $T_C$ indicates the Curie temperature.**

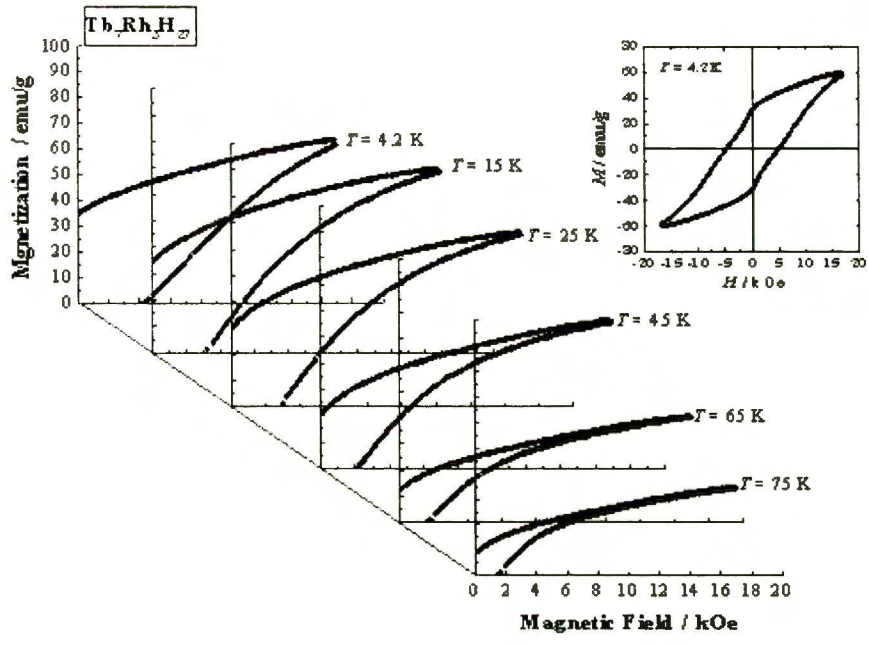


**Fig. 6.39. Magnetization curves of $Tb_7Rh_3H_{27}$ at various temperatures.**

Fig. 6.40 shows magnetic susceptibilities of $Dy_7Rh_3$ and $Dy_7Rh_3$ based hydrides at magnetic field of 10 kOe. For the parent sample, Curie and Néel temperatures were found at 34 K and 56 K, respectively [51]. No such transitions were found for $Dy_7Rh_3$ hydrides due to the lack of discontinuities on theirs susceptibilities curves. The reciprocal magnetic susceptibilities of $Dy_7Rh_3$ hydride show rather paramagnetic character at least between 30 and 300 K. The change of magnetic properties upon hydrogenation can be related to both: increasing the distance between localized magnetic states and to changes in electronic structure due to hydrogen absorption (hydrogen atoms take positions in the interstitial lattice sites as protons while their electrons fill up the empty states moving Fermi level towards higher energy values). The electronic structure change induced by hydrogen can also be found by XAS (X-ray Absorption Spectroscopy) measurement, for instance, influence of the H atoms in $R_2Fe_{14}B$ alloys has been observed as a change of K- or L-edge intensities [83]. From Fig. 6.41, which shows magnetization curves of $Dy_7Rh_3$ at low temperature range, it is clear that residual magnetization appears near 30 K and increases with decreasing temperature. This suggests a possible magnetic transition into ferromagnetic or ferrimagnetic state which would exist below 30 K [82].

The resulted magnetic properties of these hydrides were different from those of parent materials; magnetic anomalies were much weaker than in hydrogen-free alloys. This can be related to the change of interatomic distance and/or changes in the electronic structure of the alloy. For each hydride only one magnetic transition was observed leading to ferro- or ferrimagnetic ordering at 80 K (for $Tb_7Rh_3$ based hydride) or 30 K (for $Dy_7Rh_3$ based hydride). Magnetization curves of both, $Tb_7Rh_3$ and $Dy_7Rh_3$ hydrides showed large residual magnetizations at low temperatures region. At 4.2K both hydrides have ferromagnetic or ferrimagnetic ordered state.

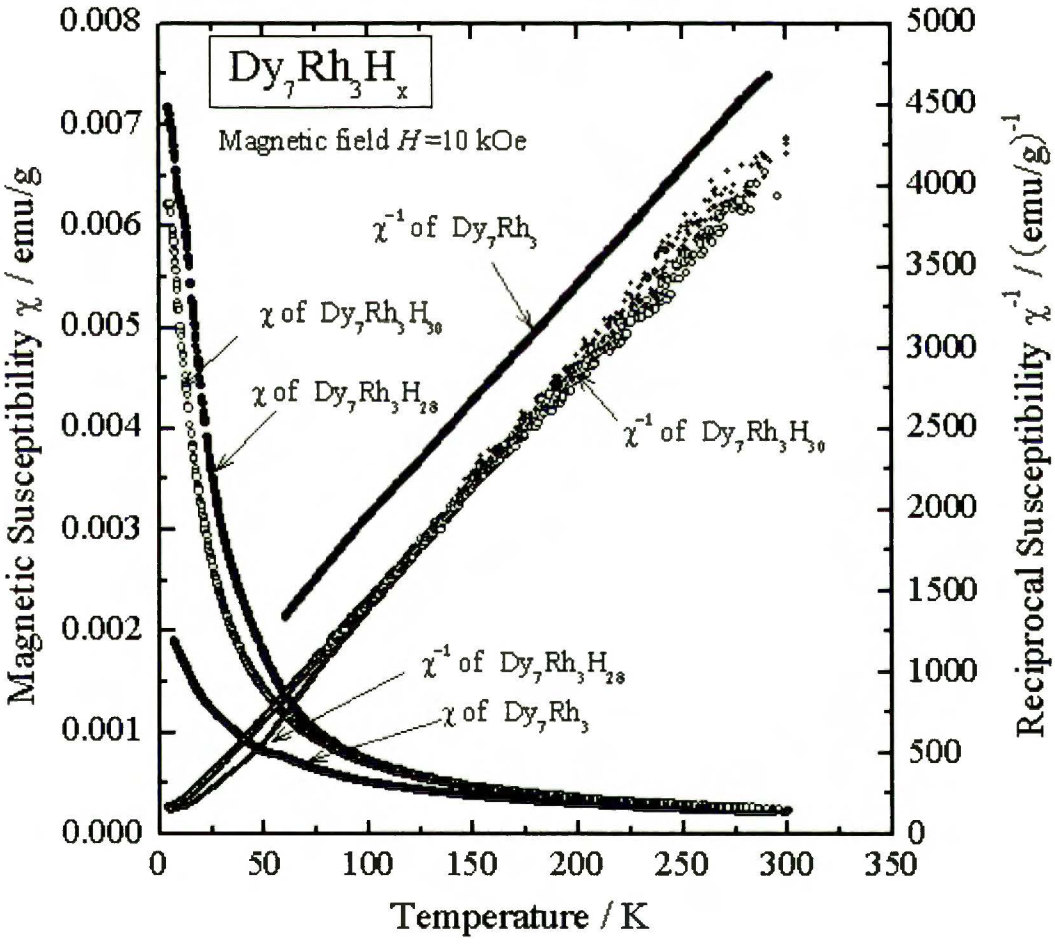


**Fig. 6.40. Magnetic susceptibility $\chi$ and reciprocal susceptibility $\chi^{-1}$ of $Dy_7Rh_3$, $Dy_7Rh_3H_{28}$ and $Dy_7Rh_3H_{30}$ as a function of temperature. $T_C$ indicates the Curie temperature.**

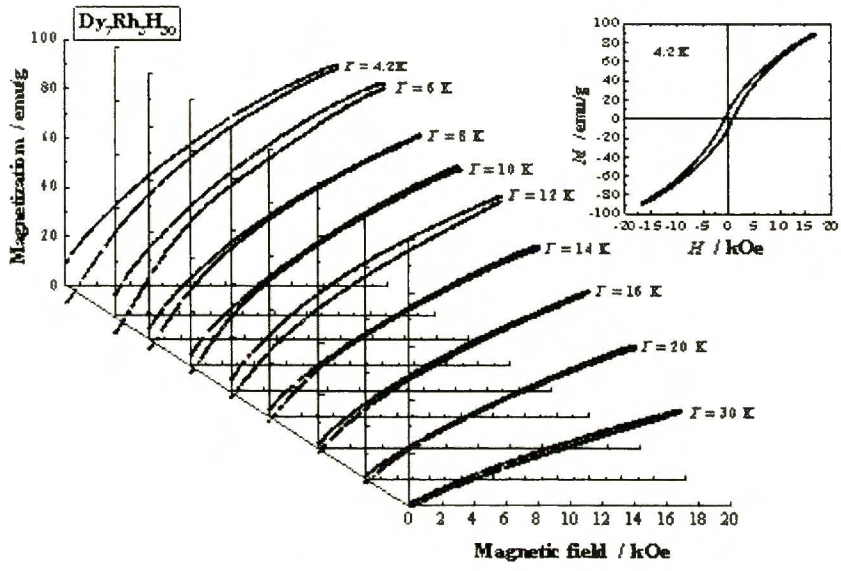


**Fig. 6.41. Magnetization curves of $Dy_7Rh_3H_{30}$ at various temperatures.**

# 7. Conclusions

Several novel hydrides were synthesized by using high pressure of hydrogen (deuterium) gas and their properties were determined. Results can be summarized as follows:

I. High-pressure Sieverts' apparatus (up to 70 MPa) has been constructed and used for measurement of isotherms of hydrogen absorption in Zr-based alloys. Both $Zr(Co_{1-x}Cr_x)_2$ and $Zr(Fe_{1-x}Cr_x)_2$ compounds absorbed hydrogen at 293 K. With increasing Cr content the hydrogen concentrations in both compounds increased, the hydrogen equilibrium pressure decreased. Comparing two systems, it became clear that for the same x value the plateau pressures of hydride formations for $Zr(Co_{1-x}Cr_x)_2$ are higher than those of $Zr(Fe_{1-x}Cr_x)_2$ alloys.

II. Parent samples of $Zr(Co_{1-x}Cr_x)_2$ have cubic or hexagonal structure (ZrCoCr and $ZrCo_{0.5}Cr_{1.5}$ are hexagonal). Hydrides of $ZrCo_2$ and $ZrCo_{1.8}Cr_{0.2}$ could be formed at 1 GPa and 373 K without change of their parent C15 symmetry. These hydrides are not stable at normal condition and decomposed within several hours. Formation of hydrides with higher Cr concentrations (e.g. $ZrCo_{1.5}Cr_{0.5}$) was accompanied with larger expansion of lattice parameters. However, even though hexagonal samples, their space group did not change during hydride formation. It was also revealed that the stability of hydrides increased with increasing concentration of Cr.

III. The lattice parameter of $Zr(Co_{1-x}Fe_x)_2$ increased with increasing Fe content but C15 cubic structure remained in whole composition range. The relative volume expansion of unit cells $\Delta V/V$ during hydride formation increased with increasing Fe substitution for Co. Kinetic measurements of decomposition of $Zr(Co_{1-x}Fe_x)_2$ based deuterides revealed that $ZrCo_{0.2}Fe_{1.8}D_x$ was much more stable than $ZrCo_{1.5}Fe_{0.5}D_x$. It has been proved that the substitution of Fe for Co increased deuterium content in deuterides and improved their stability.

IV. $(Ti_{1-x}Zr_x)Co_2$ ($0 < x < 1$) alloys and their hydrides were characterized by XRD, XAS and SQUID. According to XRD patterns both parent alloys and their hydrides have cubic structure. In spite of very high hydrogen pressure during the synthesis, we did not receive hydrides of $(Ti_{1-x}Zr_x)Co_2$ for x values lower than 0.50. In-situ XRD of discharging process was studied for $(Ti_{0.1}Zr_{0.9})Co_2$ hydride which is unstable at ambient conditions and rapidly decomposes to the parent phase. The stability of hydrides improves in following sequence: $TiCo_2 < ZrCo_2 < ZrFe_2 < ZrCr_2$.

V. SQUID measurement of magnetization reveals that magnetic moment in $Ti_{0.1}Zr_{0.9}Co_2$ decreases slightly after hydrogenation. This is attributed to the weakening of Co–Co magnetic coupling and filling up of the Co conduction band by electrons from hydrogen atoms.

VI. $RFe_2$ compounds (R = Gd, Tb, Ho and Er) with C15 cubic structure were deuterized at 1 GPa and 373 K. XRD measurements of received deuterides detected a mixture of orthorhombic and cubic structure for R = Dy and Ho whereas only cubic structure appeared for R = Gd and Tb. Since the amount of orthorhombic phase increases with increasing atomic number of rare earth, it suggests that the orthorhombic distortion tends to occur for smaller radius of the rare earth. As can be seen in structure of $ErFe_2H_5$ which transforms from orthorhombic into cubic [29], it is possible that orthorhombic and cubic structure have close enthalpy of formation.

VII. High pressure deuterium treatment of $Dy_xY_{1-x}Mn_2$ ($0.1 \leq x \leq 0.9$) was carried out at 1 GPa and 373 K for 14 days. XRD measurement of these deuterides revealed that their structures were identical as $YMn_2D_6$ with $Fm\bar{3}m$ cubic structure. It means that in the pseudobinary alloys the formation of $Fm\bar{3}m$ cubic $Dy_xY_{1-x}Mn_2D_6$ deuterides is possible for all Dy/Y atomic ratios. Therefore in $RMn_2D_6$ deuterides the positions 8*c* in their $Fm\bar{3}m$ lattice can be occupied by manganese and two different rare earth (or yttrium) atoms. On the other hand the

occupation of positions 4*a* is more restricted being "reserved" only for manganese.

VIII. Under high hydrogen pressure we succeeded for the first time to synthesize hydride of $YMn_{12}$ and a novel hydride of $Y_6Mn_{23}$ with hydrogen concentration two times higher than in $Y_6Mn_{23}H_{25}$ hydride reported by Pourarian [43]. It is especially interesting that hydrides received under high hydrogen pressure from $YMn_2$, $Y_6Mn_{23}$ and $YMn_{12}$ in principle are isostructural and have cubic structure with Fm m space group. All three hydrides have one Mn atom in 4a position which forms a complex anion with 6 H atoms. Remaining manganese and yttrium atoms occupy randomly the 8c site with different manganese-to-yttrium occupancy ratio.

IX. $R_7Rh_3$ alloys with *P6₃mc* hexagonal structure could form their hydrides even at 0.2 MPa with high stabilities in normal conditions. Formation of hydrides was followed by ~20 % expansion of the lattice. However, quick introducing of hydrogen to $R_7T_3$ alloys led to the decompositions of the samples.

X. The hydride of $Tb_7Rh_3$ exhibited higher susceptibility than the parent sample. The susceptibility curve of parent sample indicated reentrant magnetic structures which disappeared after the formation of hydride. Magnetic susceptibility of $Tb_7Rh_3H_x$ exhibited ferromagnetic or ferrimagnetic property below 80.2 K. The reciprocal susceptibilities of $Dy_7Rh_3$ hydride showed paramagnetic character at least between 30 K and 300 K. Below 30 K $Dy_7Rh_3$ hydride transforms into ferro- or ferrimagnetic state.

# 8. References


[1] K. Ohnishi, Technologies of Hydrogen Absorbing Alloys, CMC Shuppan, Tokyo, 2002.

[2] V. Paul-Boncour, et. al., J. Alloys and Compd., 317-318 (2001) 83.

[3] V. Paul-Boncour, et. al., J. Phys. Condens. Matter, 21 (2009) 016001.

[4] V. Paul-Boncour et al., J. Phys; Condens. Matter 18 (2006) 6409–6420.

[5] S.M. Filipek et al., J. Phys; Conf. Ser., 121 (2008) 022001.

[6] S.A. Nikitin, I.S. Tereshina, N.Yu. Pankratov, and Yu.V. Skoursk, Phys. Rev. B, Vol. 63, 134420, 2001.

[7] S. Kumari, J. Mater Sci. 41(2006) 5510-5513.

[8] H. Uchida, Int. J. Hydrogen Energy, 24 (1999) 861-869.

[9] M. Sato, Faculty of Mathematics and Natural Sciences, University of Oslo, Doctor thesis 2005.

[10] H. Uchida and M. Ozawa, Z. Physikalische Chimie N. F., Bd. 147, S.77-88, 1986.

[11] Saul Dushman, *Scientific Foundations of Vacuum Technique*, 2nd ed. New York, : John Wiley & Sons, 1965.

[12] Peter Atkins and Julio de Paula, *Atkins' Physical Chemistry*, 7th ed. New York: Oxford University Press, 2002.

[13] G.Ertl, Z. Physikalishe Chemie N. F., Bd.164, S.1115-1120 (1989).

[14] J.K. Nørskov and F. Besenbacher, J. Less-Common Met., 130 (1987) 475-490.

[15] Y. Fukai, *The Metal – Hydrogen System.*: Springer-Verlag Berlin Heidelberg, 1993.

[16] C.A. Edwards, Trans, AIME, 117, 13 (1935).

[17] R. Kadono, Current Opinion in Solid State and Material Science Vol.6 (2002) 141-146.

[18] G.M.Luke, et. al., Phys. Rev. B, Vol.43, No.4, 3284 (1991).

[19] N. Gerard, J. Less-Common Met., 131 (1987) 13-23.

[20] H. Uchida and T. Kuji, Int. J. Hydrogen Energy, 24 (1999) 871-877.

[21] F. Pourarian, Physica B 321 (2002) 18-28.

[22] S.K. Malik, T. Takeshita, and W.E. Wallace, Solid State Commun. 23 (1977) 599.

[23] K. Hardman-Rhyne, J.J. Rhyne, E. Prince, C. Crowder, and W.J. James, Phys. Rev. B 29 (1984) 416.

[24] F. Ishikawa, I. Yamamoto, M. Yamaguchi, M. I. Bartashevich, and T. Goto, J. Alloys and Compd., 253-254 (1997) 350-352.

[25] D. Shaltiel, J. Less-Common Met., 73 (1980) 329-338.

[26] D. Shaltiel, I. Jacob and D.Davidov, J. Less-Common Met., 53 (1977) 117-131.

[27] S.M. Filipek et al., Polish J. Chem. 75 (2001) 1921-1926.

[28] V. Paul-Boncour, et. al., J. Alloys and Compd., 356-357 (2003) 69-72.

[29] V. Paul-Boncour, et. al., J. Phys; Condens. Matter, 15 (2003) 4349.

[30] V. Paul-Boncour and A. Percheron-Guegan, J. Alloys and Compd., 293-295 (1999) 237-242.

[31] V. Paul-Boncour et al., J. Solid State Chem., 142 120-129 (1999).

[32] H.A. Kierstead, J. Less-Common Met., 70, 199 (1980).

[33] K. Shashikala, P. Raj, and A. Sathyamoorthy, Mater. Res. Bull., 31 (1996) 957.

[34] Z. Tarnawski, et. al., J. Alloys and Compd., 446-447 (2007) 415-418.

[35] H. Figiel, et. al., J. Alloys and Compd., 274 (1998) 29-37.

[36] J. Przewoznik, V. Paul-Boncour, M. Latroche, and A. Percheron-Guégan, J. Alloys and Compd., 225 (1995) 436-439.

[37] H. Figiel, A. Lindbaum, Cz. Kapusta, and E. Gratz, J. Alloys and Compd., 217 (1995) 157-160.

[38] V. Paul-Boncour, et. al., J. Solid State Chem., 178 (2005) 356-362.

[39] B. Huang, F. Bonhomme, P. Selvam, K. Yvon, and P. Fischer, J. Less-Common Met., 171 (1991) 301-311.

[40] J.V. Florio, R.E. Rundle and A.I. Snow, Acta Cryst., (1952). 5, 449.

[41] D. Berthebaud, et. al., J. Solid State Chem., 180 (2007) 2926-2932.

[42] X. Chen, W. Jeitschko and M. H. Gerdes, J. Alloys and Compd., 234 (1996) 12-18.

[43] F. Pourarian, E.B. Boltich, W.E. Wallace, R.S. Craig, and S.K. Malik, J. Magn. Magn. Mater., 21 (1980) 128-132.

[44] S. Obbade et al., J. Alloys and Compd., 253-254 (1997) 198-301.

[45] G.L. Olcese, J. Less-Com. Met., 33 (1973) 71-81.

[46] O. Trovarelli and J.G.Sereni, J. Low Temp. Phys., Vol.108. Nos. ½, 1997.

[47] P. Fischer, W. Haelg, L. Schlapbach, and K. Yvon, J. Less-Com. Met., 60 (1978) 1-9.

[48] G. Busch, L. Schlapbach and T.H. Von Waldkirch, J. Less-Com. Met., 60 (1978) 83-89.

[49] E. B. Boltich, S. K. Malik and W. E. Wallace, J. Less-Common. Met., 74 (1980) 111-116.

[50] S. K. Malik, E. B. Boltich and W. E. Wallace, Solid State Commun, Vol.33 (1980) pp.921-923.

[51] T. Tsutaoka, T. Tokunaga, M. Kosaka, Y. Uwatoko, and H. Suzuki, Physica B, 294-295 (2001) 199-202.

[52] T. Tsutaoka et al., Physica B, 327 (2003) 352-356.

[53] Y. Nakamori, T. Tsutaoka, T. Tokunaga, Y. Itoh, and H. Fujii, Physica B, 304 (2001) 1-5.

[54] T. Tsutaoka, Y. Nakamori, T. Tokunaga, H. Kadomatsu, and Y. Itoh, J. Alloys and Compd. 270 (1998) 53.

[55] Y. Nakamori et al., Physica B 329-333 (2003) 1087-1089.

[56] J.R. Christman, *Fundamentals of Solid State Physics*. New York: John Wiley & Sons, 1988.

[57] E.Talik, et. al., J. Cryst. Growth, 283 (2005) 547-552.

[58] T. Tsutaoka, Y. Nakamori, K. Koyama, and T. Tokunaga, J. Magn. Magn. Mater., 293 (2005) 768 - 773.

[59] H. Uchida, K. Terao, and Y.C. Huang, Z. Phys. Chem., Bd. 164, S. 1275-1284

(1989).

[60] H. Uchida, et. al., J. Less-Common. Met., 172-174 (1991) 983-996.

[61] H. Uchida and S. Hashimoto, Z. Phys. Chem., Bd. 181, S. 417-422 (1993).

[62] R. Sato, Department of Applied Sciences, Faculty of Engineering, Tokai University, Kanagawa, Master Thesis 2004.

[63] Y. Suzuki, T. Haraki and H. Uchida, J. Alloys and Compd., 330-332 (2002) 488-491.

[64] I.I. Bulyk, Yu.B. Basaraba and A.M. Trostianchyn, J. Alloys and Compd., 367 (2004) 283-288.

[65] B. Jiang and David J. Smith J. Sun, Phys. Rev. B 69, 214107 (2004).

[66] H.T. Kuo et al., Inorg. Chem., 2009, 48, 11655-11659.

[67] V. Paul-Boncour and A. Percheron Guegan, J. Alloys and Compd., 293-295 (1999) 237.

[68] P. Raj, K. Shashikala, A. Sathyamoorthy, V. Siruguri, and S. K. Paranjpe, Phil. Mag. B, Vol. 79 (1999) 1185.

[69] S.M. Filipek, et. al., Journal of The Hydrogen Energy Systems Society of Japan, Vol.34, No.4 (2009) 31.

[70] R.S. Liu, et. al., J. Phys. Soc. Jpn., 76 (2007) Suppl. A, pp.5-6.

[71] S.M. Filipek, et. al., J. Phys; Conf. Ser., Accepted publication.

[72] K. Shashikala, S. Banerjee, R. Kulkarni, and S.K. Dhar, J. Alloys and Compd., 467 (2009) 10-13.

[73] H.-W. Li, K. Ishikawa and K. Aoki, J. Alloys and Compd., 399 (2005) 69-77.

[74] K. Aoki, H.-W. Li and K. Ishikawa, J. Alloys and Compd., 404-406 (2005) 559-564.

[75] H.-W. Li, K. Ishikawa and K. Aoki, J. Alloys and Compd., 388 (2005) 49-58.

[76] T. Palasyuk, M. Tkacz and P. Vajda, Solid State Commun., 135 (2005) 226-231.

[77] T. Palasyuk and M. Tkacz, Solid State Commun., 130 (2004) 219-221.

[78] K. Aoki, M. Dilixiati and K. Ishikawa, Mater. Sci. Eng., 375-377 (2004) 922-926.

[79] T. Palewski, N.V. Tristan, H. Drulis, and J. Ćwik, J. Alloys and Compd., 404-406 (2005) 584-587.

[80] N.V. Tristan, T. Palewski, H. Drulius, L. Folcik, and S.A. Niktin, Materials Science, Vol. 21, No.3, 2003.

[81] M. Hadano, N. Urushihara, T. Inoue and H. Uchida, J. Alloys and Compd., 293-295 (1999) 403-406.

[82] R. Sato., T. Tsutaoka, and S.M. Filipek, J. Alloys and Compd., 446-447 (2007) 610-613.

[83] J. Chaboy and C. Piquel, Phys. Rev. B 66, 104433 (2002).

# 9. Academic Achievements

## *9.1. Publications*

- R. Sato, T. Tsutaoka and S.M. Filipek, High pressure synthesis and magnetic properties of $Dy_7Rh_3$ and $Tb_7Rh_3$ hydrides, J. Alloys and Compd. 446-447 (2007) 610-613

- H.-T. Kuo, R.-S. Liu, S. M. Filipek, R. Wierzbicki, R. Sato, C. L. Chan, H. D. Yang and J.-F. Lee, Formation of Hydrides in $(Ti_{1-x}Zr_x)Co_{2.00}$ $(0 < x < 1)$ Pseudobinary Alloys, Inorg. Chem., 48 (2009) 11655-11659

- S.M. Filipek, R. Sato, R. Wierzbicki and I. Marchuk, Selected Metal-Hydrogen Systems under High Hydrogen Pressure, Journal of Hydrogen Energy Systems Society of Japan, Vol.34, No.4 (2009) 31

- S.M. Filipek, V. Paul-Boncour, R. Sato, R. Wierzbicki and R.-S Liu, Unusual Behaviour of Manganese Containing Intermetallic Alloys under High Hydrogen Pressure, Review of High Pressure Science and Technology, 19 (2009) 366

- R.-S Liu, S.M. Filipek, H.-T Kuo, R. Wierzbicki, R. Sato, Hydrides of $(Ti_{1-x}Zr_x)Co_{2.00}$ $(0 < x < 1)$ Laves Phases Formed under High Hydrogen Pressure, Review of High Pressure Science and Technology, 19 (2009) 405

- S.M. Filipek, R. Sato, H. Tanaka, N. Kuriyama and N. Takeichi, Investigation of $Y_6Mn_{23}$ and $YMn_{12}$ Intermetallic Alloys under high Hydrogen Presures, Review of High Pressure Science and Technology, 19 (2009) 466

- S.M. Filipek, R. Sato, N. Kuriyama, H. Tanaka and N. Takeichi, Investigation of $Y_6Mn_{23}$ and $YMn_{12}$ Intermetallic Alloys under High Hydrogen Pressure, J. Phys.; Conf. Series, Accepted for publication

- S.M. Filipek, V. Paul-Boncour, N. Kuriyama, H. Tanaka, N. Takeichi, R.-S Liu, R. Wierzbicki, R. Sato and H.-T. Kuo, Hydrides of Laves Phases Intermetallic Compounds Synthesized under High Hydrogen Pressure, Solid State Ionics, 181 (2010) 306-310

## *9.2. International Conferences*

- *High Pressure Synthesis and Magnetic Properties of $Dy_7Rh_3$ and $Tb_7Rh_3$ Hydrides*, R. Sato, T. Tsutaoka and S.M. Filipek, MH 2006 – International Symposium on Metal-Hydrogen Systems (Maui, Hawaii, US) 1-6 October, 2006

- *Unusual Behaviour of Manganese Containing Intermetallic Alloys under High Hydrogen Pressure*, S.M. Filipek, V. Paul-Boncour, R. Sato, R. Wierzbicki and R.-S Liu, Joint AIRAPT-22 & HPCJ-50 – International Conference on High Pressure Science and Technology (Odaiba, Tokyo, Japan) 26-31 July, 2009

- *Hydrides of $(Ti_{1-x}Zr_x)Co_{2.00}$ ($0 < x < 1$) Laves Phases Formed under High Hydrogen Pressure*, R.-S Liu, S.M. Filipek, H.-T Kuo, R. Wierzbicki, R. Sato, Joint AIRAPT-22 & HPCJ-50 – International Conference on High Pressure Science and Technology (Odaiba, Tokyo, Japan) 26-31 July, 2009

- *Investigation of $Y_6Mn_{23}$ and $YMn_{12}$ Intermetallic Alloys under high Hydrogen Presures*, S.M. Filipek, R. Sato, H. Tanaka, N. Kuriyama and N. Takeichi, Joint AIRAPT-22 & HPCJ-50 – International Conference on High Pressure Science and Technology (Odaiba, Tokyo, Japan) 26-31 July, 2009

- *Hydrides of Intermetallic Compounds Synthesized under High Hydrogen Pressure*, S.M. Filipek, V. Paul-Boncour, R.-S Liu, R. Wierzbicki, R. Sato, Second Polish Forum Fuel Cells and Hydrogen Technologies (Kocierz, Poland) 7-10 September, 2009

## 10. Acknowledgements

I thank very much Prof. Stanisław M. Filipek for achievement of my doctor study in Institute of Physical Chemistry PAS.

I appreciate technical support on this study by Mr. Jacek Kowałek and Mr. Jan Kołodziejski.